

ABSTRACT

Ultra-Sensitive Instrumentation in the UV-Vis-NIR Spectral Region with Application on Overtone Spectroscopy

David Camejo, Ph.D.

Mentor: Carlos E. Manzanares, Ph.D.

Fourier transform infrared spectroscopy (FT-IR) is a technique widely used in molecular spectroscopy. Technology advancements are such that FT-IR spectrometers can measure vibrational transitions occurring well within the visible (Vis) region of the electromagnetic spectrum. High overtone transitions of C-H, N-H, and O-H can be measured in the near-infrared (NIR) and the Vis regions using long path cells. Despite the large sensitivity of the FT-IR spectrometers and the use of long path cells, the absorption intensities of these transitions are so low that commercial FT-IR spectrometers would not register the absorption bands. Phase shift cavity ring down (PS-CRD) and thermal lens spectroscopy (TLS) are ultra-sensitive instrumental absorption techniques very commonly used in our laboratory. These are very powerful techniques for the detection of weak absorptions in the NIR-Vis region. In the case of high overtone spectra, CRD is ideal for gas samples whereas TLS is great for liquid samples. In our laboratory we use FT-IR and UV-Vis spectrometers as complementary techniques to CRDS and TLS.

In order to simulate conditions in the atmospheres of other planets, we couple our instruments to a low temperature cryostat. In this way, these ultra-sensitive techniques can be applied to the study of gases in the atmosphere and liquid cryo-solutions to simulate the lakes of Saturn's largest moon, Titan. This work shows the use of signal-to-noise ratios to determine the spectral quality of spectra obtained with the PS-CRD technique, particularly in situations where human eye cannot perceive the small differences. We evaluate the impact of some instrumental parameters involved in data acquisition process of the PS-CRD technique, as well as evaluate the spectral quality as a function of the On-Axis/Off-Axis position of the incoming beam. This work also introduces the use of a second pumping laser for the analysis of multi-component samples in thermal lens. The design facilitates the detection of solvent and solute exciting two different vibrational overtones. Finally, the determination of band asymmetry using spectral moment calculations is shown for fundamental bands and vibrational overtones. The usefulness of this method as a complementary feature to TL spectroscopy is discussed.

Ultra-Sensitive Instrumentation in the UV-Vis-NIR
Spectral Region with Applications on Overtone Spectroscopy

by

David Camejo, Ph.D.

A Dissertation

Approved by the Department of Chemistry and Biochemistry

Patrick J. Farmer, Ph.D., Chairperson

Submitted to the Graduate Faculty of
Baylor University in Partial Fulfillment of the
Requirements for the Degree
of
Doctor of Philosophy

Approved by the Dissertation Committee

Carlos E. Manzanares, Ph.D., Chairperson

Darrin J. Bellert, Ph.D.

Kevin L. Shuford, Ph.D.

Touradj Solouki, Ph.D.

Lesley Wright, Ph.D.

Accepted by the Graduate School
August 2015

J. Larry Lyon, Ph.D., Dean

Copyright © 2015 by David Camejo

All rights reserved

TABLE OF CONTENTS

LIST OF FIGURES	IX
LIST OF TABLES	XIII
ACKNOWLEDGMENTS	XIV
DEDICATION	XVII
CHAPTER ONE	1
INTRODUCTION	1
<i>Molecular Vibrations</i>	2
<i>Detection Techniques</i>	7
<i>Dissertation Overview</i>	8
CHAPTER TWO	11
<i>CRD and Absorption Spectroscopy</i>	16
<i>Stability of an Optical Cavity</i>	18
<i>Cavity Modes</i>	19
<i>Off-Axis Alignment</i>	20
<i>CRDS Instrumentation and Procedures</i>	23
<i>CRD Cell Design</i>	23
<i>Instrumental Setup for PS-CRD Spectroscopy</i>	27
<i>PS-CRD Signal and Signal Conditioning</i>	28
<i>Experimental Procedure</i>	31
<i>Calibration</i>	31
<i>Off-Axis Alignment Procedure</i>	31

CHAPTER THREE	34
EVALUATION OF THE PS-CRD SPECTROMETER FOR THE ACQUISITION OF HIGH RESOLUTION SPECTRA	34
<i>Absorption Spectroscopy of the Oxygen Atmospheric Bands</i>	34
<i>Structure of the Bands</i>	36
<i>Absorption Spectra for the (2,0) γ-Band of O₂ using CRD Spectroscopy</i>	38
<i>Spectral Quality</i>	39
<i>Signal to Noise Ratio</i>	44
<i>Acquisition Pause</i>	46
<i>Pre-Amplification</i>	48
<i>Sensitivity</i>	51
<i>Off-Axis vs On-Axis Alignment</i>	54
<i>Conclusions</i>	55
CHAPTER FOUR	59
THERMAL LENS SPECTROSCOPY	59
<i>Theoretical Description of the TL</i>	63
<i>TL Cryostat and Vacuum Chamber</i>	65
<i>TL Cell Design</i>	68
<i>TL Experimental Setup</i>	70
<i>TL Signal and Signal Conditioning</i>	73
<i>TL Experimental Procedure</i>	76
<i>Calibration</i>	76
<i>Sample Condensation</i>	77

<i>Thermal Lens Spectroscopy and the Lakes of Titan</i>	77
<i>TL Spectrum of Benzene</i>	81
<i>TL Spectrum of Ethane</i>	82
<i>TL Spectrum of an Ethylene – Ethane cryo-solution</i>	83
CHAPTER FIVE	85
SPECTRAL MOMENT ANALYSIS.....	85
<i>First Moment</i>	87
<i>Second Moment</i>	89
<i>Calculation of First and Second Moment from TL Spectral Data</i>	91
<i>Conclusions</i>	94
CHAPTER SIX.....	97
GENERAL CONCLUSIONS AND RESEARCH OUTLOOK	97
<i>Phase Shift Cavity Ring Down Remarks</i>	97
<i>Thermal Lens Remarks</i>	98
APPENDIX A.....	101
ULTRAVIOLET-VISIBLE SPECTROSCOPY INSTRUMENTATION AND PROCEDURES	101
<i>UV-Vis Cryogenic Setup</i>	101
<i>UV – Vis Sample Cell</i>	103
<i>UV – Vis Cryostat Operation</i>	104
<i>UV-Vis Experimental Procedure</i>	105
<i>Background Acquisition</i>	106
<i>Sample Preparation</i>	106
<i>Sample Condensation</i>	108

<i>Spectra Acquisition</i>	109
<i>Shut-down Procedure</i>	109
APPENDIX B	111
CAVITY RING DOWN ALIGNMENT PROCEDURE	111
APPENDIX C	119
HIGH REFLECTANCE MIRRORS	119
<i>Mirror Cleaning Procedure</i>	120
APPENDIX D	122
CRYOSTAT OPERATION	122
APPENDIX E	125
LABVIEW CODES	125
<i>Cavity Ring Down DAQ Code</i>	125
<i>Thermal Lens DAQ Code</i>	130
REFERENCES	135

LIST OF FIGURES

Figure 1. Harmonic and Morse potential energy functions for a diatomic oscillator.	4
Figure 2. Vibrational overtone spectra of a solution of methane in argon at 87K acquired with a FT-IR spectrophotometer.	6
Figure 3. Pulsed Cavity Ring Down Diagram.....	11
Figure 4. Exponential decay of laser light within the ring-down cavity	12
Figure 5. Schematic representation of the experimental layout presented by O’Keefe and Deacon.	13
Figure 6. Phase shift cavity ring down diagram.....	14
Figure 7. PS-CRD signal (top), Reference signal (bottom).....	15
Figure 8. $\tan(\theta)$ versus θ graph.....	15
Figure 9. Stable optical cavities. (a) with mirror placed $r < L < 2r$, and (b) with mirror placed $0 < L < r$	19
Figure 10. Off-axis beam propagation	22
Figure 11. Predicted $\Delta\nu$ for a 43.5 cm cavity aligned (a) on axis and (b) off-axis when the reentrant condition is satisfied after 41 round trips.	23
Figure 12. Schematic side view (top) of the CRD cell design, (bottom) of the center cubic core.....	24
Figure 13. Expanded view of the left arm, showing the O-ring, HR mirror, as well as the mirror protector, and flange attachment (top); screws positions needed to hold and finely align the mirrors.....	26
Figure 14. Experimental setup of the PS-CRD spectrometer. Key: EOM, electro optical modulator; I, iris; L, plane-convex lens; PMT, photomultiplier tube.....	28
Figure 15. Calibration curve of the stepper motor	32
Figure 16. Mirror periscope located before the optical cavity	33

Figure 17. Potential energy diagram for the low-lying electronic states of O ₂	35
Figure 18. Combinations associated with branches of the red system of atmospheric oxygen.....	37
Figure 19. Bottom: Simulated rotational-vibrational spectrum of the γ band of O ₂ obtained with the PGOPHER program. Top: Corresponding Fortrait diagram. All rotational constants needed for this simulation were taken from reference 31.....	40
Figure 20. Bottom: Experimental result for the rotational-vibrational spectrum of the γ band of O ₂ acquired with PS-CRD. Top: Corresponding Fortrait diagram.....	41
Figure 21. Fortrait diagrams comparison the between the work of Babcock and Hertzberg (\blacktriangle), PGOPHER Simulation (\blacksquare), and this work (\bullet). Filled items represent the ^P P and ^R R branches while empty items represent the ^P Q and ^R Q branches.....	43
Figure 22. Oxygen γ band. Absorption pressure series at 295K.....	44
Figure 23. Oxygen γ band obtained at different acquisition pause. (Top) 300.0 ms, (Bottom) 0.0 ms.....	49
Figure 24. ^P Q5 and ^P P5 lines of the P-branch of the oxygen γ band evaluated at different pre-amplification gain. (Top) x100 times, (Middle) x50 times, (Bottom) x20 times.....	50
Figure 25. Section of the experimental setup of the PS-CRD spectrometer. Intensity of the reference beam versus intensity of the cavity beam. Key: I, iris; PMT, photomultiplier tube.....	53
Figure 26. ^P Q5 and ^P P5 lines of the P-branch of the oxygen γ band evaluated at different sensitivity values. (Top) 50 mV, (Bottom) 0.5 mV.....	53
Figure 27. Portion of the P-branch of the oxygen γ band, from ^P P13 to ^P P1, obtained at different Off-Axis positions. (Lowest) 0.0 mm, (Uppermost) 3.2 mm .	56
Figure 28. A probe beam irradiates an excited sample. Depending upon the change in the refractive index, η , and the density of the sample, a convergent or divergent lens will change the direction of the probe radiation	61
Figure 29. Optical system for thermal lens apparatus.....	62

Figure 30. Description of the cryostat and vacuum chamber use in the TL experiment	67
Figure 31. TLS 10 cm copper cell.....	69
Figure 32. Extended range thermal lens spectrometer.....	71
Figure 33. Lock-in amplifiers connection diagram.....	74
Figure 34. UV-vis spectra of benzene in liquid methane at 97 K.....	80
Figure 35. TL spectrum of the $\Delta\nu=6$ of benzene at room temperature, obtained with the extended range TL setup.....	82
Figure 36. TL spectrum of the $\Delta\nu=5$ of ethane at 91 K, obtained with the extended range TL setup.....	83
Figure 37. TL spectrum of the 10% $C_2H_4-C_2H_6$ solution at 100 K obtained with the extended range TL setup. Notice that the ethylene band is not showing in the expected frequency range.....	84
Figure 38. Graphical calculation of $M_{(1)}$ for the fifth overtone of benzene.	93
Figure 39. Graphical calculation of $M_{(2)}$ for the fifth overtone of benzene.	93
Figure 40. Graphical calculation of $M_{(1)}$ and $M_{(2)}$ for the fourth overtone of ethane ..	94
Figure A.1. Experimental set up for the study of cryogenic samples in the UV-Vis region.....	102
Figure A.2. Diagram of the cryostat head and vacuum chamber for the study of cryogenic samples in the UV-Vis region.....	102
Figure A.3. Diagram of the cell used in the UV-Vis experiment.....	104
Figure A.4. Experimental set-up for UV-Vis cryogenic sample preparation.....	107
Figure B.1. Front (or back) end of the cavity shown in frontal and angled profile....	112
Figure B.2. Periscope used for PS-CRD beam alignment.	113
Figure B.3. Attachment of HR mirrors onto the cavity ends	115
Figure B.4. Reflection of the laser beam onto the pinhole slide after it is reflected from the rear HR mirror	115

Figure B.5. Reflection of the laser beam onto the pinhole slide after it is reflected from the front HR mirror	116
Figure B.6. Ring-down signal for the exponential decay CRD method.....	117
Figure E.1. Measurement Panel Wiring Diagram.	126
Figure E.2. DAQ Movement of the motor.	127
Figure E.3. Delay time.	127
Figure E.4. Acquire Data Point and Calculated Absorption.	127
Figure E.5. Pscrd 830 Snap.vi.	128
Figure E.6. Stop Data Collection.	128
Figure E.7. Front panel of the Main PS-CRD vi code.	129
Figure E.8. Voltage acquisition.	131
Figure E.9. Stepper motor control.	131
Figure E.10. Saves the raw data.	132
Figure E.11. Addressing of the GPIB, and storage of data points.	132
Figure E.12. DAQ, and addressing of the information out from the lock-in amplifier through the GPIB.....	133
Figure E.13. Block diagram of the Graph.vi that shows the final results	133
Figure E.14. (Top) Front panel of the Main TLS vi code. (bottom) Graph result vi ..	134

LIST OF TABLES

Table 1. Mode Spacing Calculations	20
Table 2. Comparison between $\Delta v_{\text{off-axis}}$ and $\Delta v_{\text{on-axis}}$	22
Table 3. Center wavelength, bandwidth and radii of curvatures for CRD mirrors ..	26
Table 4. Line absorption frequencies	42
Table 5. S/N results with the ^R R11 line values	46
Table 6. S/N results with the ^P P5 line values	46
Table 7. S/N results at different pause length using the ^R R11 line values	47
Table 8. S/N results at different pause length using the ^P P5 line values	47
Table 9. S/N results at different gain values	50
Table 10. S/N results at different sensitivities	53
Table 11. S/N results at different Off-Axis positions	55
Table 12. Common detection used in photothermal spectroscopy	60
Table 13. Chemical Composition of Titan's Lakes at the Poles and Equator Proposed by Cordier et al	79
Table 14. Excitation beam ranges and selected solutes and solvents of the binary cryo-solutions studied with the extended range TL spectrometer	81
Table 15. Calculation results of benzene and ethane spectral moments	94
Table A.1. Steps for programing the SI-9650 to a particular temperature set point ...	105
Table A.2. Technical specification of chemical substances	118

ACKNOWLEDGMENTS

First and foremost, I want to thank God for my life and all the blessings he have put on my way. Gracias a mi familia, sin ustedes nada de esto sería posible. Gracias por su apoyo incondicional en cada decisión que he tomado en mi vida. Mama, Papa y Leo, gracias por su infinito amor. Los amo con todo mi corazón. Ustedes han hecho que esta aventura lejos de ustedes sea inmensamente más fácil de lo que debió haber sido. Que bonito es saber que la distancia solo nos une con más fuerza.

To my wife Courtney Camejo, our life together could have started a lot better should I have graduated sooner and yet you were always there to put a smile on my face, in the good times but especially in the not so good ones. You and your family have always believed in me. Momma, John, Michael, Candy, Andrew, Jonathan, Mrs. Brown, Mrs. Jean, Margaret, Basil, and all the rest of you, I have nothing but appreciation for all of you.

I would like to thank my mentor Dr. Manzanares for all the efforts and trust he invested on me. He grew to know me to the point of recognizing how harmful frustrations could be on me, and he always did his best to keep me away from them. He taught me a very important lesson in order for me to develop as a scientist, which is about the importance of taking baby steps in any experimental approach, and when things are not going as planned it is always good to get back to the basics. Thank you very much profe.

I have a very special and heartfelt thank you for two other professors, Dr. Darrin Bellert and Dr. David Pennington. Dr. Bellert, if there was such thing as a “second

mentor”, that would definitely be you. I always knew I could count on you when I needed a friend or whenever I found myself being frustrated in the lab. You were always a door away from me. In the other hand, Dr. Pennington has always had an immeasurable faith on me. When I found myself slowing down the most you showed up to push me harder, and it was my huge respect for you what kept me going. Thank you sincerely to both of you.

To my dissertation committee, Dr. John Olson, Dr. Darrin Bellert, Dr. Kevin Shuford, Dr. Touradj Solouki, and Dr. Lesley Wright. Thank you for taking the time to play an important role in my formation as one of your own.

I am deeply grateful to all the rest of my family inside and outside the boundaries of this country. Todos ustedes me han ayudado de alguna manera u otra a poder lograr éste título que tanto esfuerzo y sacrificio me ha costado. Tanto los que están aquí cerquita de mí, como aquellos que están en Venezuela y en España.

I also thank my dearest friends Otsmar, Ricky, Jaime, David, Leomar, who despite the distance always managed to keep encouraging me in their own way. Always giving me a hard time which, at times, I needed to wakeup and finish strong. Estar tan lejos de ustedes no ha sido fácil y sin embargo eso nunca ha debilitado nuestra amistad, por el contrario siempre que necesité de un poquito de distracción y una buena carcajada los tuve aquí con un simple texto. Gracias.

I also want to thank some of my newest friends here in town, whose with I have had so many memorable moments while I went through this PhD program. Sara, Nelson, Katie, Alejandro, Mieke, Sergio, Franklin, Ivanna, Roberto, Daniel, Jenny, and Terrance. Gracias a todos.

To Mary Chacón, thank you so much for your trust. You have been a very important part of why I am making it this far. I always knew I could count on you and indeed you did not fail me. Muchas gracias de corazón Mary.

I am also thankful to Mr. Chris Jaska because without him none of these experiments would have occurred. His help and friendliness was always one call away when any laser would break in the lab, not to mention all the things I learned from him when repairing them. Thanks Chris.

Finally, this research would not have been possible without the financial support of the Robert A. Welch Foundation, and CASPER.

DEDICATION

A mi familia y a la memoria de mi abuela Olga Camejo

CHAPTER ONE

Introduction

Achieving improvements in instrumental techniques and developing new instrumental methods with better detection limits is always an ongoing task in areas for the development of new technologies. Alternative techniques have been developed such as Fourier transform infrared spectroscopy (FT-IR), laser induced fluorescence spectroscopy (LIF), and photothermal techniques, are some of the spectroscopic techniques most widely used for liquid samples. While the first two have their own limitations including detection limit and the fluorescent nature of the sample, respectively, the latter has been used for the quantification of trace components in liquid samples. On the other hand, the study of gas samples is often related to fundamental spectroscopic studies because of the broadening effect of the spectral band, caused by molecules adjacent to the analyte, is usually diminished or nonexistent.¹ Therefore, very sensitive techniques have been developed, including photoacoustic spectroscopy (PAS),² thermal lens spectroscopy (TLS),³ intracavity laser absorption spectroscopy (ICLAS)⁴ and cavity ring-down spectroscopy (CRDS).⁵ Among these, the CRD technique has proven to be a valuable addition because of its high sensitivity and relatively simple experimental set-up.^{5,6} The main advantage of CRD spectroscopy over traditional absorption spectroscopy is that it does not depend on intensity nor the power of the light source, and hence intensity fluctuations are not a source of error. The detection limits of the CRD technique are directly related to the time a sample spends absorbing the

radiation of the excitation source. That time can be altered by the design of a long pass cell. This means that as long as the detection is fast enough, lower and better detection limits can always be achieved.

This work discusses the instrumental aspect of both TLS and CRDS techniques as two powerful tools for the study of liquid and gaseous samples, respectively. In some cases it also shows the different experimental variations, as well as some derived methods to increase the sensitivity of detection.

Vibrational Overtone Spectroscopy

Molecular Vibrations

The analysis of motion of atoms in a molecule becomes complicated as the number of atoms in the molecule increases. For diatomic molecules a simple diatomic oscillator can easily describe their motion. Molecules with N atoms have $3N$ degrees of freedom, three of them correspond with the translational motion of the molecule in space and three more represent its rotational motion on the three x , y , and z axes. The remaining $3N-6$ degrees of freedom represent the number of vibrational modes in the molecule. In the case of lineal molecules this expression turns into $3N-5$ since it only has two rotational and three translational degrees of freedom.^{7,8}

As an initial approximation towards understanding the inherent vibrational behavior of the atoms in a molecule, it is useful to think of a normal mode of vibration. Normal mode means that all atoms move in phase and with the same frequency. Then all atoms reach their position of maximum displacement at the same time, and hence pass through the equilibrium position at the same time as well.⁹ Under these conditions, the

vibrational motion of the atoms can be approximated as harmonic displacements. The potential energy (V) associated with a harmonic oscillator can be calculated by:

$$V = \frac{1}{2}k(x - x_e)^2 \quad (1)$$

where k represents the force constant of the oscillator, x_e is the equilibrium internuclear separation, and x is the internuclear separation at any given time. The force constant is related to the frequency (ω) of the harmonic oscillator according to equation 2, where μ represents the reduced mass.

$$\omega = \frac{(k/\mu)^{1/2}}{2\pi} \quad (2)$$

The vibrational energy (E_v) is:

$$E_v = h\nu \left(v + \frac{1}{2} \right) \quad (3)$$

where h is Planck's constant, ν is the fundamental frequency and v is the vibrational quantum number. Vibrational frequency is often measured in units of cm^{-1} .

This harmonic oscillator model is a fair approximation to predict vibrational energies of the lower vibrational states of a diatomic molecule, but it fails to do so as we move our attention towards higher vibrational states. As shown in Figure 1, the harmonic oscillator approximation suggests that a bond between two atoms cannot be broken regardless of the energy of the vibration.

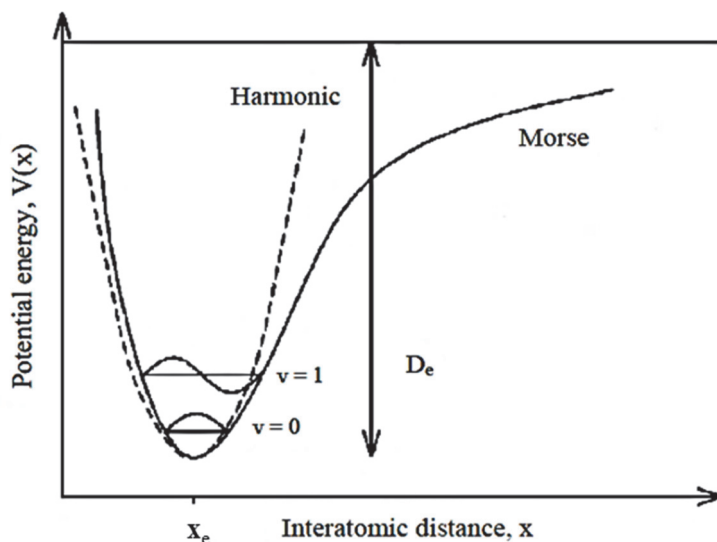


Figure 1. Harmonic and Morse potential energy functions for a diatomic oscillator.¹¹

The molecular vibrations behave anharmonically rather than harmonically. The Morse function can describe that anharmonic motion of atoms in a molecule, and the potential energy can be calculated as follows:

$$V(x) = D_e(1 - e^{-aq})^2 \quad (4)$$

where D_e is the depth of the potential well, as shown in figure 1, a is an empirical constant that relates to the curvature of the function beyond the equilibrium distance x_e , and q is the difference in the position x with respect to x_e ($q = x - x_e$). The Morse function successfully predicts the dissociation of the bond when the two atoms taking part in a bond are forced apart, and it also shows the harmonic behavior when the atoms remain closer to the equilibrium distance. These facts are in agreement with the experimental observations.⁹ For an anharmonic oscillator the vibrational energy states are described by:

$$E_v = hc\omega_e \left(v + \frac{1}{2}\right) - hc\omega_e x_e \left(v + \frac{1}{2}\right)^2 + hc\omega_e y_e \left(v + \frac{1}{2}\right)^3 + \dots \quad (5)$$

where $\omega_e x_e$ and $\omega_e y_e$ are the anharmonicity constants associated with the first and second corrections to the potential energy curve. The Taylor series shown in equation 5 makes the vibrational levels move closer to each other as ν increases, until the point of dissociation.

When molecules are promoted from their vibrational ground state ($\nu = 0$) to $\nu = 1$ they undergo their fundamental transition. These transitions can be registered in the infrared (IR) region of the electromagnetic spectrum. When the transitions occur towards higher vibrational levels these are defined as overtone transitions; therefore, when molecules move from $\nu = 0$ to $\nu = 2$ ($\Delta\nu = 2$) this is known as the first overtone, from $\nu = 0$ to $\nu = 3$ ($\Delta\nu = 3$) is the second overtone, and so on. As we move higher in overtones, these bands start moving towards the near infrared (NIR), visible (Vis.), ultra-violet (UV), and so on; they require larger energy changes to occur.

The vibrational transitions experienced by a given bond depend on the magnitude of the dipole moment operator, μ , and the interatomic distance. The dipole moment is expressed in a Taylor series as shown in equation 6.¹⁰

$$\mu_{(x_i)} = \mu_0 + \left(\frac{\partial\mu}{\partial q}\right)_{q=0} \cdot q + \left(\frac{\partial^2\mu}{\partial q^2}\right)_{q=0} \cdot q^2 + \left(\frac{\partial^3\mu}{\partial q^3}\right)_{q=0} \cdot q^3 + \dots \quad (6)$$

The intensity of a transition is proportional to each term in the expansion. For example, the fundamental ($\Delta\nu = 1$) is proportional to the first derivative of the dipole moment, the first overtone ($\Delta\nu = 2$) is proportional to the second derivative which is smaller in magnitude, and so on. Because of this, the intensities are in the order:

$$I_{\Delta\nu=1} > I_{\Delta\nu=2} > I_{\Delta\nu=3} \dots \quad (7)$$

Figure 2 shows spectra of the $\Delta\nu = 2$, $\Delta\nu = 3$, and $\Delta\nu = 4$ overtone transitions of methane, recorded at 87 K. Notice how the third overtone is barely showing in the bottom trace, and how an enlargement of 100x was needed to see the details in the bands. More sensitive techniques would be required in order to register $\Delta\nu = 5$, and $\Delta\nu = 6$.

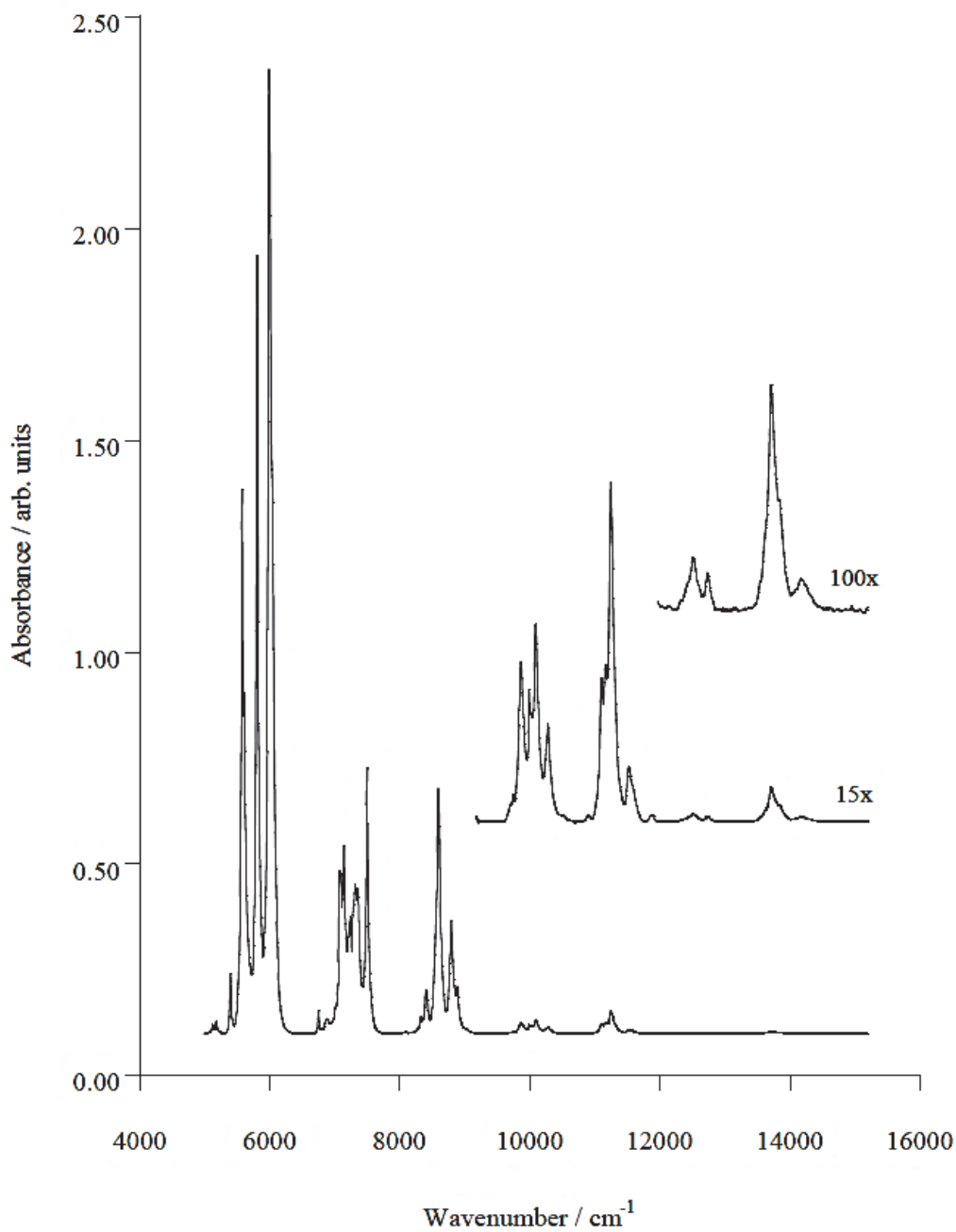


Figure 2. Vibrational overtone spectra of a solution of methane in argon at 87K acquired with a FT-IR spectrophotometer.

Defining the energy as $G(v) = E_v/hc$ in wavenumbers (cm^{-1}), the energy of a vibrational transition is usually calculated using only the first order anharmonicity term and subtracting the energy of the ground state from that of the excited state of interest. This results in equation 8, as follows:

$$\left(\frac{\Delta G_v}{v}\right) = (\omega_e - \omega_e X_e) - \omega_e X_e \cdot v \quad (8)$$

where the energy (G), harmonic frequency (ω_e), and anharmonicity ($\omega_e X_e$) have units of wavenumber (cm^{-1}). The anharmonicity as $\omega_e X_e$, can be obtained experimentally by plotting $(\Delta G_v/v)$ against v , this is also known as the Birge-Sponer plot. The anharmonicity can be obtained from the slope of this linear plot, whereas the harmonic frequency can be obtained from its intercept.

Detection Techniques

Given the weak intensity of overtone transitions, highly sensitive detection techniques are required to measure them. Traditional absorption spectroscopy, mostly in the IR region, has been used for this purpose. Although, as already mentioned on Figure 2, signal enhancement is often necessary in order to identify higher overtones. Developed by O'Keefe and Deacon,¹³ cavity ring-down spectroscopy (CRDS) is a highly sensitive absorption spectroscopy technique capable of measuring very weak absorptions. Therefore, it is widely used in overtone spectroscopy. As will be further explained in Chapter Two, one of the inherent limitations of CRDS is that liquid samples cannot be studied with this method, as these may alter the high reflectivity features of the optics involved, which affects the high sensitivity of this technique. Despite some efforts to

study liquid and solid samples with CRDS,^{14, 15} typically gas samples are the most widely studied with this technique.

Some photothermal methods are also capable of measuring very weak signals, and this makes them suitable for the study of overtones.^{16, 17} Thermal Lens Spectroscopy (TLS) is a photothermal technique that has been widely used in our laboratory¹⁸, and elsewhere,¹⁹ as an important tool in overtone spectroscopy. This technique is based on the photothermal effect, and can ideally be used to study samples in any physical state. Nevertheless, the photoelectric effect depends on the density of the sample and because of this, the use of TLS for gas samples would be extremely challenging. Hence, TLS is most commonly used for liquid samples.

In our laboratory we have developed both CRDS^{20, 21} and TLS^{18, 22} for low temperature measurements and cryogenic samples. These highly sensitive instrumental techniques, complemented in some cases by FT-IR and UV-Vis, are used for overtone studies of either liquid or gaseous samples. Hereafter, we will limit our discussion to the instrumental details of these techniques, as well as some of their applications.

Dissertation Overview

Chapter Two presents the fundamentals of the Cavity Ring Down technique, followed by the explanation of the experimental setup of the PS-CRD instrument. Descriptions of the optical layout are provided as well as instrumental descriptions. Off-axis alignment is also covered in this chapter.

Chapter Three presents the results obtained with the PS-CRD technique described in Chapter Two. Evaluation of some important experimental parameters including sensitivity, acquisition pause, and pre-amplification gain, and their effect on the quality

of the spectra obtained with this instrument are discussed, as well as the evaluation of on-axis versus off-axis conditions has been explored. This was accomplished by measuring the rotational-vibrational spectrum of the γ atmospheric band of O₂. An explanation of the features of this band is provided at the beginning of the chapter, and conclusions about the empirical calculations made here are offered at the end of it.

Chapter Four presents the fundamentals of the TL technique, and the experimental setup of the TL instrument designed for measurements at cryogenic temperatures. A new instrument design for this technique for the measurement of multicomponent cryogenic solutions is introduced, and its usefulness in the study of selected areas of astrochemistry is demonstrated. The ($\nu = 0 \rightarrow 4$) vibrational transitions of ethane, and ($\nu = 0 \rightarrow 5$) vibrational transition of benzene are observed at cryogenic temperatures.

Chapter Five introduces the calculation of the first and second spectral moments of the C-H overtone transitions of benzene and ethane calculated from the TL spectra obtained in Chapter Four. These calculations are described as useful tools to complement our TL experiment, and to study the asymmetry of spectral bands often obtained with the thermal lens spectrometer.

Chapter Six contains general conclusions about the two main absorption techniques presented in this work, as well as it offers a research outlook for future work.

The Appendices present a brief description of the UV-visible apparatus used as complementary technique to the thermal lens experiments presented in this work, which is focused on the study of cryogenic solution. General information for the CRD and TL instruments is also found in these appendices. This includes procedures for the start-up and alignment of the CRD systems for the exponential decay and phase shift methods, as

well as procedures for cryostat operation, and the maintenance of the HR mirrors. Details about the code built to acquire the data in each of the experiments mentioned in this manuscript are also shown in this section.

CHAPTER TWO

Cavity Ring Down Spectroscopy

This chapter presents the fundamentals of the Cavity Ring Down (CRD) technique, and describes the instrumental setup utilized throughout the course of the research. A complete description of each component, from the cell design to the PS-CRD instrumental setup is provided. It also includes the experimental procedures carried out with this sensor. The off-axis alignment of the cavity is also presented.

Cavity ring-down (CRD) spectroscopy is a direct absorption technique, which can be performed with either pulsed (exponential decay CRD)¹³ or continuous (phase shift CRD)²³ light sources. Due to its extremely long effective pathlength (10 – 80 kilometers) within a one meter cavity, this technique has a significantly higher sensitivity than obtainable in conventional absorption spectroscopy.²⁴

CRD spectroscopy consists of a laser source, an optical cavity, and a detector to measure the exiting light from the optical cavity. Figure 3 depicts a characteristic pulsed cavity ring down diagram.

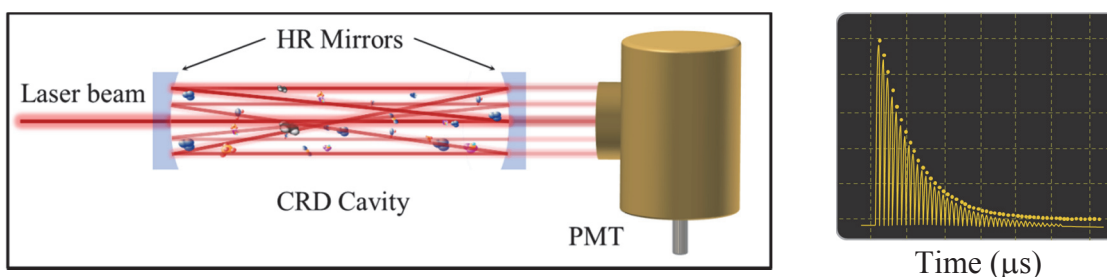


Figure 3. Pulsed Cavity Ring Down Diagram

In a typical ring down experiment the laser light is injected into a cavity sealed by two highly reflective mirrors, each with a reflectivity greater than 99.99 %. When the mirrors are aligned in fine parallel configuration the incoming laser pulse bounces back and forth between the mirrors, leaking a small portion (less than 0.01%) of its intensity on each bounce, and until the beam has left the cavity. The beam stays trapped in the cavity for a certain amount of time, usually in the range of micro seconds, causing the long optical path length.

Figure 3 shows the decay of the beam as it leaks out of the cavity, measured by a photo-sensitive detector placed behind the output mirror. This is known as the ring-down event. If short laser pulses are used, a very *fast* detector will see a train of pulses within the exponential decay envelope, but the time response of detection electronics usually means the pulses are smoothed into a single exponential curve. This is shown in Figure 4.

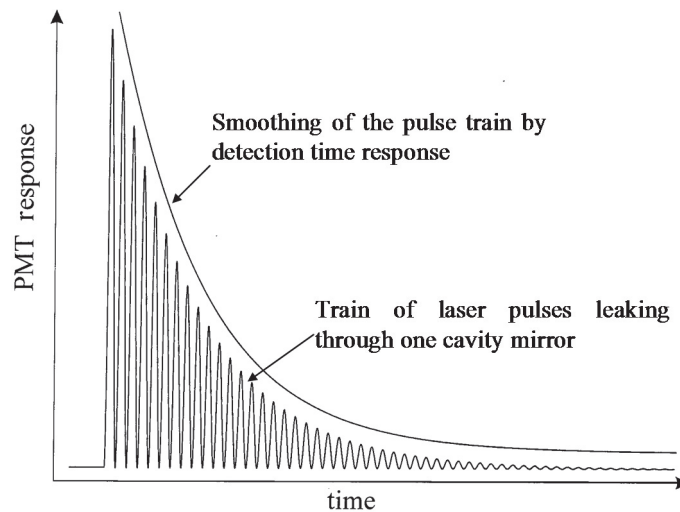


Figure 4. Exponential decay of laser light within the ring-down cavity²⁵

The intensity (I) of the light transmitted out of the cavity decreases as a function of time (t) and can be characterized as:

$$I_{(t)} = I_0 e^{-(t/\tau)} \quad (9)$$

where I_0 is the initial light intensity detected and τ is the decay constant. This decay constant (τ) is commonly referred to as the ring-down time. This value can be from $1\mu\text{s}$ to $100\mu\text{s}$ or more depending upon mirror reflectivity.

Cavity ring down spectroscopy can be done using the two most common methods which are the exponential method and the phase shift method. Both methods can be used to obtain τ . The exponential CRD detection method uses an exponential fitting of the output signal from the cavity to measure the decay time. An exponential fitting program is used to obtain τ . Figure 5 shows a schematic of the system shown for the first time by O’Keefe and Deacon¹³ where this detection method was used.

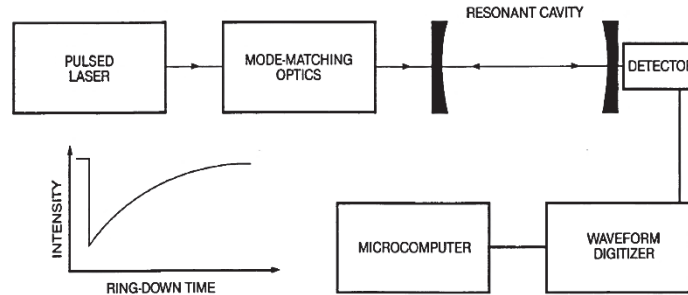


Figure 5. Schematic representation of the experimental layout presented by O’Keefe and Deacon.¹³

The PS-CRD method was first developed by Herbelin et. al.²⁵ This method measures the phase-shift of a modulated beam from the output beam of the cavity with respect to the modulated beam, or reference beam, before entering the cavity. The phase shift angle is related to the ring down time by the equation

$$\tan \theta = 2\pi f\tau \quad (10)$$

where θ is the phase shift angle and f is the frequency of modulation.

In Figure 6, we can see how the radiation of a CW tunable laser source has been modulated, and is incident upon the optical cavity. Typically, an acousto-optic or an electro-optic modulator can be used to create a square modulation frequency shape. Modulating the CW laser output produces an on/off pattern which translates into a filling/emptying of the cavity.²⁶

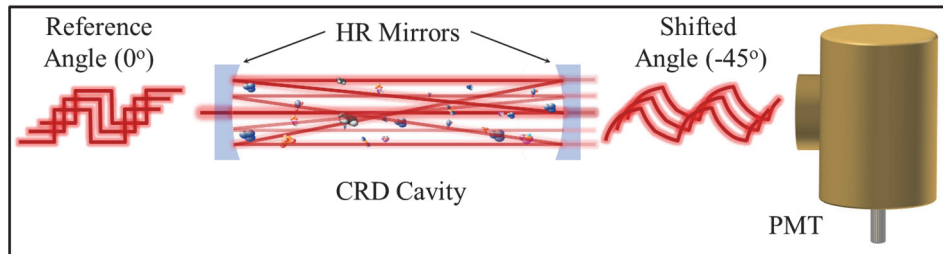


Figure 6. Phase shift cavity ring down diagram

The output signal from the cavity in Figure 6 resembles a shark fin when the angle is approximately 45° , and so it will be referred to herein. A closer and more detailed look of this signal is shown in Figure 7. This figure illustrates how the positive slope of the shark fin signal relates to the radiation building up inside the cavity, as the reference signal is entering it (bottom trace). Then the phase shift occurs while the beam traverses the cavity (top).

Experimentally, the PS-CRD method results in an angle of -45° after the initial alignment of the empty cavity. This condition is critical as it relates to the baseline of all the spectra that will be obtained thereafter. In other words, the closer this condition is met, the flatter the baseline will be.²⁷ This -45° angle is given by the characteristic shape of the $\tan(\theta)$.

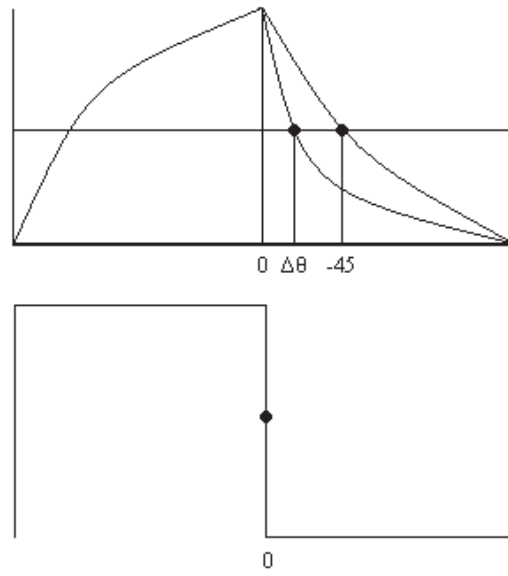


Figure 7. PS-CRD signal (top), Reference signal (bottom)

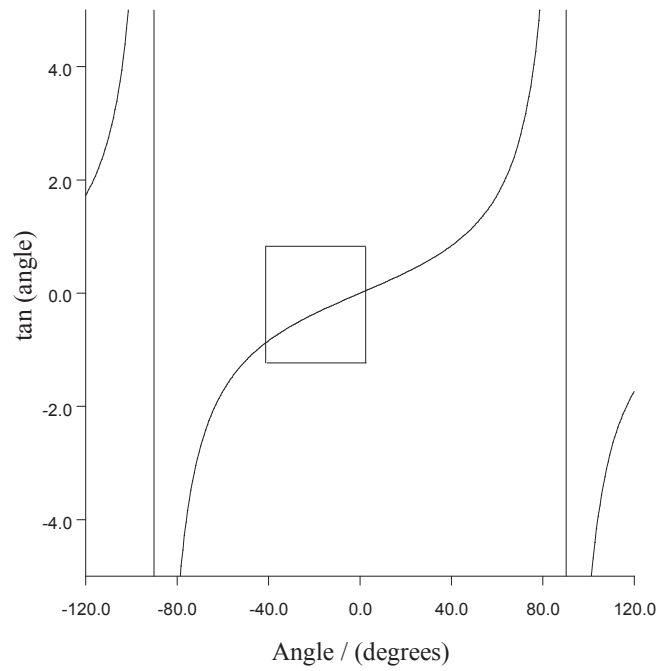


Figure 8. $\tan(\theta)$ versus θ graph

Figure 8 shows a plot of the $\tan(\theta)$ versus angle θ , where the boxed area shows to be fairly linear from -30 to -50 degrees. Angles greater than 45 are avoided because they would induce measurements with a non-linear response of the PS-CRD system.

CRD and Absorption Spectroscopy

The absorption of light by a sample is described by the Beer-Lambert law. This establishes a quantitative relationship between the intensity of a spectral feature and the frequency-dependent absorption properties of the sample:

$$I = I_0 e^{(-\sigma Cl)} \quad (11)$$

where I is the transmitted intensity, I_0 is the incident intensity, σ is the absorption cross section of the sample at the wavelength of the measurement, C is the concentration of the absorber and l is the sample pathlength. The product of C and σ is the absorption coefficient, α , and the absorbance is defined as σCl . From equation 11, it can be demonstrated that it is plausible to detect very small concentrations of a sample, or very weak absorption cross sections, as long as the pathlength is long enough.^{6, 25} CRD provides that long pathlength to make direct absorption measurements of either trace amounts or weak absorptions.

The ringdown time, τ , of an empty cavity is related to the distance between the mirrors and the reflectivity of the mirrors by the equation below:

$$\tau = \frac{L}{c(1 - R)} \quad (12)$$

where L is the distance between the two mirrors, c is the speed of light, and R is the reflectivity of the mirrors. Since c and L are known quantities, then τ is a direct measure of the mirror reflectivity (R).

When there are absorbing species present in the cavity, these will induce loss of the radiation resonating inside of it due to sample absorption. This speeds up the decay of the remaining trapped light. If the absorption follows Beer-Lambert law, the light intensity will still decay exponentially, with time dependence given by:²⁸

$$I(t) = I_0 \exp\left\{-\frac{t}{\tau} - \alpha ct\right\} \quad (13)$$

where α is the molecular absorption coefficient at a given wavelength, with dimensions of cm^{-1} , and c is the speed of light. The product of c and τ is the pathlength over which the absorption is measured. The decay rate is now given by

$$\frac{1}{\tau'} = \frac{1}{\tau} + c\alpha \quad (14)$$

Thus, the ring down time for a cavity filled by an absorbing medium, τ' , where the Beer-Lambert law is valid is described as:

$$\tau' = \frac{L}{c[(1-R) + \alpha(\nu)L]} \quad (15)$$

During a scan with a tunable laser in the absorption region of the sample, the ring down time (τ) is obtained from the exponential fitting, or the phase shift angle, of the radiation leaking out of the cavity.

The decay time of a cavity filled with an absorbing medium is a combination of the sample and the background (see equation 16). In order to obtain the absorption of the sample, the inverse of the decay time of the empty cavity ($1/\tau_0$) is subtracted from the inverse of the decay time of the filled cavity ($1/\tau'$)

$$\alpha(\nu) = \frac{1}{c} \left(\left(\frac{1}{\tau'(\nu)} \right) - \left(\frac{1}{\tau(\nu)} \right) \right) \quad (16)$$

The calculated absorption ($\alpha(\nu)$ in cm^{-1} units) is plotted as a function of the wavenumber (cm^{-1}) to show the spectrum of the sample.

Stability of an Optical Cavity

Some conditions are required to observe CRD signal. A CRD experiment requires achieving a stable optical and non-confocal cavity. An optical cavity with two mirrors is stable geometrically when the light is refocused within the cavity after successive reflections from the mirrors, this means that the optical energy is contained, or trapped, within the cavity. Achieving a stable optical cavity depends upon the known as g parameters of the mirrors and cavity itself.⁵ Specifically:

$$0 \leq g_1 g_2 \leq 1 \quad (17)$$

where g_1 and g_2 are defined as:

$$g_1 = \left(1 - \frac{L}{r_1}\right) \quad (18)$$

$$g_2 = \left(1 - \frac{L}{r_2}\right) \quad (19)$$

where r_1 and r_2 are the radiuses of curvatures of the mirror surfaces.

A non-confocal system offers a degree of mechanical flexibility in order to allow the mirrors to move slightly without jeopardizing the alignment with respect to each other. This is advantageous because should the mirrors be at each other's focal length, any mechanical disturbance would result in a loss of alignment. This approach is defined by equations 20 and 21:

$$r < L < 2r \quad (20)$$

or

$$0 < L < r \tag{21}$$

where r is equal to their radius of curvature, assuming $r=r_1=r_2$. Figure 9 shows two configurations for a stable optical cavity system with mirrors placed outside of the radius of curvature and with mirrors placed within radius of curvature, respectively. The structure mode of such a cavity can be made very dense, especially when the L/r ratio is chosen to be an irrational number.²⁹

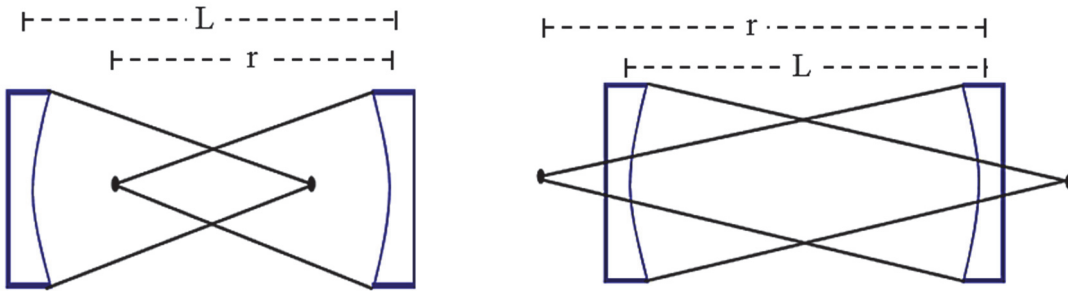


Figure 9. Stable optical cavities. (a) with mirror placed $r < L < 2r$, and (b) with mirror placed $0 < L < r$

Cavity Modes

The modes in which a cavity is operating are important in CRD. When a laser beam is incident upon an optical cavity, modes of light are formed. These can be longitudinal or transverse modes (TEM). Transverse mode describes the cross sectional profile of a beam. Longitudinal modes, also known as axial modes, determine the resonant oscillation frequencies that satisfy the wavelength requirements of the cavity along a given optical path.⁵ When the frequency spacing of the longitudinal modes of the cavity (the cavity free spectral range, FSR) exceeds the width of the spectral bands being studied, then the radiation with the appropriate frequency for excitation of certain spectral

lines will not be present in the cavity, causing the resultant spectrum to be absent of important absorption features.³⁰

Comparing the mode spacing against line width of the continuous radiation provides an idea of the response of an optical cavity to a scanning PS-CRD system. The frequency spacing ($\Delta\nu$) of longitudinal cavity modes (FSR) is defined as:

$$\Delta\nu = \frac{c}{2L} \quad (22)$$

where c is the speed of the light.

Table 1 shows the laser resolutions and the calculated longitudinal mode spacing for some common laser sources used in our laboratory. It must be noticed that the mode spacing is much smaller than the laser resolution, giving us an overlapping multi-mode configuration.³¹ This allows continuous scanning experiments to be carried out with the PS-CRD method.

Table 1. Mode Spacing Calculations

Cell length (cm)	Dye Laser Resolution (cm ⁻¹)	Ti:Sapphire Resolution (cm ⁻¹)	Longitudinal Mode Spacing (cm ⁻¹)
43.5	0.07	0.17	0.0115

Off-Axis Alignment

Cavity ring down requires of the accurate alignment of the laser beam along the center axis of the cavity. For PS-CRD systems based on this on-axis alignment, the coherent beam couples into the cavity on average only 5% - 10 %³² of the time. At times, this coupling-time efficiency can be improved experimentally with additional laser

frequency dithering³² and modulation of the cavity length. Cavities with irrational number of cavity length to mirror curvature radius can be used.²⁹

Another resource to increase the coupling efficiency consists of performing an off-axis alignment of the cavity. This off-axis alignment involves injecting the laser beam into the cavity at an angle to the optical axis. Under this condition the beam may couple into the cavity continuously up to 100% of the time.^{33, 34} Also, the off-axis alignment decreases the cavity FSR and excites a large number of transverse cavity modes. The off-axis configuration spatially separates the multiple reflections within the cavity until the reentrant condition is fulfilled, that is the time at which the ray begins to retrace its original path through the cavity. This condition is dictated by the specific curvature and spacing of the mirrors forming the cavity. Any stable cavity that follows the condition shown by equation 15 can achieve stable off-axis paths.³⁵

In order to maximize the number of spots that can be accommodated on the mirror surface without overlapping, the beam spot should be a circle near the edge of the mirrors, as shown in Figure 10.³⁶

The angle of a round trip rotation of the beam spot (2θ) is determined by the geometry of the cavity and is given by³⁷

$$\cos \theta = 1 - L / r \quad (23)$$

The reentrant condition is satisfied if³⁷

$$2m\theta = 2n\pi \quad (24)$$

where m is the number of optical round-trip passes and n is an integer, and after every m round trips the ray starts to retrace its path.

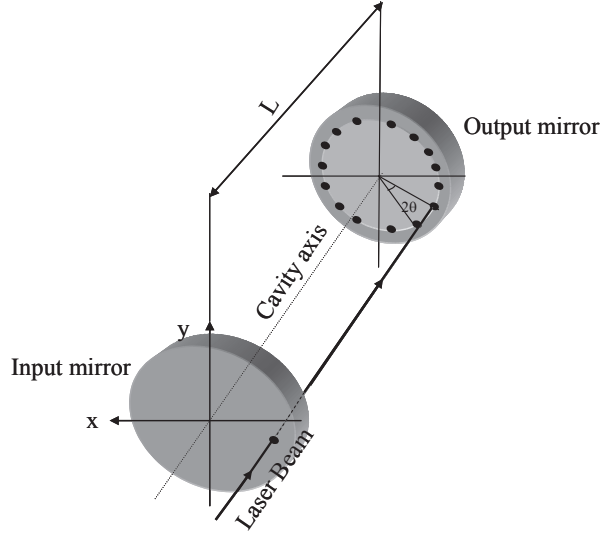


Figure 10. Off-axis beam propagation³¹

It can be said that the longitudinal mode spacing, $\Delta\nu$, becomes similar to one that is m times longer. The longitudinal mode spacing of a cavity aligned off axis ($\Delta\nu_{\text{off-axis}}$) is

$$\Delta\nu = \frac{c}{m2L} \quad (25)$$

In equations (24) and (25), m was determined by considering the geometrical parameters of the cavity. Experimentally, m and n can be determined depending on the beam alignment. Table 2 shows m and n values obtained for two different radius of curvatures, when $L = 89.7$ cm, and $\Delta\nu$ for cavity aligned on-axis and off-axis.³¹

Table 2. Comparison between $\Delta\nu_{\text{off-axis}}$ and $\Delta\nu_{\text{on-axis}}$

R (cm)	m	n	$\Delta\nu_{\text{off-axis}}$		$\Delta\nu_{\text{on-axis}}$	
			$\text{cm}^{-1} 10^{-4}$	MHz	$\text{cm}^{-1} 10^{-4}$	MHz
600	41	5	1.4	4.1	55	167
100	26	8	2.1	6.4		

Figure 11 shows predicted longitudinal mode spacing for an 89.7 cm cavity aligned on axis, Figure 11 (a), and off-axis, Figure 11 (b), when the reentrant condition is satisfied after 41 round trips.

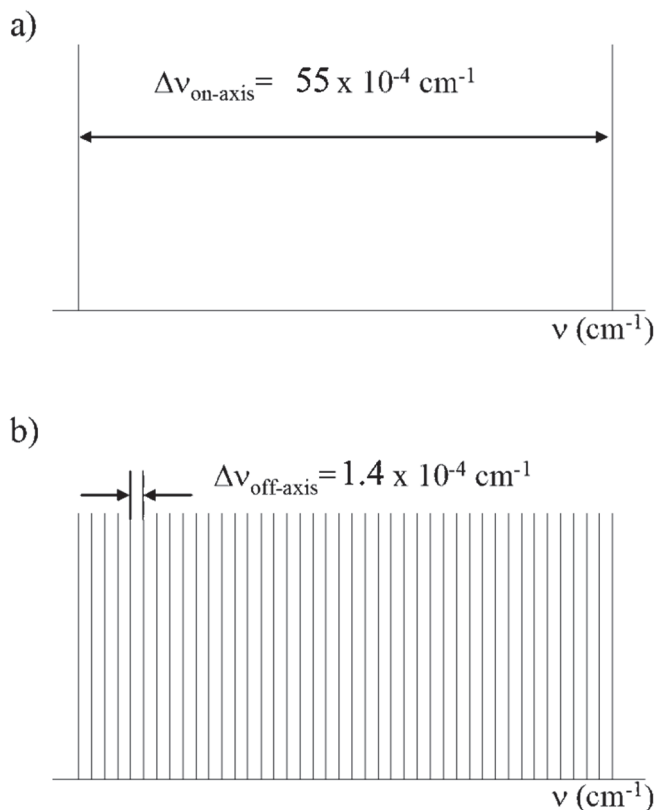


Figure 11. Predicted $\Delta\nu$ for a 43.5 cm cavity aligned (a) on axis and (b) off-axis when the reentrant condition is satisfied after 41 round trips.³¹

CRDS Instrumentation and Procedures

CRD Cell Design

The sample cell is composed by a central cubic cell with two attaching arms. The central cubic cell was made of yellow brass whereas the arms are made of aluminum since these materials have good thermal conductivities and expansion coefficients at low temperatures, which make possible the use of this set-up for studies at temperatures different from room temperature.^{26, 27} The cubic core of this cell measures 40 x 40 x 40

mm³ and it serves as the main point of attachment of the cell with the rest of the CRD instrument. The aluminum arms are 428.5 mm in length and 12.7 mm in internal diameter. These arms are attached to the central cubic core with screw head bolts and O-ring seals. The resulting cell is 897 mm in length and 12.7 mm in diameter. Stainless steel tubing is used to connect the cell to the external gas sample preparation system. Figure 12 shows the sample cell separated in its several components, as well as the respective dimensions.

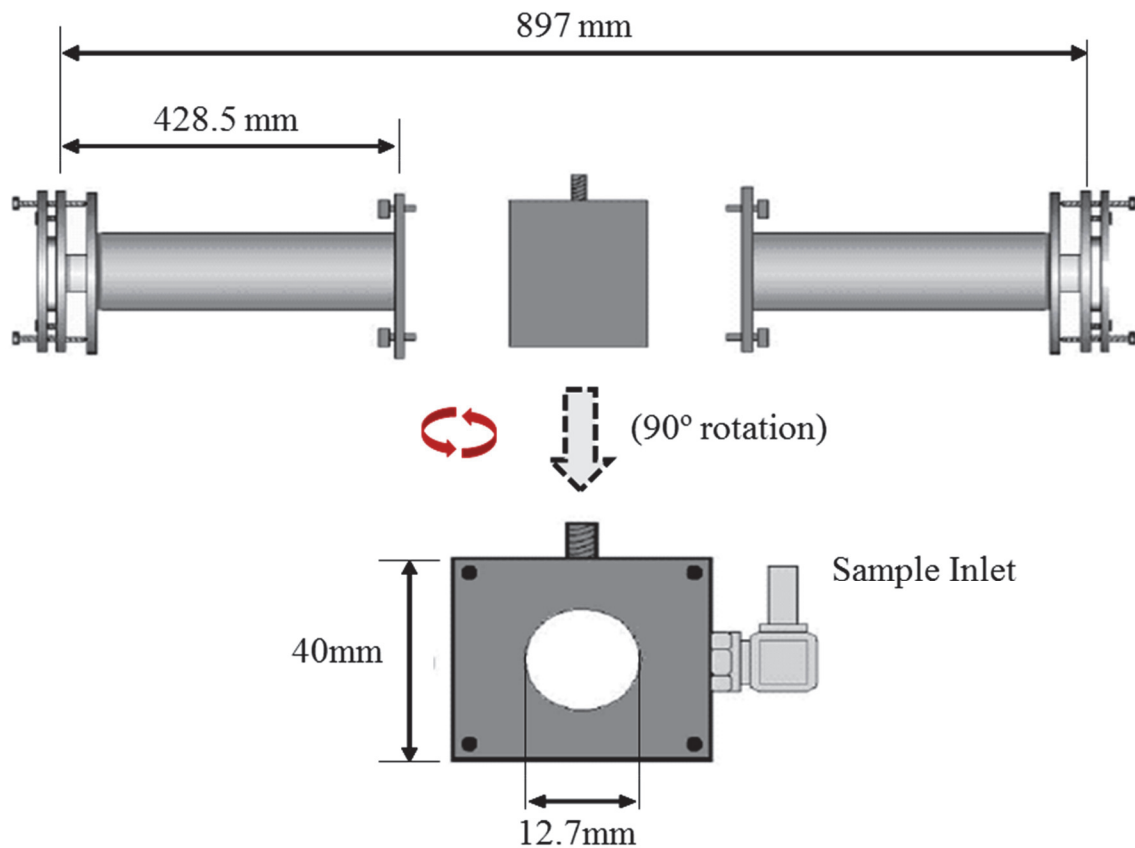


Figure 12. Schematic side view (top) of the CRD cell design, (bottom) of the center cubic core.

Figure 13 (top) shows a view of the left-hand side of the arm. Each arm consists of two attachment flanges constructed from an Aluminum solid piece. The opening in the center of each flange is 12.7 mm wide, as well as the internal diameter of the cell. Between the attachment flange and the high reflector (HR) mirror, an Aluminum mirror protector is used to prevent the mirror from breakage during the alignment process. The dimensions of this piece depend on the mirror dimensions, and it is precisely cut to accommodate the mirror based upon its thickness and diameter. The HR coating on the mirrors must also be protected from pressure and friction; hence, a rubber O-ring seals the cell from the outside and also protects the mirror from mechanical damage. This rubber O-ring must be precisely located concentric with the 12.7 mm opening in the cell and it must be wide enough to ensure that no leaks will be present when the assembly is complete. In cases when the experiment is intended for low temperature measurements, the rubber O-ring must be replaced by Indium O-rings to ensure proper sealing.

At the bottom of Figure 13 it can be seen a recommended configuration for the attachment and fine alignment screws. It is desirable to design the arms and flanges so that the fine alignment screws result in North, South, East, and West positions. The thread of the attachment screws is $\frac{1}{4}$ "-32, whereas that of the alignment screws is $\frac{1}{4}$ "- 80. The system is rigid but there is a small margin of flexibility that allows aligning the mirrors with respect to the laser beam by rotating the alignment screws.

Three different sets of CRD mirrors are used depending on the wavelength region of interest. All of them have 20.32 mm in diameter. Table 3 summarizes bandwidth, radii of curvatures and listed reflectivity for CRD mirrors.

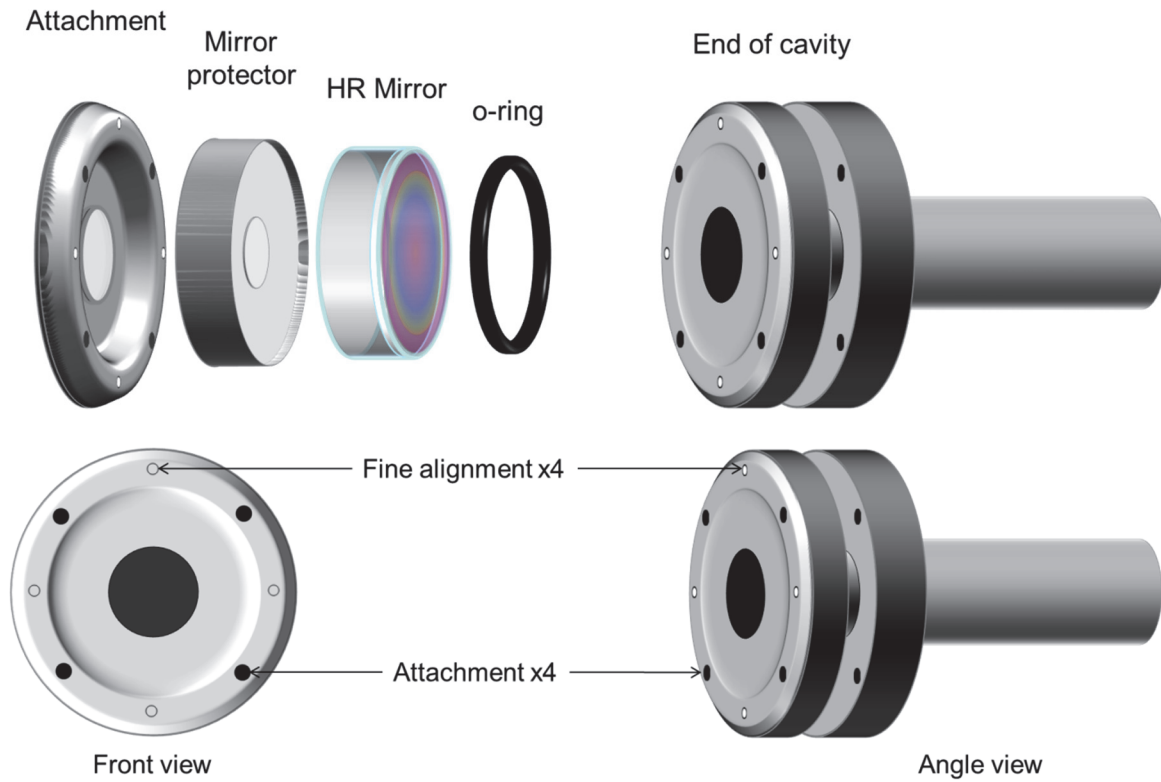


Figure 13. Expanded view of the left arm, showing the O-ring, HR mirror, as well as the mirror protector, and flange attachment (top); screws positions needed to hold and finely align the mirrors.

Table 3. Center wavelength, bandwidth and radii of curvatures for CRD mirrors

Mirror Set	Bandwidth nm	Radius of Curvature m	Listed Reflectivity %
Los Gatos 760 nm	740 - 800	6	99.995
Los Gatos 722 nm	695 - 745	6	99.995
Newport 620 nm	583 - 663	1	> 99.9

Instrumental Setup for PS-CRD Spectroscopy

The experimental setup is shown in Figure 14. The pump laser is a solid state, Millennia V laser (Spectra Physics) providing single wavelength (532nm) at a power of 5W. This laser is used to pump a continuous wave Coherent CR-599 dye laser with a solution of Rhodamine 6G as the fluorescent medium, resulting in a scanning range between 599 to 690 nm or 14493-16695 cm^{-1} . The wavelength tuning of this dye laser is accomplished with a birefringent filter driven by a stepper motor. This stepper motor is controlled remotely from the computer using LabVIEW®. The output beam of the dye laser is modulated into a square wave with a Conoptics model 350-50 electro-optic modulator (EOM). The EOM is driven by a Stanford Research Systems (SRS) function generator, and the modulation frequency depends upon the final alignment conditions of the cavity. The beam is injected on-axis into the optical cavity and aligned following the steps explained in Appendix B. The leaked radiation out the back of the cavity is focused by a lens and detected by a Newport 70680 photomultiplier tube (PMT), which is powered by a high voltage power supply operated between 700 V – 1000 V.

A combination of movable mirrors and beam splitters is used before and after the cavity to bypass the beam around the cavity and into the PMT. The PMT response is sent to a Stanford Research Systems (SRS) Low-Noise Pre-Preamplifier model SR 560 for signal amplification and conditioning. The signal is then sent to an SRS 830 Lock-In amplifier, where the phase angle between the bypassed beam and the leaked beam is determined. The data from the SRS 830 is sent to a computer via a GPIB interface where it is also processed using a LabVIEW® code specifically written for this system. The

whole system sits on top of a Newport 4' by 10' by 8' optical table which has vibration isolation legs to eliminate random mechanical noises.

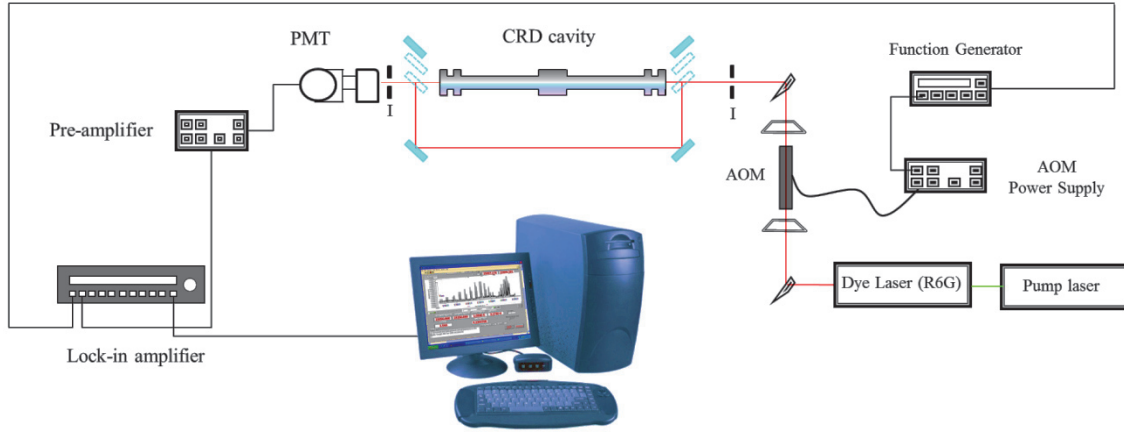


Figure 14. Experimental setup of the PS-CRD spectrometer. Key: EOM, electro optical modulator; I, iris; L, plane-convex lens; PMT, photomultiplier tube.

PS-CRD Signal and Signal Conditioning

Obtaining a low noise phase-shift signal not only depends upon the accuracy of the alignment of the cavity, but also on several instrumental devices. The resulting sensitivity of the instrument is determined by the noise of the background signal and hence, every effort must be done to decrease the noise within the PS signal.

In order to detect a PS-CRD signal after the optical cavity we must first modulate the laser beam going into the cavity, this provides a square signal measurable by the SRS 830 lock-in amplifier. This is accomplished by modulating the beam into a square wave using the EOM. In our experiments, the modulation frequencies varied between 21 - 25 KHz.

The signal resulting from the cavity is detected by the PMT. The response curve of the PMT showed a maximum detection range at around 1000 volts. Therefore, most

signals were detected using either a 900 V or 1000 V setting. The PMT uses a 50 ohm load resistor mainly because of two reasons; first, the resistor protects the PMT from a charge buildup which, upon connection to a measurement device, could be released rapidly causing damage to the PMT. Second, the resistor behaves like an RC circuit that responds like an exponential function with a time constant equal to:

$$\tau = RC \quad (26)$$

where R is the resistance in ohms and C is the capacitance in farads. This is useful to determine the response of the system to changes in the signal.

The signal is sent from the PMT to a SRS SR560 pre-amplifier where any random noise can be filtered out of the signal. The latter is also amplified at this stage. The typical settings for the SR560 are a gain of 1, low noise filter mode with the high and low pass filter set at 6 dB, and DC coupling. The cutoff filters are set from 300 Hz to 300 kHz, which makes possible to reduce the degree of noise in the measurement without interfering with the signal of interest. To ensure that the cutoff filters are far enough away from the modulation frequency of the laser beam, the cutoff filters are first set very wide. The filters are then narrowed toward the modulation frequency until a noticeable change in signal and angle are observed. The filters are then backed off two settings to avoid signal aliasing. After the pre-amplifier the signal is also sent to an oscilloscope. The oscilloscope is used to identify the signal for alignment purposes.

The lock-in amplifier is used to extract the phase angle from the signal. It requires a reference frequency supplied by the frequency generator and a reference phase angle to determine the phase angle of the CRD signal. The reference phase angle is obtained by bypassing the optical cavity and sending the beam to the PMT. This results in a signal

that should resemble a square wave with the modulation frequency value. It is advisable to use optical density filters to dim the intensity of the bypass beam without lowering the power of the pump laser. The intensity of this beam should be filtered to fall within the same sensitivity range, in the lock-in amplifier, of the CRD signal. This reference signal is called the zero phase-shift and can automatically be programmed into the SRS 830 by hitting the reference button. Once the reference signal has been zeroed, the signal from the optical cavity is allowed to reach the PMT. In the oscilloscope this signal (if is delayed) may look like a shark fin instead of a square signal. This represents the delay, both loading and unloading the cavity, with respect to the reference signal. In the lock-in amplifier the phase shift can be read.

The lock-in uses low pass roll-off filters along with phase sensitive detectors to remove all of the unwanted AC signals and noise components from the signal. The roll-off filters are 6 dB/octave, RC type filters which output become steadier by using a long time constant. A single RC filter requires about 5 time constants to settle to its final value so that a 1 second time constant will need a wait of least 5 seconds. This parameter acts as a limiting factor when measuring very narrow rotational lines, therefore in chapter three we discuss its influence on the spectral resolution.

The phase measurements from the lock-in are sent via GPIB to a LabVIEW® data acquisition (DAQ) computer program. The program also controls the stepper motor that drives the micrometer screw on the dye laser, making scanning possible. After each step of the motor the DAQ acquires the phase in degrees from the lock-in and converts it to radians. The decay time constant τ is calculated as shown in equation 10. The absorption is then determined by:

$$\text{Absorption (cm}^{-1}\text{)} = \frac{1}{c\tau} \quad (27)$$

where c is the speed of light in cm/s. The DAQ program is shown in appendix E.

Experimental Procedure

Calibration

The micrometer screw on the dye laser must be calibrated periodically to obtain reliable PS-CRD results. The calibration is necessary whenever the adjustment knobs are used to re-align the laser after cleaning the optics. This is usually necessary when a decrease on the lasers performance is observed. Optics cleaning procedures can be found in Appendix C.

The calibration of the laser is necessary in order to convert the micrometer positions of the birefringent filter to wavenumbers (cm^{-1}). This is accomplished by using a monochromator and recording the resulting wavelength at every position of the micrometer screw. This is usually repeated for intervals of 5 – 10 micrometers until the desired range is covered. As Figure 15 shows, a plot of wavenumbers vs. micrometer positions is obtained and a polynomial fit can be used as the calibration equation. The latter can then be entered in the LabVIEW® software program so that the measured spectra are correctly positioned.

Off-Axis Alignment Procedure

The first step for the off-axis alignment is to perform the on-axis alignment. The detailed and improved procedure for the on-axis alignment can be found in Appendix B. Using the mirror periscope assembly placed in front of the cell (Figure 16), the incoming beam can be moved gradually off-axis from the center of the cavity. The laser beam can

be moved, to the left or right, up to 5 mm off the center axis. Selection of the direction of this displacement depends only on the quality of the initial alignment.

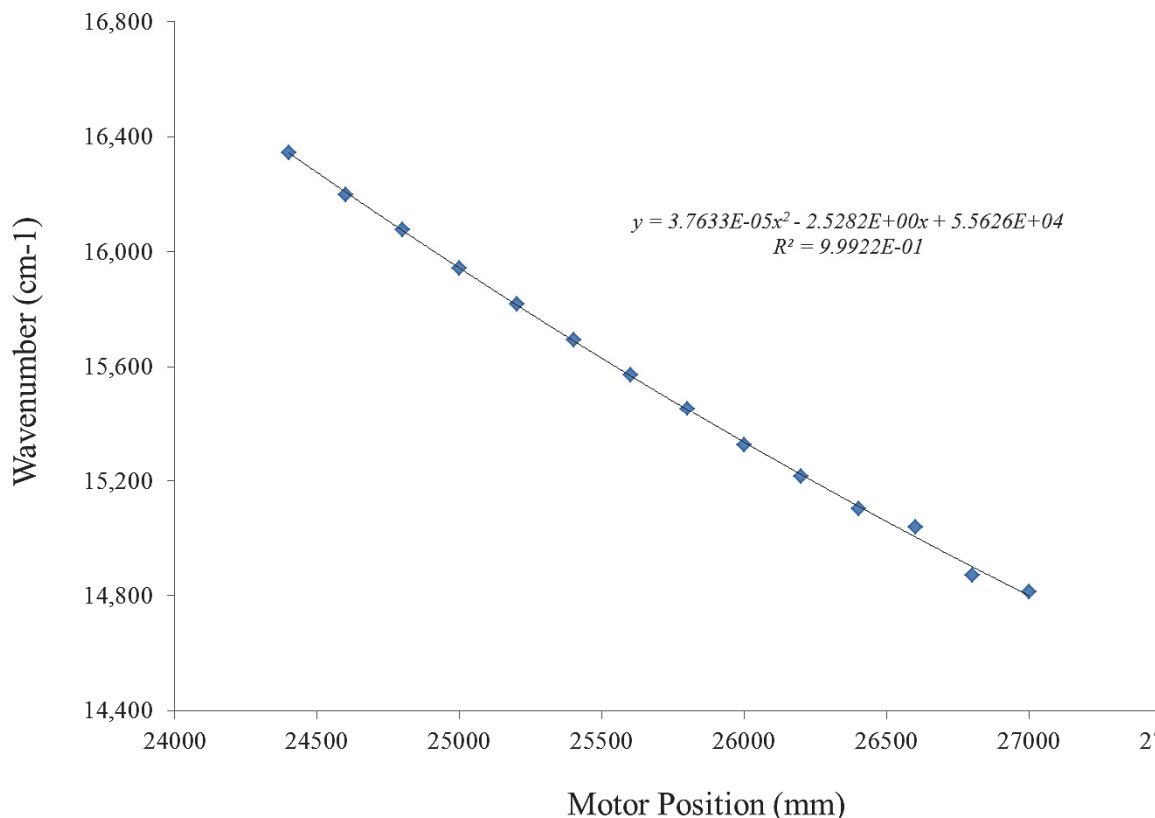


Figure 15. Calibration curve of the stepper motor

In the completed process the CRD signal needs to be monitored with the oscilloscope. The PS-CRD signal can be optimized with small adjustments of the alignment screws in the front mirror. After that, a lens is placed between the cell and the PMT to collect the output light from the cavity. Also, an iris is placed behind the lens to decrease the beam power and scattered light.

One more step is necessary when the PS-CRD system is aligned. After the maximum obtainable angle is found, the frequency of modulation must be adjusted up or

down to obtain a -45° angle. Some final adjustments may need to be made to tweak the signal, but these come from experience and practice.

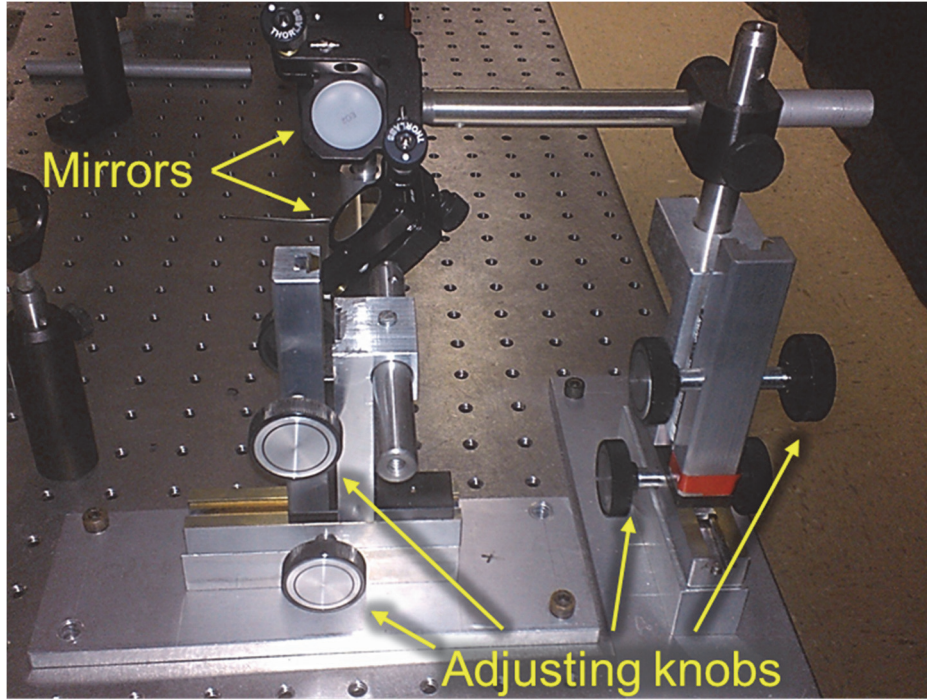


Figure 16. Mirror periscope located before the optical cavity

CHAPTER THREE

Evaluation of the PS-CRD Spectrometer for the Acquisition of High Resolution Spectra

The absorption spectra of molecular oxygen recorded for the ($2\leftarrow 0$) band of the $b^1\Sigma_g^+(v'' = 2) \leftarrow X^3\Sigma_g^-(v' = 0)$ transition using phase shift cavity ring down spectroscopy are presented in this chapter. Measurements at room temperature of the individual rotational line intensities were made for the oxygen γ -band at 628 nm. A comparison between experimental and simulated spectra validates the optimization procedure achieved experimentally. The spectra are used to evaluate experimental variables including gain, time constant, pause, sensitivity, and off-axis position.

Absorption Spectroscopy of the Oxygen Atmospheric Bands ($b^1\Sigma_g^+ \leftarrow X^3\Sigma_g^-$)

Transitions between the lowest three electronic states of the oxygen molecule, $X^3\Sigma_g^-$, $a^1\Delta_g$ and $b^1\Sigma_g^+$ give rise to several absorption band systems in the near infrared and visible regions. Figure 17 shows a potential energy diagram for the low-lying electronic states of O_2 .³⁸

The red atmospheric bands of molecular oxygen are due to the transition between the electronic triplet ground state $X^3\Sigma_g^-$ and the singlet electronic state $b^1\Sigma_g^+$. The ($0\leftarrow 0$), ($1\leftarrow 0$) and ($2\leftarrow 0$) bands are respectively denoted as the A , B , and γ bands. The ($0\leftarrow 0$) transition is favored by Frank-Condon factors over the ($1\leftarrow 0$) and ($2\leftarrow 0$) bands. Thus, the A -band is the strongest and the γ -band the weakest.

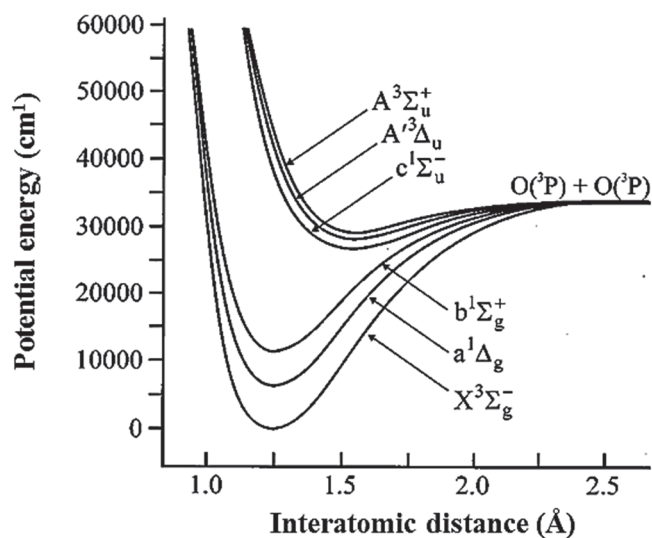


Figure 17. Potential energy diagram for the low-lying electronic states of O_2 .³⁸

These red atmospheric bands are very weak since the electronic dipole transition between the two states for the gerade - gerade, $\Sigma^+ \leftarrow \Sigma^-$, and singlet-triplet cases are all forbidden. Therefore, the transition takes place via a magnetic dipole interaction. Because the electronic ground state is the $X^3\Sigma_g^-$ state, the average electronic orbital angular momentum vanishes ($\Lambda = 0$). Nevertheless there is an instantaneous non-zero value of the orbital angular momentum which produces a recessing magnetic dipole moment of orbital origin. The total electronic spin is $S=1$ and hence, molecular oxygen has a permanent magnetic dipole moment of approximately two Bohr magnetons.

The first spectroscopic study of the red system of atmospheric oxygen bands was made by Babcock *et al*³⁹ using a long path cell in the laboratory and open path measurements through the atmosphere with two different grating spectrometers. Since then measurements of intensity have been made for individual rotational lines of the atmospheric oxygen $b^1\Sigma_g^+(v'' = 2) \leftarrow X^3\Sigma_g^-(v' = 0)$ A band and γ band by using

different techniques such intracavity laser-absorption spectroscopy (ICLAS)⁴⁰ and cavity ring down spectroscopy.^{31,32,41}

The high sensitivity of CRDS^{13,42}, phase shift cavity ring down spectroscopy²⁹ and Fourier transform phase shift cavity ring down spectroscopy⁴³ have been demonstrated by using several bands in the very weak forbidden $b^1\Sigma_g^+ \leftarrow X^3\Sigma_g^-$ transitions on gaseous molecular oxygen.

Structure of the Bands

The rotational levels of the O₂ states are designated by the quantum numbers J and K , where K represents the rotational angular momentum, and J , the total angular momentum, is the sum of the rotational and spin angular momenta, $J=K+S$. The ground state is split into levels corresponding to $J'' = K'', K''+1, K''-1$, with only odd values of K'' allowed (double primes and single primes denote lower and upper states, respectively). The upper electronic level, which has zero spin, is composed of single states with $J'=K'$, where only even values of K' are allowed.

The red atmospheric oxygen bands are comprised of four branches, two R -form branches forming a head and two P -form branches, separated from the former by a zero gap. The observed four branches of the red atmospheric oxygen bands can be accounted for only by the selection rules for magnetic dipole radiation,

$$\Delta J=0, \quad (J = 0 \overset{NO}{\leftrightarrow} J = 0) \quad (28)$$

$$\Delta J=\pm 1 \quad (+ \leftrightarrow +, - \leftrightarrow -, - \overset{NO}{\leftrightarrow} +) \quad (29)$$

The corresponding transitions are indicated in Figure 18 using full lines. There is an R R branch ($\Delta J = +1, \Delta K = +1$), a P P branch ($\Delta J = -1, \Delta K = -1$), an R Q branch ($\Delta J = 0,$

$\Delta K = +1$), and a PQ branch ($\Delta J = 0, \Delta K = -1$).³⁹ These are expressed according to the notation $\Delta^k\Delta J$.

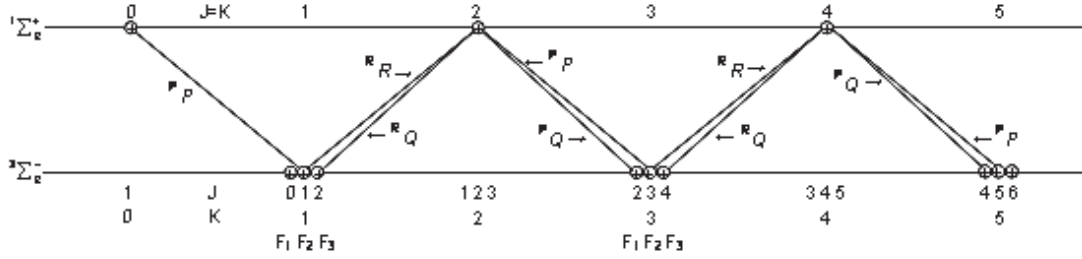


Figure 18. Combinations associated with branches of the red system of atmospheric oxygen

As shown in Figure 18, the three components of the $X^3\Sigma_g^-$ ground state of oxygen are designated by $F_1, F_2,$ and F_3 , in accordance with $J = K - 1, J = K,$ and $J = K + 1$. The PP and RR branches of the red atmospheric bands correspond to transitions from the F_2 component, the RQ and PQ branches to transitions from F_1 and F_3 components, respectively. These ${}^PP, {}^PQ, {}^RR,$ and RQ transitions can also be conveniently represented on a Fortrait diagram as the one shown at the top of Figure 19. The rotational terms F_i , are given by Watson.⁴⁴

For $J'' = K'' + 1,$

$$F_i = J''(J'' + 1)B'' + (2\lambda - \gamma) + (B'' - \lambda - 1/2\gamma) - \left[(B'' - \lambda - 1/2\gamma)^2 + 4J''(J'' + 1)(B'' - 1/2\gamma)^2 \right]^{1/2} \quad (30)$$

For $J'' = K'',$

$$F_i = J''(J'' + 1)B'' + (2\lambda - \gamma) \quad (31)$$

For $J'' = K'' - 1,$

$$F_i = J''(J'' + 1)B'' + (2\lambda - \gamma) + (B'' - \lambda - 1/2\gamma) + \left[(B'' - \lambda - 1/2\gamma)^2 + 4J''(J'' + 1)(B'' - 1/2\gamma)^2 \right]^{1/2} \quad (32)$$

where the inertial and coupling constants are $B'' = 1.43777 \text{ cm}^{-1}$, $\lambda = 1.984 \text{ cm}^{-1}$, and $\gamma = -0.084 \text{ cm}^{-1}$. The parameter λ indicates a coupling of the spin to the internuclear axis and thus indicates a deviation from Hund's case b which would normally be expected for an unperturbed $^3\Sigma$ state. The parameter γ represents the magnetic coupling between the electron spin and the axis of rotation.

Absorption Spectra for the (2,0) γ -Band of O_2 using CRD Spectroscopy

As mentioned in previous section, this γ band corresponds to the (2,0) band of the $b^1\Sigma_g^+ \leftarrow X^3\Sigma_g^-$ electronic system of the O_2 molecule, and it is the weakest absorption of the red atmospheric bands system, with a rather small Franck-Condon factor (0.00264).¹³ It is a highly forbidden transition, since it is gerade - gerade, $\Sigma^+ - \Sigma^-$ and a singlet-triplet transition.

Absorption spectra of oxygen γ bands were measured in the range (15795-15945) cm^{-1} using a dye laser with R6G as dye, pumped by a solid state Millennia V laser. Thus, PS-CRD was used to acquire the spectra. The resolution of the dye laser was 0.013 cm^{-1} . The path length achieved was 12.2 km. Figure 19 shows the simulated absorption spectrum of the oxygen γ band in the region between 15960 and 15750 cm^{-1} . The P P and P Q branches are very well resolved. Their assignments are indicated by the Fortrait diagram above. A congested region is also observed between 15930 to 15905 cm^{-1} where the R R and R Q branches of the γ band are seen. In this region the Δv between R R transitions start to decrease progressively, and these R R and R Q branches eventually start folding as the J values increase. Ultra-high resolution is required in order to fully resolve this area of the spectrum experimentally.

Figure 20 shows the absorption spectrum of the oxygen γ band in the region between 15960 and 15750 cm^{-1} . This is the spectrum obtained experimentally using the PS-CRD technique. Likewise, the $^{\text{P}}\text{P}$ and $^{\text{P}}\text{Q}$ branches are very well resolved. Nevertheless, due to inherent experimental limitations, the $^{\text{R}}\text{R}$ and $^{\text{R}}\text{Q}$ branches of the γ band are rather unresolved in the region between 15930 and 15905 cm^{-1} . Their assignments are indicated by the Fortrait diagram above. Still, some assignments could be made for some of the $^{\text{R}}\text{R}$ and $^{\text{R}}\text{Q}$ transitions, despite the insufficient resolution obtained in this region.

Perhaps these assignments can be observed better in Table 4. This table also shows a comparison between the values obtained by Babcock and Hertzberg³⁹ and those obtained in this work with PS-CRD and PGOPHER.

It can be seen in Figure 21 how the $^{\text{P}}\text{P}$ and $^{\text{P}}\text{Q}$ spectral values obtained with PS-CRD are closer to those obtained by Babcock et. al. whereas a larger gap exist between these and the simulation. This validates the experimental conditions, and calibration, achieved with the PS-CRD system described in Chapter Two.

Spectral Quality

A pressure series of 760, 300, 200, 100 and 50 Torr was measured and is displayed in Figure 22. This series of spectra show how the absorption increases along with the pressure of oxygen inside the cavity. This attest to the linear response expected from and absorption spectroscopy technique.

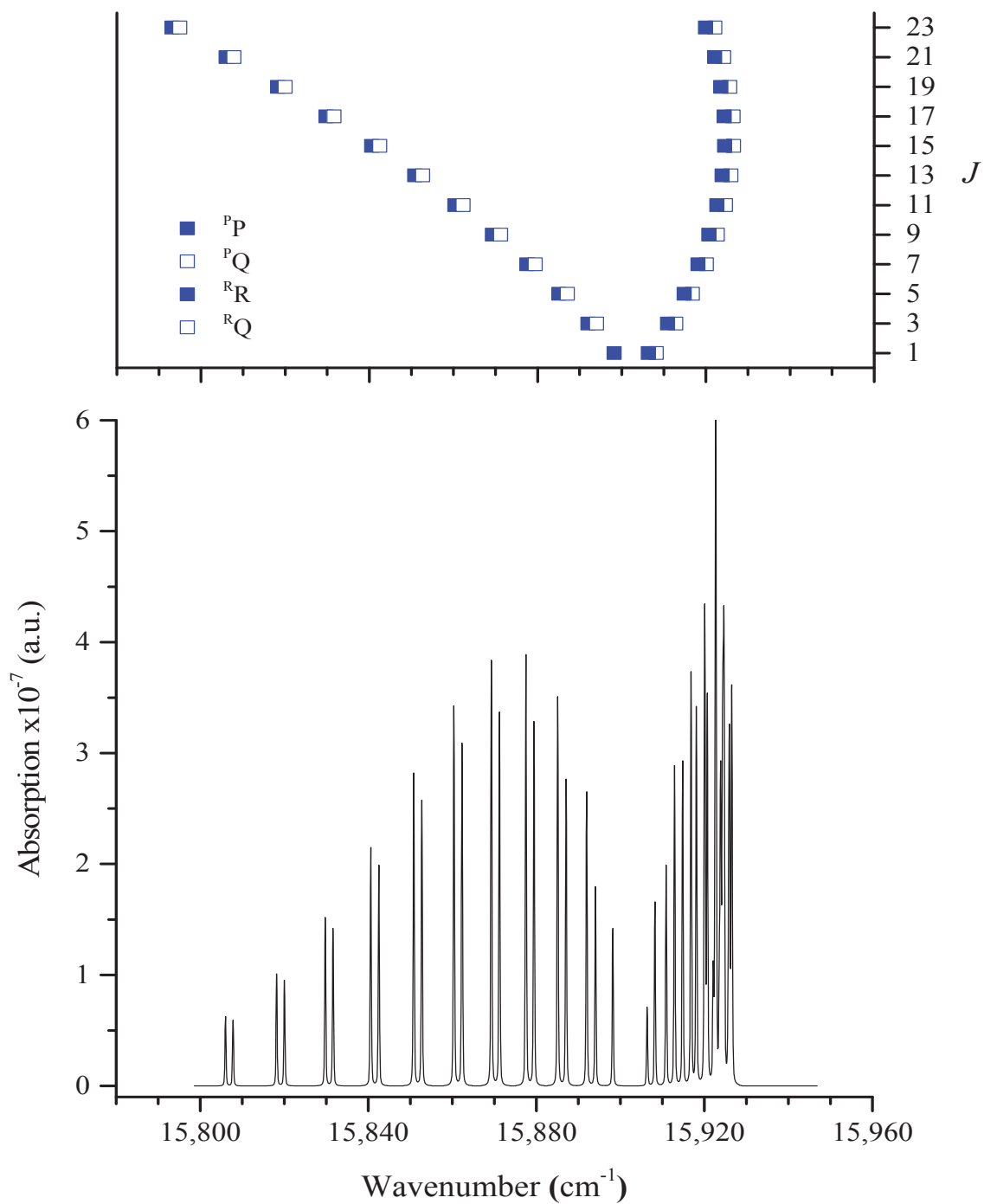


Figure 19. Bottom: Simulated rotational-vibrational spectrum of the γ band of O_2 obtained with the PGOPHER program.⁴⁵ Top: Corresponding Fortrait diagram. All rotational constants needed for this simulation were taken from reference 31.

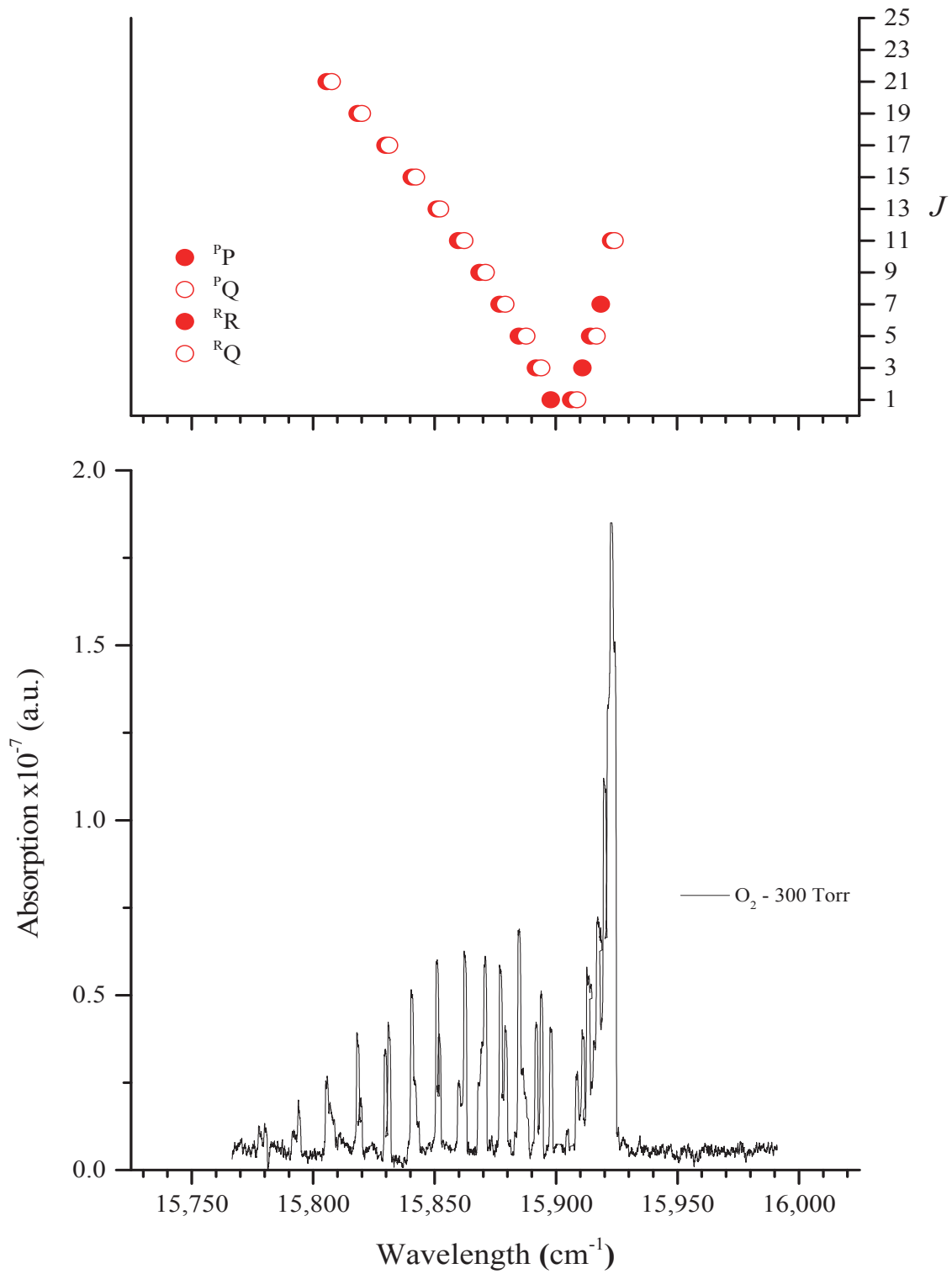


Figure 20. Bottom: Experimental result for the rotational-vibrational spectrum of the γ band of O_2 acquired with PS-CRD. Top: Corresponding Fortrait diagram.

Table 4. Line absorption frequencies

J	Babcock & Hertzberg		PGOPHER Simulation		This Work	
	^P P Branch	^P Q Branch	^P P Branch	^P Q Branch	^P P Branch	^P Q Branch
1	15,899.546	-----	15,898.2	-----	15,897.9	-----
3	93.294	15,895.379	91.9	15,894.1	91.9	94.0
5	86.381	88.394	85.1	87.1	84.8	87.8
7	78.806	80.780	77.6	79.5	76.9	79.2
9	70.576	72.515	69.3	71.3	68.6	71.1
11	61.668	63.591	60.5	62.4	59.8	62.3
13	52.104	54.006	50.8	52.8	51.0	52.3
15	41.883	43.766	40.7	42.6	40.7	42.4
17	30.993	32.854	29.7	31.7	29.9	31.3
19	19.434	21.282	18.2	20.1	18.4	20.1
21	07.208	09.030	06.0	08.0	05.7	07.7

J	^R R Branch	^R Q Branch	^R R Branch	^R Q Branch	^R R Branch	^R Q Branch
1	15,907.674	15,909.550	15,906.4	15,908.2	15,906.4	15,908.8
3	12.257	14.207	10.8	13.0	11.0	-----
5	16.718	18.168	14.8	16.9	14.2	16.8
7	19.472	21.443	18.2	19.9	18.5	-----
9	22.008	24.049	20.7	22.2	-----	-----
11	23.916	25.982	22.4	24.5	22.9	24.2
13	25.153	27.234	23.6	25.8	-----	-----
15	25.709	27.813	24.3	26.3	-----	-----
17	25.580	27.704	24.1	26.3	-----	-----
19	24.781	26.930	23.4	25.6	-----	-----
21	23.286	25.440	21.8	24.1	-----	-----

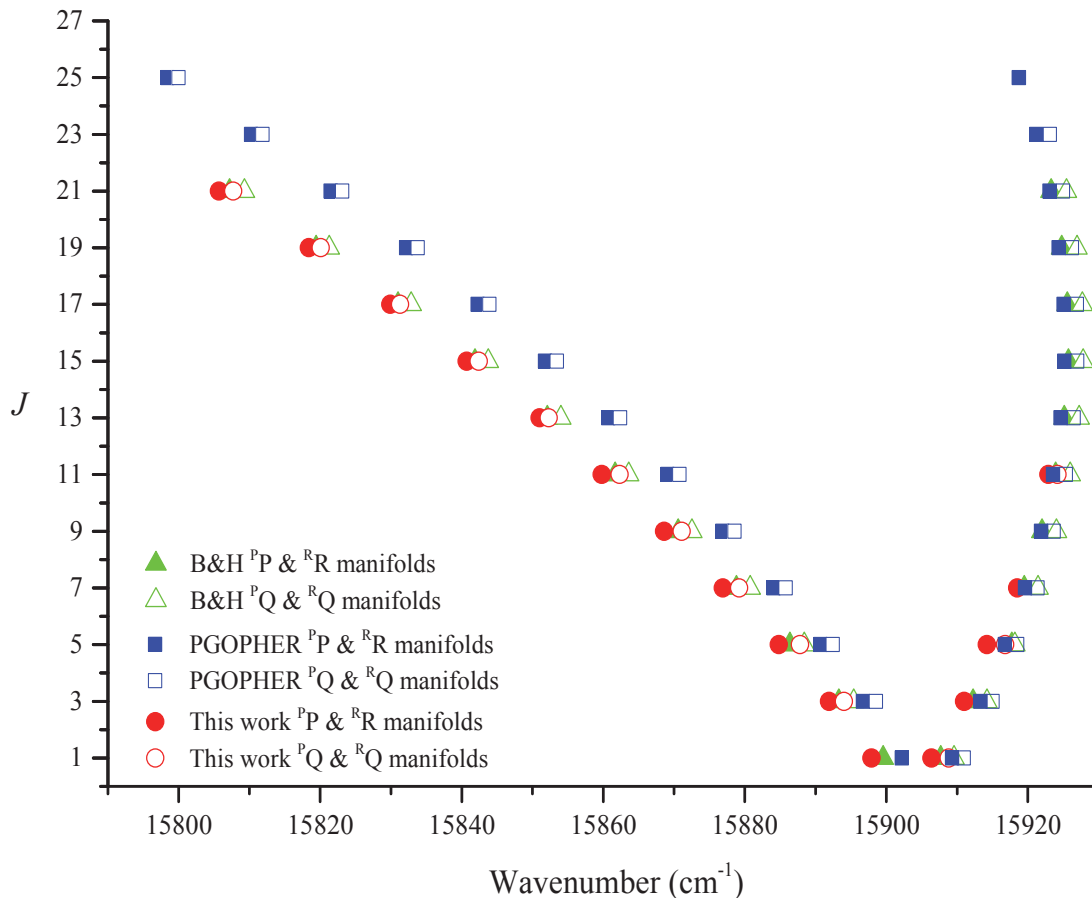


Figure 21. Fortrait diagrams comparison the between the work of Babcock and Hertzberg (\blacktriangle), PGOPHER Simulation (\blacksquare), and this work (\bullet). Filled items represent the $^P P$ and $^R R$ branches while empty items represent the $^P Q$ and $^R Q$ branches.

Quantitative measurements of spectral parameters like signal to noise ratio (S/N) and root mean square (RMS) noise can be measured for individual spectra, in order to evaluate the impact of the experimental variables inherent to the PS-CRD technique on the overall quality of a spectrum.

The complexity of a PS-CRD spectrometer, which uses several instruments including pre-amplifiers, lock-in amplifiers, PMT detectors, etc., requires optimizing many variables in order to obtain good quality spectra. Although the impact of some of these variables on the overall spectral quality might be obvious, some others are not.

Some of these are the pre-amplifier's gain, the sensitivity of the lock-in amplifier, the time constant set on the lock-in amplifier for the averaging of the signal, and the pause taken by the data acquisition software between iterations. Because the PS-CRD technique does not depend on the intensity of the radiation but rather on the time the radiation spends inside the cavity, the use of variables like gain, sensitivity, and laser power must be weighted out as their influence on the overall signal is not very straight forward.

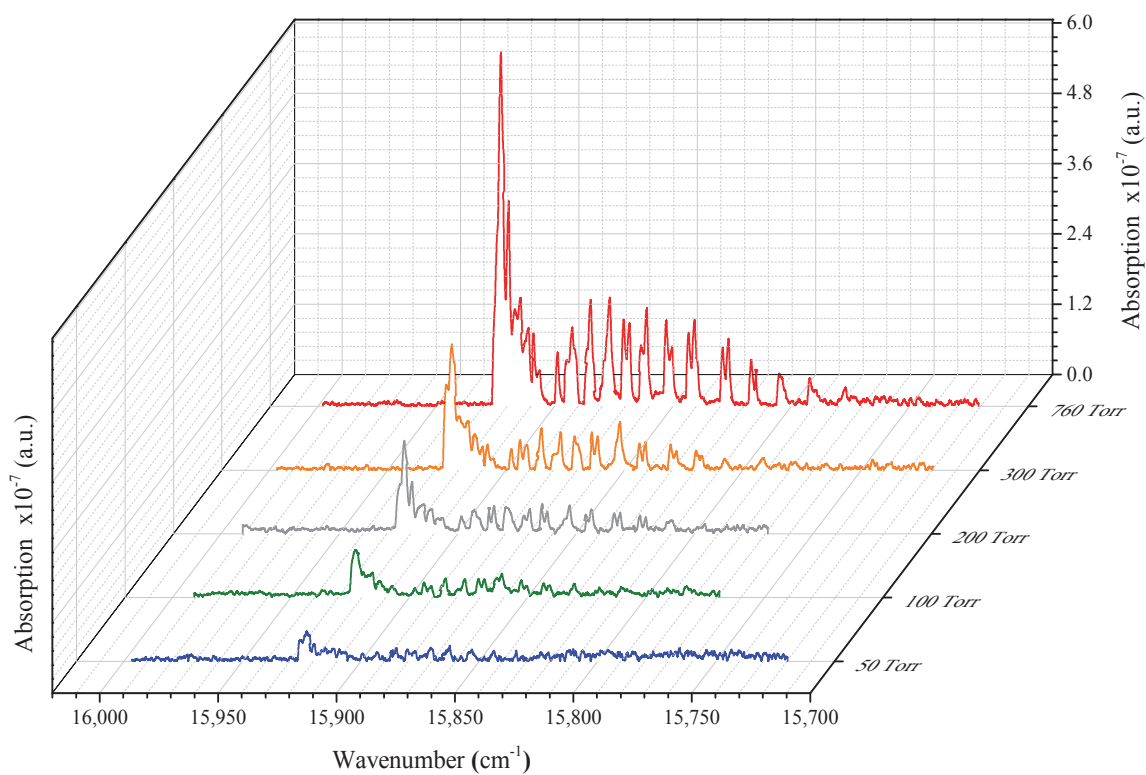


Figure 22. Oxygen γ band. Absorption pressure series at 295K

Signal to Noise Ratio

This quantity was used as the primary indicator of the spectral quality of each spectrum. The signal intensity was obtained from the spectral data by looking at the $^{\text{R}}\text{R11}$ transition line ($15,922.9 \text{ cm}^{-1}$) of the full spectra, as well as the $^{\text{P}}\text{P5}$ line ($15,884.8 \text{ cm}^{-1}$)

for the spectra where only the P branch is shown. The root mean square (RMS) noise was calculated using equation 33. Equation 34 shows the resulting expression for the S/N.

$$N_{RMS} = \sqrt{\frac{\sum_{i=1}^n (S_x - S_i)^2}{n}} \quad (33)$$

$$S/N_{RMS} = \frac{I_{R_{R11}}}{\sqrt{\frac{\sum_{i=1}^n (S_x - S_i)^2}{n}}} \quad (34)$$

where n is the number of data points used in the calculation, I_{RR11} can be substituted by I_{PP5} and represents the intensity of the $^R R_{11}$ and $^P P_5$ lines, respectively, S_x is the average line intensity, and S_i is the line intensity of at a particular data point. On average among all the analyzed spectra, the value of n was 4596 or higher.

Tables 5 and 6 show the S/N ratios calculated for the pressure series shown in Figure 22. These were calculated using the intensities of both transitions, $^R R_{11}$ and $^P P_5$, respectively. They show that all runs were obtained with similar noise values despite the increases in pressure. Accordingly, the intensities of the I_{RR11} and I_{PP5} lines increased with the pressure. The table also shows the number of resolved bands obtained on each of the spectra. The criteria used for counting the resolved peaks was only limited to the P branch of the spectra since neither of the R branch peaks were resolved satisfactorily. This is due in part to the folding nature of the R branch manifold, which complicates this region of the spectrum. On the other hand, the gap between adjacent transition lines tends to increase for the P branch, facilitating the identification of resolved peaks. Calculations of the frequency width at half maximum (FWHM) could be made for each peak but, given the number of peaks, we considered it convenient not to do so in order to facilitate

the description of the analysis presented in this work. Although the best S/N ratios were obtained at the highest pressure of this series, it can be concluded from these results that the best spectrum was obtained at 300 Torr. Therefore all succeeding runs were evaluated at this pressure.

Table 5. S/N results with the ^RR11 line values

P (Torr)	RMS Noise	I ^R _{R11}	S/N Ratio	# Resolved Bands*
50	2.3E-09	2.2E-08	9.3	1
100	2.2E-09	8.1E-08	37.1	5
200	2.3E-09	1.6E-07	70.0	7
300	2.0E-09	2.1E-07	108.5	7
760	2.0E-09	6.1E-07	295.3	1

* out of 23 possible (P branch)

Table 6. S/N results with the ^PP5 line values

P (Torr)	RMS Noise	I ^P _{P5}	S/N Ratio	# Resolved Bands*
50	2.3E-09	2.3E-08	9.8	1
100	2.2E-09	3.3E-08	15.1	5
200	2.3E-09	4.7E-08	20.7	7
300	2.0E-09	7.1E-08	36.0	7
760	2.0E-09	1.8E-07	88.8	1

* out of 23 possible (P branch)

Acquisition Pause

Appendix E shows the LabVIEW code used to control, operate, and acquire data with the PS-CRD spectrometer explained previously and shown in Figure 14. This customized program can execute several duties, from moving the stepper motor attached the dye laser, to acquiring the data readings from the lock-in amplifier, solving simple algorithms, plotting the results in real time, and properly saving the data into common electronic files. It performs the entire cycle in a timely manner and in as many iterations

as required, depending on the desired range of wavelengths. Typically the number of iterations is determined by the number of steps taken by the stepper motor plus one more.

At the end of each cycle the program must take a “Pause” before starting the next iteration. The length of this pause, measured in seconds, must be designated by the operator, and it depends on the configuration of the lock-in amplifier during a scan. Parameters like time constant, dynamic range, and number of data points to be averaged are important factor to be considered when determining the length of the pause. The challenge is to find a pause value long enough to allow the system to acquire good quality spectra, yet short enough to avoid scans taking long periods of acquisition time. Therefore, the balance between a good quality, high resolution spectrum and short scan duration must be achieved.

Several pause values were tested, from 0 s, 100 ms, 200 ms, and 300 ms, and we found an increase in the spectral quality until it no longer improves after 300 ms. The spectral quality was evaluated using both ^RR11 and ^PP5 transition lines of the oxygen’s γ -band. Figure 23 and Tables 7 and 8 show the results for 0 and 300 ms.

Table 7. S/N results at different pause length using the ^RR11 line values

P (Torr)	Pause (ms)	RMS Noise	I ^R R11	S/N Ratio	# Resolved Bands*
300	300.0	1.3E-09	1.9E-07	144.9	10
300	0.0	9.4E-10	1.5E-07	163.9	1

* out of 23 possible (P branch)

Table 8. S/N results at different pause length using the ^PP5 line values

P (Torr)	Pause (ms)	RMS Noise	I ^P P5	S/N Ratio	# Resolved Bands*
300	300.0	1.3E-09	6.9E-08	53.9	10
300	0.0	9.4E-10	3.2E-08	34.0	1

* out of 23 possible (P branch)

Figure 23 shows how the resolution of the spectrum gets diminished when the software performs without taking any pause. This means that it is not allowing enough time to let the signal stabilize before it acquires it from the lock-in amplifier, and it basically reads the first number that the latter registers. The shape of the band and the intensity of each transition are also affected as it can be seen on Figure 23. The shape of the P-branch of the 0 ms spectrum is affected by the randomness of the quick reading which affects the S/N values.

Pre-Amplification

As shown in Figure 14, the signal coming out of the PMT detector must pass through a pre-amplifier before it reaches the lock-in amplifier. In conventional absorption spectroscopy methods the sensitivity of the technique and the S/N ratio depend upon the strength of the signal. In these cases, an amplification of the detector's electronic response will increase the intensity of the signal and also the noise. As explained in the previous chapter, CRD does not depend on the intensity of the signal nor the laser power, but rather on the time it takes the incident beam to exit the cavity. Nevertheless, after the beam has undergone several round trips inside the cavity, and consequently absorbed by the sample, the exiting beam is not intense enough to be read accurately by the lock-in amplifier. Even with the amplification range obtained with the PMT, the magnitude of the signal is low and therefore the use of a pre-amplifier is critical.

Several scans were obtained at different levels of gain of the pre-amplifier and the quality of the resulting spectra was evaluated looking at the P branch of the γ band of O₂. Table 9 shows the results obtained at three different values of gain and these spectra are shown in Figure 24.

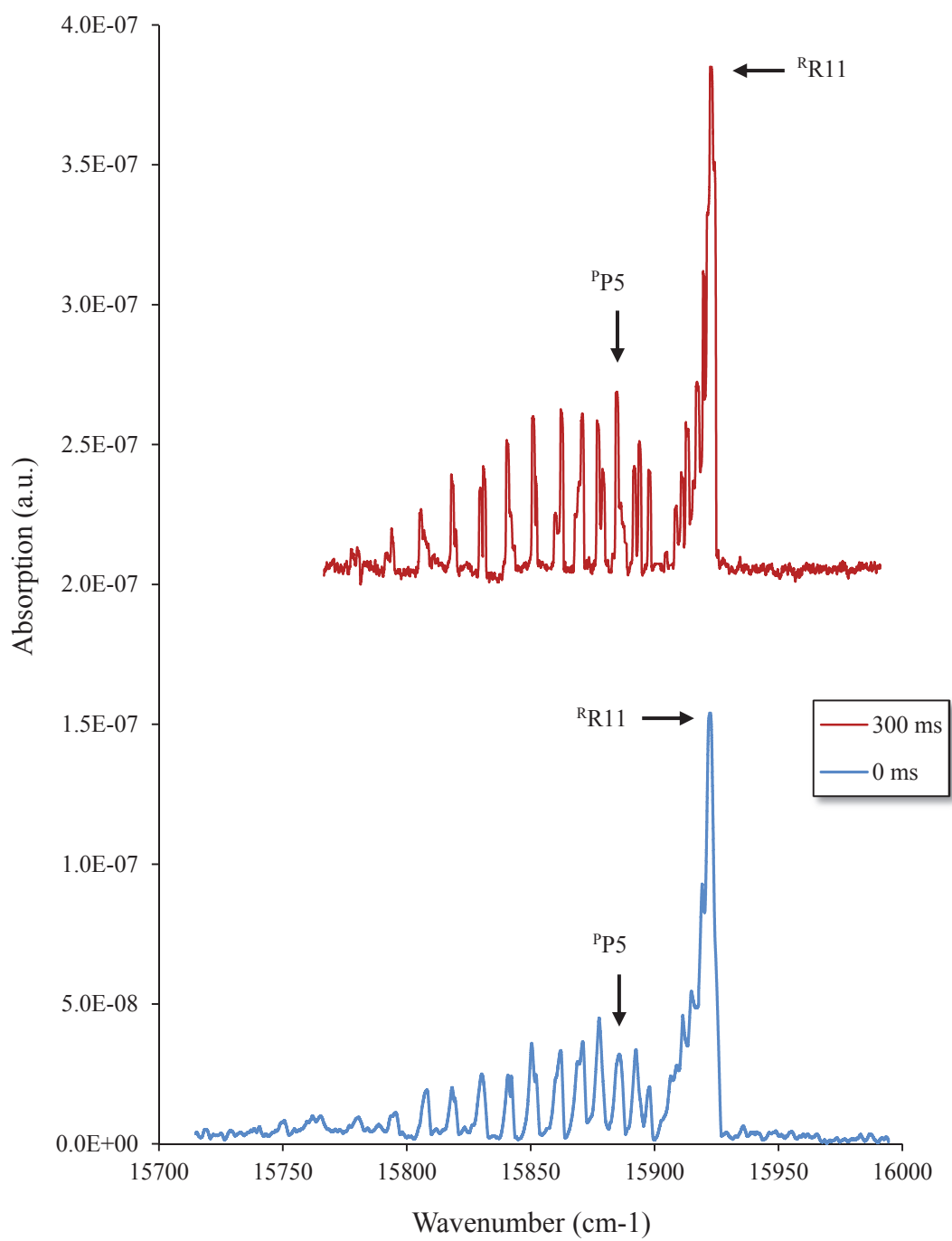


Figure 23. Oxygen γ band obtained at different acquisition pause. (Top) 300.0 ms, (Bottom) 0.0 ms.

Table 9. S/N results at different gain values

P (Torr)	Gain	RMS Noise	$I^{P_{P5}}$	S/N Ratio	# Resolved Bands*
300	100	9.9E-10	5.4E-08	54.5	11
300	50	9.4E-10	5.6E-08	59.3	11
300	20	9.9E-10	5.5E-08	55.5	11

* out of 23 possible (P branch)

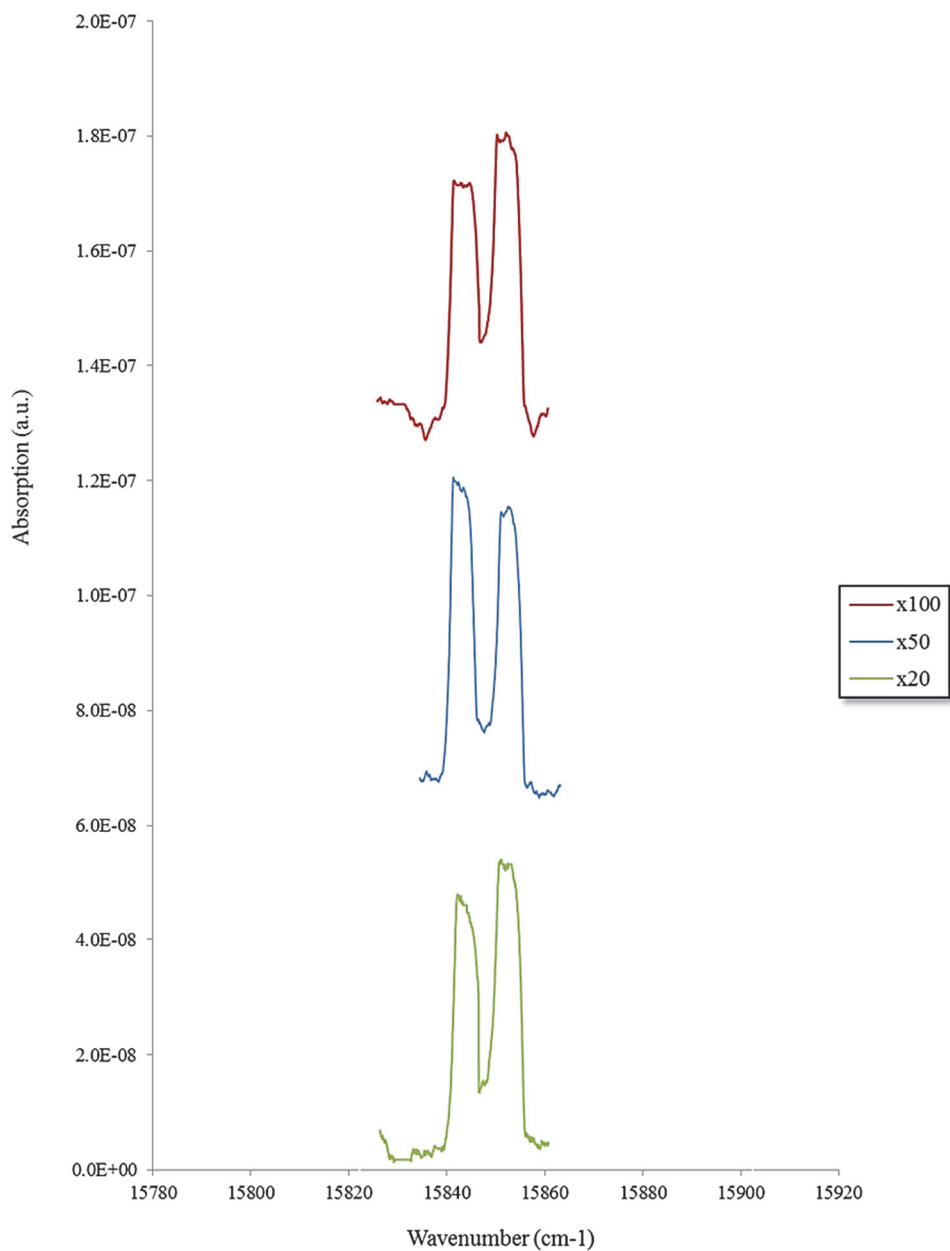


Figure 24. PQ5 and PP5 lines of the P-branch of the oxygen γ band evaluated at different pre-amplification gain. (Top) x100 times, (Middle) x50 times, (Bottom) x20 times.

Contrary to what was expected the noise remains approximately the same for all the gain values. Similarly, the intensity of the ^PP5 line maintained its value and no other resolved bands were noticed. In general, judging only by the empirical results shown in table 9, the spectral quality of these results remained independent of the gain value. Nevertheless, it can be noticed that the baseline of the spectrum is slightly affected at the highest gain value of x100. The slight frequency shift between the maximums of each of the bands and their homologues is not a consequence of the gain and it should not be understood as such. This shift is due to the small inaccuracy in the calibration of the stepper motor shown in Figure 15.

Sensitivity

Once the pre-amplified signal is received by the lock-in amplifier, the need for adjusting the sensitivity of this apparatus arises. Generally, there will be a range of suitable sensitivity values going from the point of maximum sensitivity, where the lock-in is near saturation, to the lowest sensitivity in which the lock-in amplifier hardly registers any signal. Usually, when the lock-in amplifier is at its most sensitive level, its dynamic range is at its highest, which introduces a large degree of volatility on the measurements. Although this volatility of the signal can be controlled by changing some of the lock-in amplifier's parameters, like time constant or signal averaging, sometimes these actions are not desired.

Another factor that influences the selection of the sensitivity levels of the lock-in amplifier is inherent in the nature of the PS-CRD experiment itself. When the beam of light is by passed around the cavity to be taken as a reference, it is only experiencing a one way trip along the cavity and therefore its intensity is much larger than that of the

beam traveling across the cavity. Therefore, the signal of the reference beam that gets sent to the lock-in amplifier is much higher than the one belonging to the cavity beam.

Some efforts can be made to minimize this situation by locating optical density filters along the reference beam, but the intensity of the beam exiting the cavity is so low that the reference beam will still be much more intense. Occasionally, this will lead to choosing a different sensitivity level for each of the two signals, which at first sight does not seem ideal.

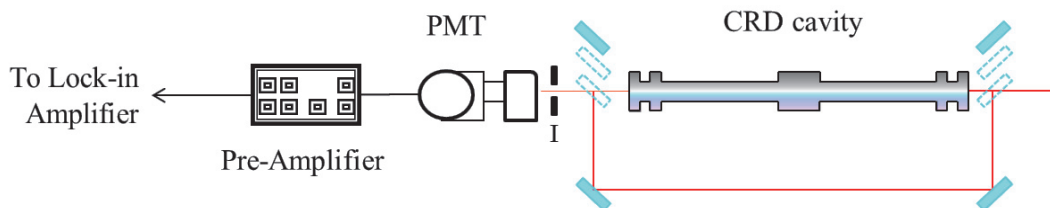


Figure 25. Section of the experimental setup of the PS-CRD spectrometer. Intensity of the reference beam versus intensity of the cavity beam. Key: I, iris; PMT, photomultiplier tube.

Several spectra were obtained at different levels of sensitivity of the lock-in amplifier, and their spectral quality was evaluated looking at the P branch of the γ band of O_2 . Table 10 shows the results obtained at two values of sensitivity representing the outermost values of the studied range. Even though at 50 mV the lock-in amplifier is a hundred times less sensitive than at 0.5 mV, the latter produced results with slightly lower spectral quality than those obtained at 50 mV. These spectra are shown in Figure 26.

Table 10. S/N results at different sensitivities

P (Torr)	Sensitivity (mV)	RMS Noise	$I^{P_{P5}}$	S/N Ratio	# Resolved Bands*
300	50	9.9E-10	5.5E-08	55.5	13
300	0.5	1.1E-09	4.4E-08	42.1	8

* out of 23 possible (P branch)

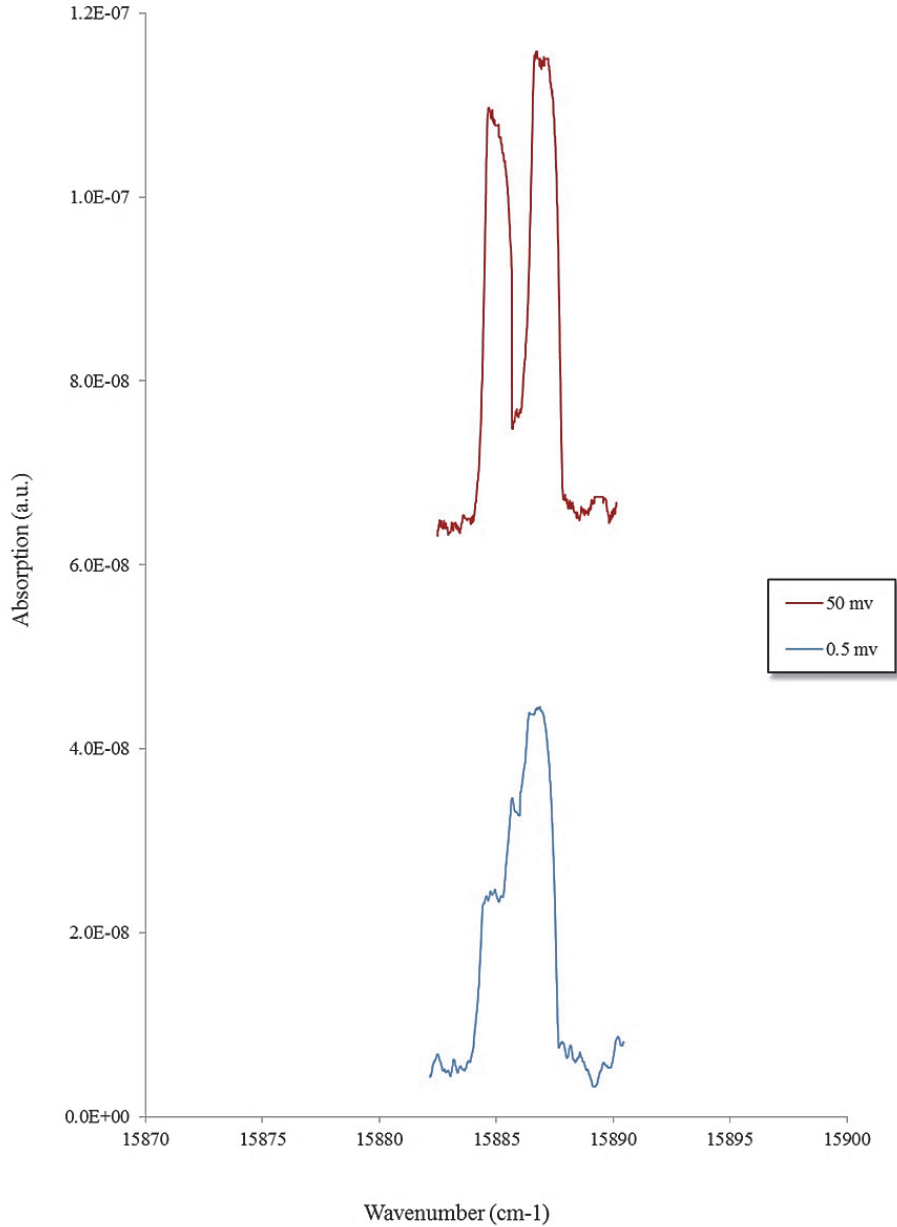


Figure 26. PQ_5 and PP_5 lines of the P-branch of the oxygen γ band evaluated at different sensitivity values. (Top) 50 mV, (Bottom) 0.5 mV.

Off-Axis vs On-Axis Alignment

In Chapter Two of this work the off-axis method was described as an alternative to improve the results obtained with a PS-CRD spectrometer. Its major advantages are the increased coupling of the laser beam into the cavity, and the decrease of the free spectral range (FSR) when the beam is still in it. Experimentally, the off-axis alignment is risky and hard to achieve because, if it is not performed in a rather methodic way, there is a high probability that the return to the exact same initial on-axis position will never be achieved. This is due to the imperfect nature of all the optics involved in this already complicated CRD setup. Under these conditions it is often questionable whether it is worth taking such risk, especially considering that not all off-axis positions of the beam will lead to the best result or to a better result than that already obtained via the on-axis alignment. Furthermore, the optimal off-axis position could be at any distance from the center axis and at any of the 360° of the plane delimited by the entry mirror.

Several spectra of the γ -band of oxygen were recorded at different positions to the left and to the right of the on-axis position, and the spectral quality was evaluated on each case. Because of experimental challenges, the off-axis positions to the north, south, and any diagonal directions were not evaluated. It was found that there was no symmetry between the results to the left and those to the right of the center axis. We evaluated off-axis positions located at 0.8 mm, 1.6 mm, 2.4 mm, and 3.2 mm on both sides, and in neither of these cases did the results at one of these positions matched those obtained at the identical distance on the opposite side.

Table 11 shows the results obtained for the positions located to the right side of the center axis. These results were obtained running the system with the best

configuration of all the experimental parameters discussed thus far. A comparison with the on-axis position of the beam is also shown. The selection of these discrete positions was ruled by the spot size of the incoming beam (1.6 mm), and the experimental limitations inherent to our system.

Table 11. S/N results at different Off-Axis positions

P (Torr)	Off- Axis (in)	Off- Axis (mm)	RMS Noise	I_{P5}	S/N Ratio	# Resolved Bands*
300	0.125	3.2	2.5E-09	5.0E-08	19.7	7
300	0.094	2.4	2.1E-09	9.8E-08	46.2	10
300	0.063	1.6	8.7E-09	8.5E-08	9.7	5
300	0.031	0.8	3.8E-09	8.4E-08	22.3	6
300	0.000	0.0	1.5E-09	4.5E-08	29.0	7

* out of 23 possible (P branch)

Conclusions

Table 4 and Figure 21 show that the spectra obtained in this work with our PS-CRD setup correlate closely to the simulated spectrum and, more importantly, to those values obtained by Babcock and Hertzberg on their work. This should validate the experimental setup used in this work. The linear response of our system was also demonstrated with the pressure series experiment shown in Figure 22. A simple analysis of the spectral quality of this series showed that the response of the system at pressures of 50 Torr is governed by a large amount of noise on the signal. On the other end of the range, results suggest that at high pressures the systems starts experiencing saturation effects at 760 Torr. The optimal values of S/N ratio and resolved bands count were found at 300 Torr of oxygen, and therefore that same pressure was used for the forthcoming analysis of the experimental variables.

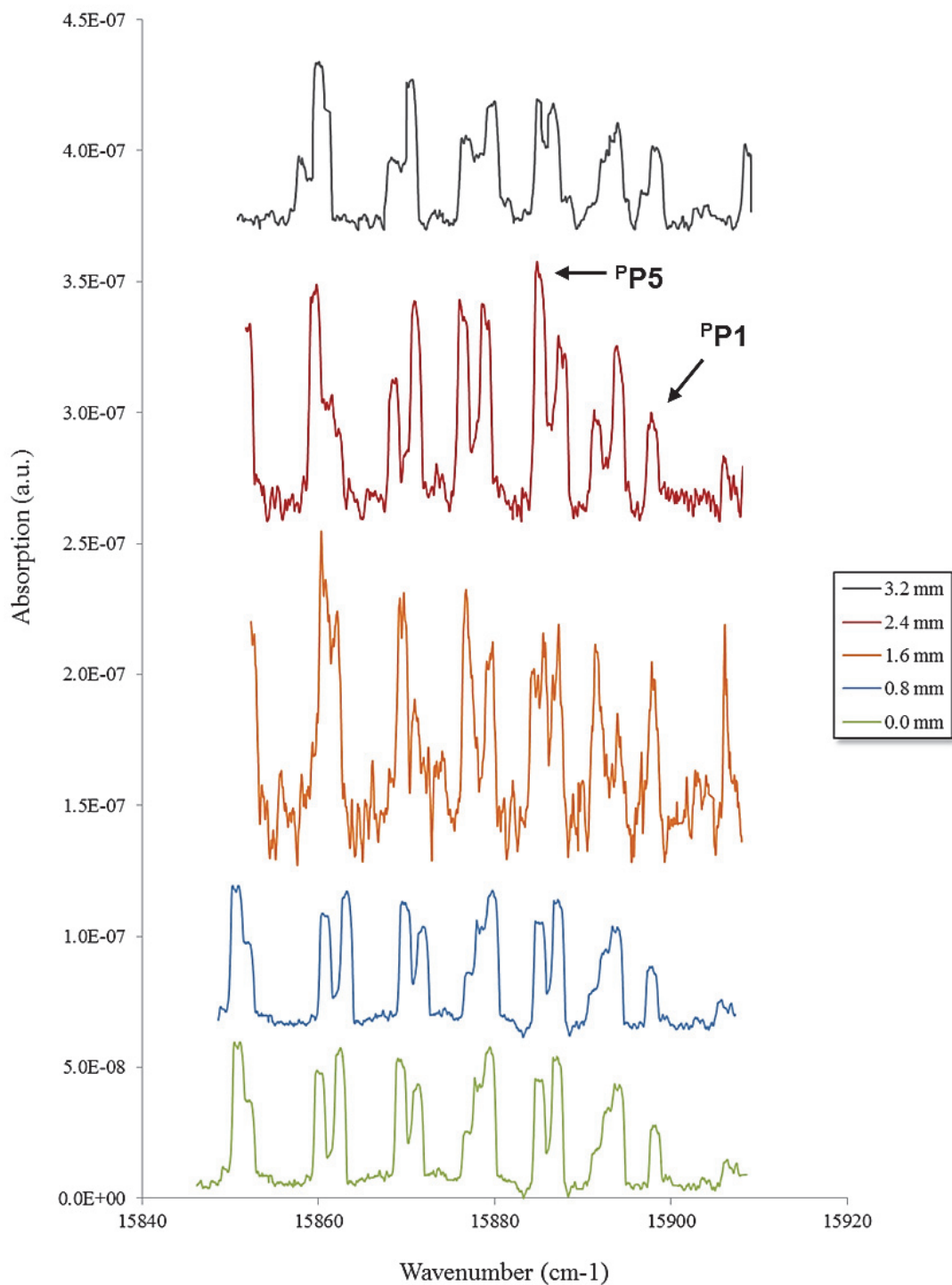


Figure 27. Portion of the P-branch of the oxygen γ band, from $^{\text{P}}\text{P13}$ to $^{\text{P}}\text{P1}$, obtained at different Off-Axis positions. (Lowest) 0.0 mm, (Uppermost) 3.2 mm.

Despite the complicated nature of the PS-CRD experiment, some of the most common experimental variables were evaluated, and the results show that the spectral quality is not greatly affected by changes in the gain of the pre-amplifier. Table 9 does not show major differences on the S/N values nor a change in the resolved bands count for any of the three evaluated gain values. On the other hand, the acquisition pause can be very influential on the overall spectral quality within a small range of values. For values higher than 300 ms no major changes were found experimentally, and the more contrasting difference was found between 0 and 300 ms as shown in Figure 23. All these were tested with the lock-in amplifier set with the same time constant of 3 s during all the scans.

The sensitivity of the lock-in amplifier has a small effect on the overall quality of the spectra. The results were better when setting up the lock-in amplifier at relatively low sensitivity, which may sound contradictory. Nevertheless, this re-enforces what we know about CRD and its non-dependence on the strength of the signal. Our results suggest this signal only needs to be strong enough for the lock-in amplifier to lock the corresponding phase and to determine the phase shifts with respect to the reference signal.

Lastly, the off-axis/on-axis comparison shows some interesting findings. After the main on-axis alignment has unequivocally been accomplished, one may be tempted to conclude that any off-axis position parallel to the preceding on-axis position would improve the method. The results show otherwise. Optimal off-axis positions seem to be found at very discrete angles from the center axis. In every case the intensity of the CRD signal increased, but in some cases this occurred to the detriment of the band resolution and the S/N ratio. A result more difficult to demonstrate with scientific data is the

increase in the continuous coupling of the beam inside the cavity. It has been reported elsewhere^{33, 34} that this factor results in an “optical sensor that is more robust and insensitive to mechanical vibrations”. Experimentally, this increase in the coupling of the incoming beam translated into a major improvement of the stability of the experimental setup. When working with on-axis CRD, it is normal to notice a frequent decline on the experimental configuration of the PS-CRD sensor. This is usually caused by random events like mechanical vibrations, small changes in the alignment of the dye laser cavity, small displacements of the optics holders and mirrors, etc. All this makes critical the adjustment of the cavity alignment every 24 hours. Nevertheless, when the sensor was setup for the off-axis configuration, the system did become rather robust. Declines on the quality of the alignment were not noticed for weeks, which translated into the acquisition of large amounts of spectra under virtually the same experimental conditions.

CHAPTER FOUR

Thermal Lens Spectroscopy

This chapter presents the fundamentals of the Thermal Lens (TL) technique. A description of the instrumental setup follows, starting with a complete presentation of the Thermal Lens (TL) system, from the cell design to the TL experimental setup, including cryostat design and preparation of cryogenic samples. The application of the TL technique for the study of the hydrocarbon lakes found in the moon Titan is discussed. An improved experimental setup for the study of cryogenic multicomponent solutions is presented. This is done through acquisition of the thermal lens spectra of the C - H ($\Delta v = 0 \rightarrow 4$) vibrational transition of ethane at 91 K, and C - H ($\Delta v = 0 \rightarrow 5$) vibrational transition of benzene at room Temperature. Finally, a TL spectrum of a binary cryogenic solution of ethylene in ethane is also shown.

Thermal Lens Spectroscopy (TLS) was first discovered by Gordon et al.⁴⁶ who also suggested its use for the detection of very weak absorptions.^{3, 47} TLS was also the first photothermal spectroscopic method applied for sensitive chemical analysis, and it is a powerful technique in the analysis of chemical traces.^{48, 49} TLS can be used in the thermal characterization of materials,⁵⁰ as well as being a useful tool in areas of fundamental studies, including the measurement of absolute fluorescence quantum yields,⁵¹ measurement of thermal diffusivities,⁵² and the measurement of two-photon absorption spectra.⁵³ Table 12 summarizes some of the most common photothermal techniques and their applicability.⁵⁴

Table 12. Common detection used in photothermal spectroscopy

Thermodynamic Parameter	Measured Property	Detection Technique
Temperature	Temperature	Calorimetry
	Infrared emission	Infrared emission
		Photothermal radiometry
Pressure	Acoustic wave	Photoacoustic spectroscopy
Density	Refractive index	Photothermal lens
		Photothermal interferometry
		Photothermal deflection
		Photothermal refraction
		Photothermal diffraction
	Surface deformation	Surface deflection

Thermal Lens Spectroscopy (TLS) is based on the Photothermal Lens Effect. When a molecule absorbs radiation, the excited specie releases energy to return to the ground state. Heat is then produced in a non-radiative decay. This causes a temperature increase of the molecules which decreases the refractive index, n , of that medium. As a result of this, a radial n gradient is formed at the focal plane of the radiation, as shown on Figure 28. The lens is created through the temperature dependence of the sample's refractive index.

The lens usually has a negative focal length since most materials expand upon heating and the refractive index is proportional to the density. If the excitation light has a non- uniform shape (e.g., Gaussian shape), a localized non-uniform distribution of the refractive index is formed, acting like a concave, or negative, lens. This negative lens causes the divergence of a second beam (probe beam) traversing the sample and the signal is detected as a time dependent power decrease of the probe beam. Spectroscopy can be readily achieved by scanning the wavelength of the excitation source. The lens created in the medium is called the thermal lens (TL).⁵⁵

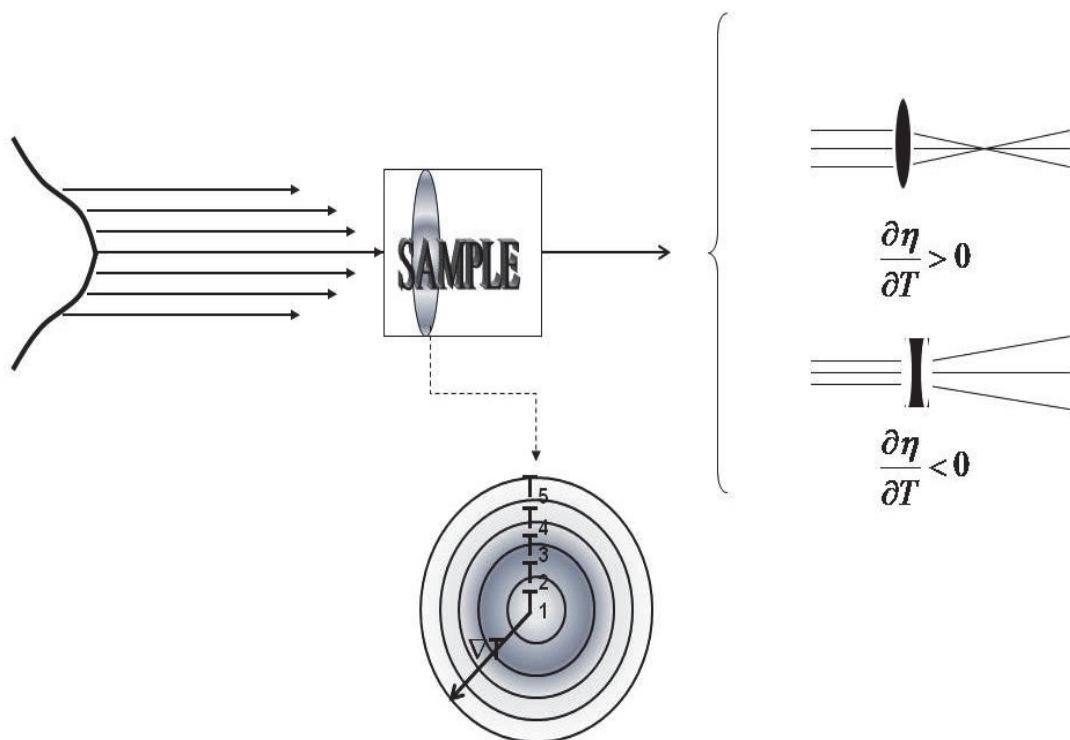


Figure 28. A probe beam irradiates an excited sample. Depending upon the change in the refractive index, η , and the density of the sample, a convergent or divergent lens will change the direction of the probe radiation. For most liquids, $\partial\eta/\partial T < 0$, which results in a divergent lens.

The original TL apparatus used by Gordon et. al.³ was studied and improved by Grabiner, et al,⁵⁶ to measure vibrational relaxation rate constants. This was further developed by Hu and Whinnery achieving more sensitive absorbance measurements⁵⁷. These studies resulted in less complicated transient signals, as well as simplified the theory behind these.

The typical components of the TL apparatus are: (i) the coherent laser excitation source able to deliver high optical power throughout a small cross section area of the sample, (ii) a low absorbance sample, (iii) an optical filter or pinhole (or both) placed in the far field, and (iv) a photodetector to measure the power beyond the pinhole. A simplistic view of the optical system for the thermal lens apparatus is shown in Figure 29.

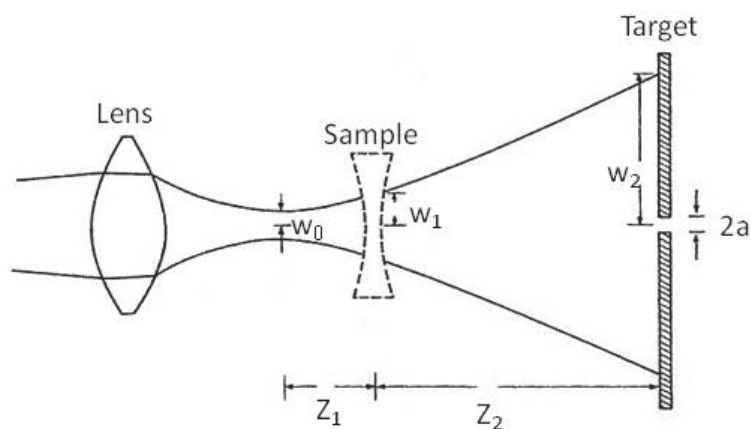


Figure 29. Optical system for thermal lens apparatus

Thermal lens instrumentation can be classified in two categories, single- and double- beam.⁵⁵ The advantage of the single-beam configuration is that it is less complex than the double-beam, but the latter has more flexibility and suitability in the analysis of wider spectral region.⁵⁸ Single-beam TL spectrometers are unique among thermal lens instruments because the same laser is used in both excitation and signal detection, this adds simplicity and ease of operation. This configuration was commonly used in early stages of the technique to evaluate signal dependence on laser power, optical pathlength, beam divergence, sample concentration, and flow dynamics.^{58, 59} This configuration captures multiple points along the transient increase of the thermal lens signal and it can provide faster and more accurate determinations than a double-beam setup.^{57, 59} In this case, the probe laser is a cw beam whereas the excitation beam could be cw or pulsed laser.

The double-beam TL spectrometer has separate use of lasers for the pump and probe beams. Nowadays signal averaging devices allow precise monitoring of the modulation imposed on a stable probe laser by a thermal lens. Double-beam TL

spectrometers could be set- up in two configurations, collinear and transverse. In the collinear configuration, both beams are precisely aligned collinearly for the whole optical path. On the transverse configuration, the excitation beam, and the probe beam are aligned perpendicular in the center of the sample.

Theoretical Description of the TL

The thermal lens effect has been previously described.⁶⁰⁻⁶³ Whether the laser excitation is pulsed or continuous, the pump-probe geometry is collinear or transverse, and the sample is stationary or flowing, theoretical models have been developed to account for the experimental observations. Although these models are limited to specific experimental conditions, they have led to a better understanding of the factors governing the intensity of the thermal lens. Thanks to this it is possible to achieve its optimization and use as an ultrasensitive spectroscopic technique.

The TLS signal can be described in terms of the focal length of the TL formed within the sample. A simplified description calls for a thin lens, with the assumption that $\alpha.l \ll 1$, and unit quantum efficiency for heat production, where α is the absorption coefficient, and l is the lens thickness. A sample excited by a laser beam with an irradiance E of the form shown by equation 35, will produce a time dependent TL with focal length, $f(t)$, as described in equation 36.

$$E_r = \frac{2\Phi_0}{\pi W^2} e^{-2r^2/W^2} \quad (35)$$

and

$$f(t) = f_{(\infty)} \left(1 + \frac{t_c}{2t} \right) \quad (36)$$

where E_r is the radial dependent irradiance in watts per square meter (W/m^2), Φ_0 is the incident radiant power in watts, w is the 1/e2 radius of the pump beam, w^2 is the spot size of the laser beam, f_∞ represents the steady state focal length formed at infinite time (in meters), and t_c is the characteristic thermal time constant expressed in seconds. At constant pressure, the steady state focal length of the TL depends on the refraction index, temperature, and the beam's spot size as shown in equation 27.

$$f_\infty = \frac{\eta_0 \pi \kappa w^2}{\Phi_0 \alpha l \left(\frac{d\eta}{dT} \right)_p} \quad (37)$$

and

$$t_c = \frac{w^2 \rho C_p}{4\kappa} \quad (38)$$

where κ ($\text{J.s. cm}^{-1}.\text{K}^{-1}$) is the thermal conductivity, η_0 the refractive index of the medium where detection takes place, η the refractive index of the sample, T the temperature in Kelvin, ρ the density in kg/m^3 , and C_p the specific heat capacity (J kg K^{-1}).

Because of the temperature gradient formed in the neighborhoods of the excitation point, the thermal diffusion process is a consequence of the tendency of a system to return to its thermodynamic equilibrium. Thermal diffusion is defined by the nature of the solvent.

The general equation of energy conservation for an irradiated sample can be expressed as follows:

$$\frac{\partial T_{(r,t)}}{\partial t} = D_{th} \nabla^2 T_{(r,t)} - v_x \frac{\partial T_{(r,t)}}{\partial x} + \frac{1}{\rho C_p} Q_{(r,t)} \quad (39)$$

where $T_{(r,t)}$ is the temperature as a function of radial position and time, D_{th} is the thermal diffusivity (m^2/s), C_p is the heat capacity of the medium with a uniform velocity v_x in the x direction, and $Q_{(r,t)}$ represents the heating source.⁵⁹

The first term on the right side of equation 39 is a portion corresponding to the thermal diffusion, the second term denotes the heat flow due to convection, and the third term refers to the energy gained by the sample due to laser absorption. The later depends on the excitation mode and other experimental conditions. Under the thin lens approximation, $Q_{(r,t)}$ for cw and pulsed sources are:

$$Q_{(r,t)} = \frac{2\alpha P_{av}}{\pi w^2 t_0} \{e^{-2(x^2+y^2)/w^2}\} (1 + \cos \omega t) \quad (40)$$

$$Q_{(r,t)} = \frac{2\alpha E_0}{\pi w^2} e^{-2(x^2+y^2)/w^2} \quad (41)$$

where t_0 is the duration of a laser pulse with energy E_0 propagating in the z direction perpendicular to the x and y coordinates, and P_{av} is the average power of a cw beam, which is modulated at a frequency $F = \omega/2\pi$.

Lastly, solving equation 39 for a given temperature, the non-uniform radial distribution of the refractive index could be calculated by⁶³

$$\eta_{(x,y,t)} = \eta_0 + \frac{\partial \eta}{\partial T}(x, y, t) \quad (42)$$

TL Cryostat and Vacuum Chamber

The TL apparatus has been designed in order to be able to carry out TLS experiments at cryogenic temperatures. Therefore, the sample cell is connected to a cryostat (International Cryogenics, Inc., model 31-4000). The cryogen used is liquid nitrogen (LN₂), although liquid helium (LHe) can also be used if the experiment requires it. This device features a 12 L Dewar isolated by a 10 L shield to minimize cryogen boil-off that occurs as the system moves towards restoring thermal equilibrium with the surroundings. Figure 30 shows a detailed diagram of the cryostat and the vacuum system. A copper block is attached to the base of the

Dewar, and capillary tubes drive the cryogen from the bottom of the dewar to the head of the block, also referred to as the cold-head. The cryogen flows through the cold-head, and its flow is regulated with a metering valve operated with a vernier handle. The base of the cryostat has four ports for several purposes. One of them is used for vacuum measurement of the cryostat chamber, using a MKS cold cathode ionization gauge for high vacuum, and a Varian E c0531 vacuum gauge for the initial mechanical vacuum. Another port is used as an electrical feed. The other two ports are used for sample admission. Accurate control of the cold head temperature is executed by a filament heater with a maximum power output of 50 W.

There are two Silicon diode thermometers attached to both, cold-head and cell, which allow the reading and control of the temperature in the system. These diodes are operated with a current of 10 μ A. The diodes are connected to a Scientific Instruments Temperature Controller (SI-9700) in order to accurately read and control the temperature up to the 0.001 K. This unit offers a digital display, and can be operated directly from the device's front panel or remotely by the LabVIEW® graphical interface provided by the manufacturer.

The vacuum chamber (bottom of Figure 30) is an aluminum unit of 7.1" in depth and 8.7" in external diameter, attached at the bottom of the dewar. Its function is to isolate the sample cell from the surroundings of the laboratory. It has four windows, of 2" in diameter each, symmetrically placed in front of each other across the chamber diameter. One of the window ports is connected to a cryogenic pump CTI-Cryogenics Helix Cryo Torr 8F, which can achieve thermal isolation with high vacuum (10^{-7} Torr and below). A flexible aluminum hose attaches the cryopump to the chamber which helps minimize transference of mechanical vibrations.

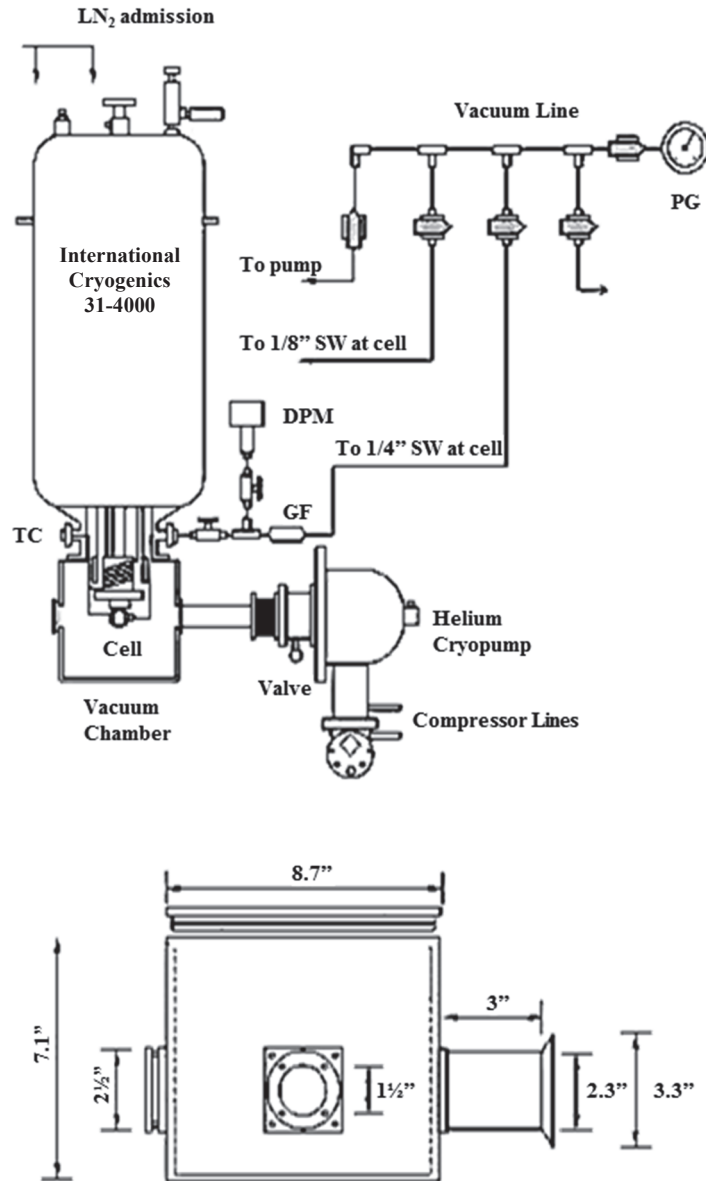


Figure 30. Description of the cryostat and vacuum chamber use in the TL experiment.

The other three window ports have sapphire windows of 3 mm thickness. These seal the chamber with the use of rubber O-rings and are attached to the chamber's body with flat aluminum flanges. Initial operation of the cryopump requires pressures lower than 100 mTorr; therefore, evacuation with a mechanical pump is necessary as first stage. This can be

accomplished through a vacuum port located at the top of the cryostat. A complete set of instructions for the cryostat operation can be found in Appendix D

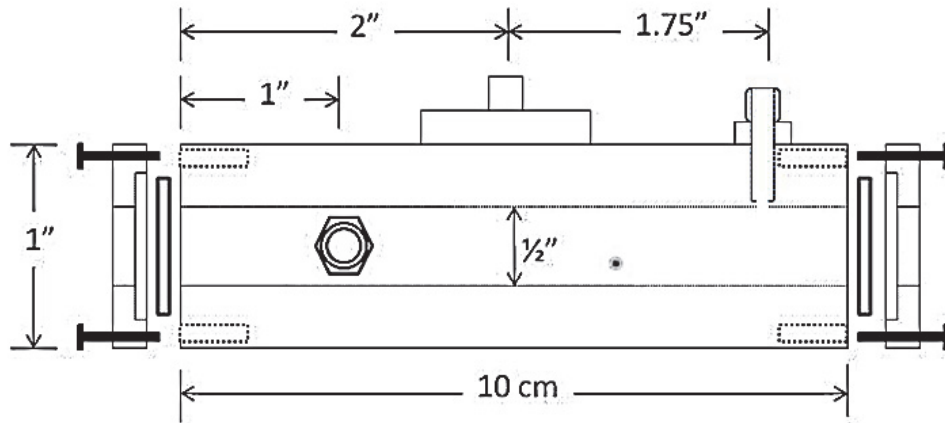
TL Cell Design

Figure 31 shows the sample cryo-cell details and dimensions. The cell is made out of copper (OFHC) and it has a cylindrical internal cavity of 0.5" (1.27 cm) in diameter and 3.937" (10 cm) in length. It has three sapphire windows of 0.75" (1.905 cm) in diameter and 2 mm thick located on each end of the cell and in one of the sides, at the symmetry center. The sapphire windows caused no significant change in the power emerging from the cell, nor polarization of the beam. The windows are sealed to the sample cell with indium O-rings, and fastened with squared flanges as shown in Figure 31.

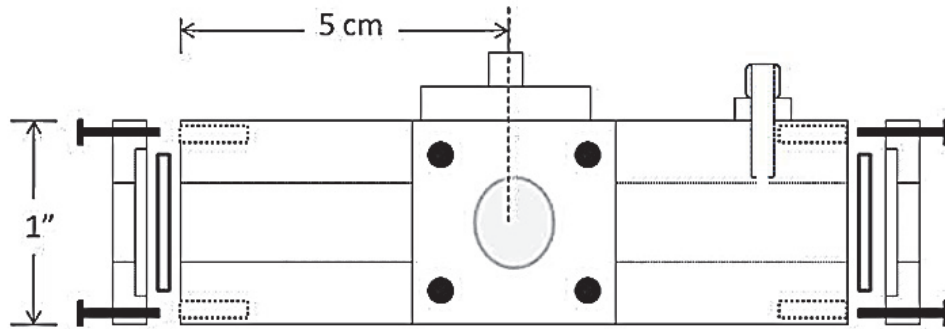
The introduction of the sample into the cell is achieved by two sets of Swagelok to NPT adapters. A 1/8" brass connector is placed on the top of the cell to ensure complete filling, and facilitate faster flow of the condensed gases into the cell. A 1/4" brass connector is next to the vacuum line, and close to a pressure meter, to allow accurate measurements of sample intake. This is further discussed later in this chapter, in the section titled sample preparation. This inlet is also convenient when promoting turbulence in order to facilitate a homogeneous mixing.

Connection of the sample cell to the cold-head of the cryostat is achieved through a customized copper plate. The connection between them requires a temperature transmittable copper paste. The same paste is used to affix two temperature sensors in different locations of the cell. The cell is screwed below the cryostat tank and inside a vacuum chamber. The vacuum chamber also has sapphire windows which are aligned with those of the copper cell.

Right:



Left:



Front and rear ends:

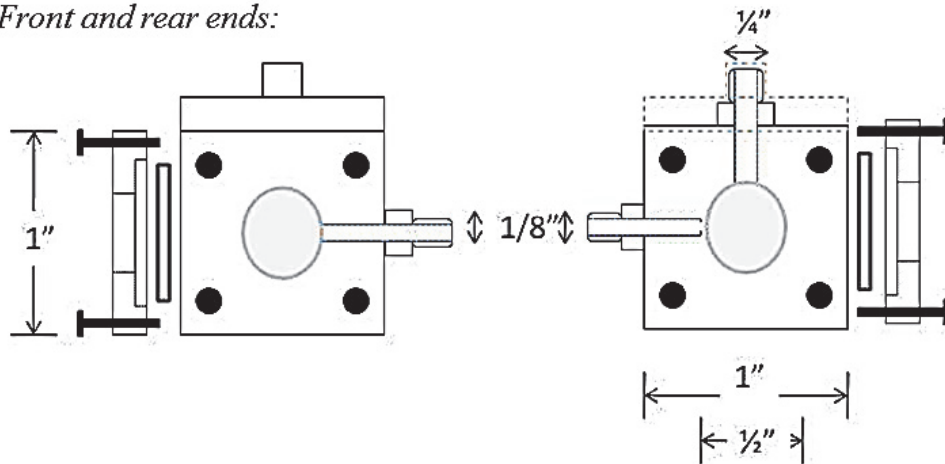


Figure 31. TLS 10 cm copper cell.

TL Experimental Setup

The thermal lens collinear configuration used in this work is shown in Figure 32. The excitation beam is a tunable continuous-wave (cw) dye laser (Coherent CR-599), which is pumped with a wavelength of 514 nm by an argon ion laser (Spectra Physics, model Stabilite 2017). The dye laser is scanned in the range of the Rhodamine-6G dye, from 15800 to 17400 cm^{-1} , with the use of a stepper motor (Miniangle Stepper Astrosyn, type 23pm-C002) of 1.8 degrees per step. The stepper motor is controlled remotely by a computer with LabVIEW® software. A small fraction of the excitation beam is optically extracted, modulated at 250 Hz (Stanford Research Systems (SRS) chopper model SR 540), detected with a photo-diode (Newport, model 882), and sent to the reference port of a lock in amplifier (Ithaco 3962A) via BNC connectors.

Alternatively, another excitation beam is aligned co-linearly with the output of the dye laser. This radiation is provided via fiber optics by a continuous wave (Coherent 899) Ti:Sapphire ring laser which provides an alternative scanning range between 700 to 800 nm or 12500-14300 cm^{-1} . Before the co-alignment of this beam with the dye laser output beam, the Ti:Sapphire radiation coming out of the fiber optic is collimated with a combination of planar-convex lenses. Wavelength tuning of the (0.17 cm^{-1} bandwidth) dye and Ti:Sapphire lasers is accomplished with a birefringent filter driven by a stepper motor. Similarly to that of the dye laser, the Ti:Sapphire stepper motor is also controlled using the same LabVIEW® program. The Coherent 899 laser is pumped by a solid state, frequency doubled, Neodymium Yttrium Vanadium Oxide (Nd: YVO4) laser (Coherent-Verdi) providing single wavelength (532 nm) at a power of 5W.

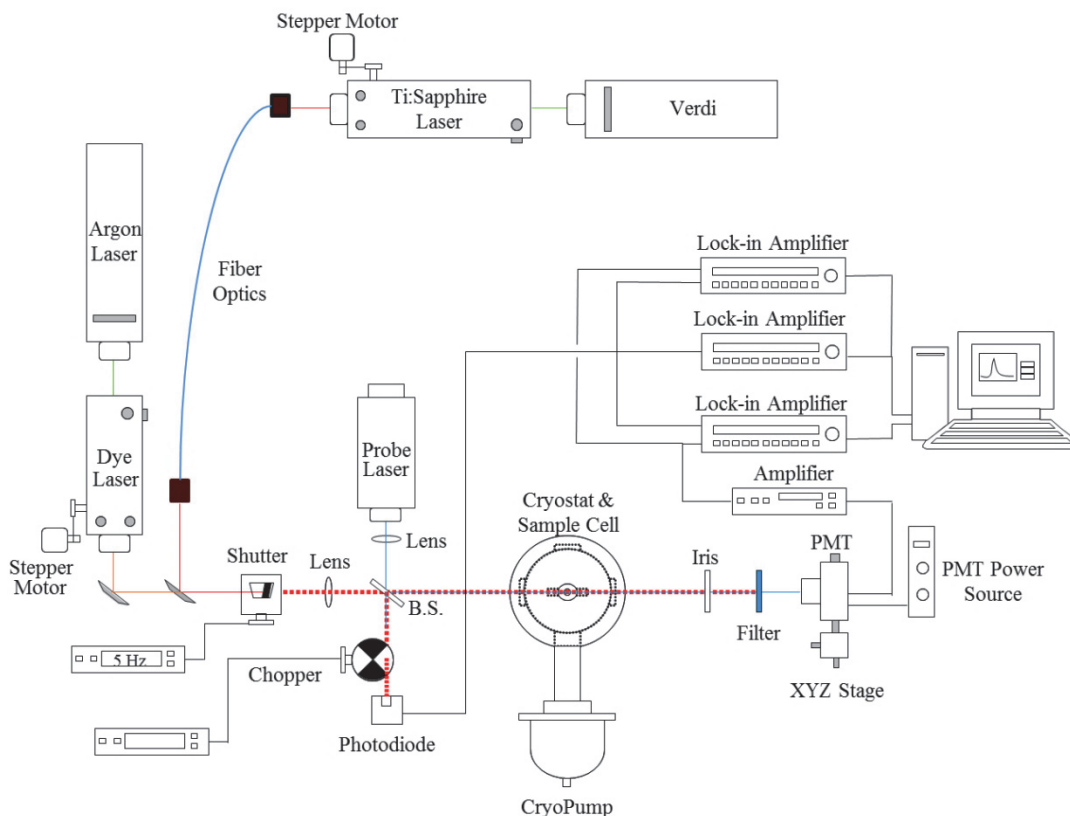


Figure 32. Extended range thermal lens spectrometer.

After coupling, the excitation beams are modulated by a low frequency optical shutter (Electro-Optical CH-60) operated with a function generator (BK Precision, model 3011A) usually having a modulation frequency between 5 and 1 Hz. The modulated excitation beam is focused at the sample cell. The spot radius and confocal distance at that position are 0.20 and 51 cm for the dye laser, and 0.15 and 51 cm in the case of the Ti:Sapphire laser.

The cw probe beam is a single wavelength (488 nm) Spectra Physics argon ion laser, model 161B-13. Before entering the vacuum chamber, the excitation and expanded probe beams are overlapped with a blue dichroic filter and propagated collinearly through the sample cell. Expansion of the probe is accomplished by a diverging lens to obtain a spot size

larger than the excitation beam's. At the cell, its spot radius is 0.90 cm and its confocal distance 87 cm.

Upon exiting the cryostat chamber, an iris is placed in the path of the beam to spatially select the probe center. Then, an interference filter blocks the excitation beam while just transmitting the probe beam. Any residual transmission of the excitation beam is eliminated by placing a blue glass filter before the detector.

The probe beam intensity is recorded with a photomultiplier tube from GCA McPherson, model EU-701-93. A 20 μm diameter pinhole installed on a xyz stage allows precise location of the signal and intensity maximization. The signal is pre-amplified with an SRS low noise pre-amplifier, model SR 560; and finally sent to another Ithaco 3962A single-phase lock-in amplifier.

When using both excitation sources, constant changes to the sensitivity range of the lock-in amplifier are needed when changing back and forth from one laser to the other. This is due to the differences in output power between the two excitation sources. Therefore it is convenient to add a third lock-in amplifier to register the signal provided by the second excitation beam, in this case, that is the Ti:Sapphire laser.

The complete control of the system is done with LabVIEW and integration of all the motors and equipment onto a computer card is required in order to provide a user friendly interface between operator and TL apparatus. We use a National Instruments (NI) CB-50LP block followed by an NI PCI-6025E DAQ (data acquisition) board. The data acquisition process and real time plotting of the probe, excitation, and normalized signals are also possible with these hardware and software.

TL Signal and Signal Conditioning

The TL signal is obtained by normalization, which is done by dividing the probe signal output by the excitation beam signal. This results in a normalized thermal lens signal as a function of the wavenumber.

Before attempting any scan, the laser sources should be turned on for long enough to allow them to reach a stable output. Moreover, verification of highly accurate concentric alignment of the excitation and probe lasers should be verified. Fine alignment of all the beams is critical for the success of this experiment; and hence, double checking on this aspect is crucial. When the beams are misaligned a fraction of the signal's intensity, or no signal at all, is observed. The optics and mirrors directing the beams along the apparatus and across the cell, as well as the dichroic lens, are mounted on translational stages. These make possible the displacement in the x, y and z directions. Alignment is monitored by observing the beam spot size after it passed through the sample cell, and at a distance of three meters away from it. In our set-up, the probe beam is enlarged using a 10 cm focal-lens concave lens. It is recommended to map the center of this probe beam with the PMT; this is a good approximation to locate the thermal lens signal since the excitation beams must traverse the sample concentrically with the probe beam.

A low-frequency shutter controlled by a function generator modulates the excitation beams. The shutter receives 4 V square signal with frequencies between 0.5 to 10.0 Hz. The oscillatory nature of the TLS is a direct consequence of this modulation. As a general rule of thumb we could say that the lower the concentration of the sample, the slower the modulation frequency. This is because highly diluted solutions may require longer times to develop a detectable TL signal. The signal generator also provides the trigger of the TL event; hence, its

reference signal is connected to the reference ports in those lock-in amplifiers where the excitation beams' signals are connected to.

The power of the excitation beams changes over the entire range of the dye during one scan, which is why the TL signal should be normalized as described before. The lock-in amplifier can be programmed to perform this operation by using “Ratio” function built in it. Figure 33 shows a diagram of the proper connection required between all three lock-in amplifiers in order to be able to perform the ratio function when the two excitation sources are used in consecutive scans. The outputs of the lock-in amplifiers, located in the back of each unit, are used to transfer the measured voltages via GPIB from each of the “reference” lock-in units to the “main” lock-in, where the ratio function is undergone. The latter then sends all the information to the computer for data acquisition.

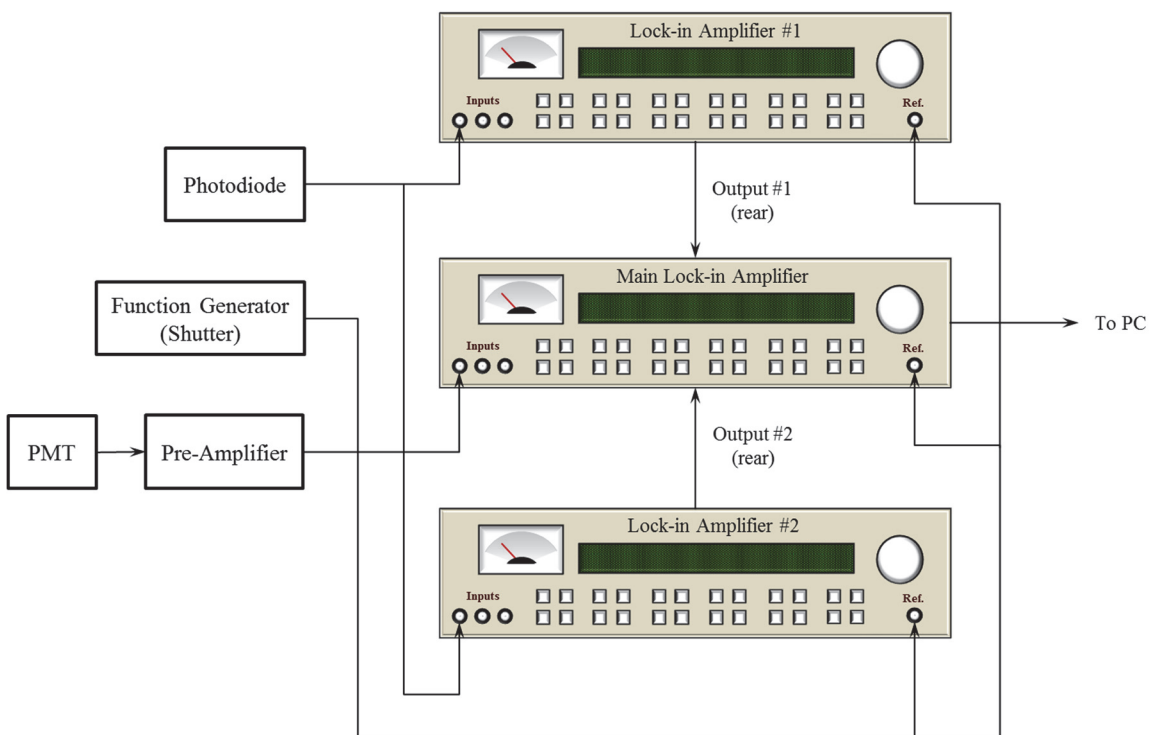


Figure 33. Lock-in amplifiers connection diagram.

Normal operation of the photomultiplier tube that monitors the probe beam intensity requires 1000 V, and the use of a 20 μm pin hole cap before its photosensitive area. Like all the optics, the PMT is mounted on a translational stage that permits movement in the x, y and z directions. This allows for the accurate location of the signal maximum. Complete filtering of the excitation beam before it reaches the PMT is critical to avoid interferences by spurious light, which would obscure the TLS. This can be done by using a blue glass interference filter. The output signal of the PMT is fed to a low-noise pre-amplifier. A 50 Ω cap is connected to the feeding terminal to avoid high voltages that may leak from the detector as product of random jittering. Cut-off filters on the amplifier reduce the signal noise. Typically, the settings used on this pre-amplifier were as follows: 0.03 and 30 Hz for the lower and upper limits; respectively, AC coupling, and a gain of 2x.

The output of the pre-amplifier feeds the main lock-in amplifier. The AUTOSET function on the main panel of the main lock-in amplifier may be used to automatically optimize the acquisition parameters. Nevertheless, the phase, sensitivity, dynamic range, and time constant could also be manually modified; and at times this was indeed needed. The previous must be done with the cell under vacuum conditions and after proper alignment of the beams has been accomplished. Tune the excitation beam to the wavelength at which maximum absorption is expected for a given sample. Then, find the center of the probe signal by adjusting the position of the PMT. When a maximum intensity is found, the AUTOSET function of the lock-in amplifier must be activated. These steps must be repeated until the maximum intensity of the normalized TL signal is reached.

Very diluted solutions, with mole fractions of 10^{-3} or lower, require intensities above the 300 μV . The value of the time constant, τ , depends on the noise levels but its typical

values are 1 and 3 seconds. A higher value of τ is usually the consequence of noisy or weak signals. In general, if the alignment is optimum, mapping times depend on the concentration of the sample. High concentrations of the analyte produce high signal intensity, which is easily mapped, while diluted solutions produce weak signals, requiring more time to maximize. Another consequence of high concentrations is the saturation of the TL signal.

Similarly to the CRD experiments, the TL spectra are obtained using a LabVIEW interface developed in our lab. A detailed description of this code is found in appendix D. In this work, most of the spectra were taken with two and three laser set-up configurations.

TL Experimental Procedure

Calibration

The micrometer screws on both, the dye laser and the Ti:Sapphire laser, must be calibrated periodically to obtain reliable TL results. The calibration is necessary whenever the adjustment knobs are used to re-align the laser after cleaning the optics. This is usually necessary when a decrease on the lasers performance is observed. Optics cleaning procedures can be found in Appendix C.

The calibration of the laser is necessary in order to convert the micrometer positions of the birefringent filter to wavenumbers (cm^{-1}). This is accomplished by using a monochromator and recording the resulting wavelength at every position of the micrometer screw. This is usually repeated for intervals of 5 – 10 micrometers until the desired range is covered. A plot of wavenumber vs. micrometer positions is obtained and a polynomial fit can be used as the calibration equation. The latter can then be entered in the LabVIEW software program so that the measured spectra are correctly positioned.

Sample Condensation

Once the temperature set point is stabilized, the insertion of the sample components into the sample cell is carried out. First, the components are allowed to pre-mix inside the connection pipes (Figure 30). For a binary sample of benzene and ethane in which the latter acts as cryogenic solvent, a desired pressure of benzene is first loaded into the pipes followed by approximately 2.5 atm of the solvent. After pre-mixing of the gases, these are then introduced into the sample cell by opening the Swagelok valve to the 1/8" cell port. When the sample cell is almost full the 1/4" inlet port, located on top of the cell, must be opened to avoid bubble formation inside the cell. This procedure promotes homogenization of the solution during the solvation process. A rise of the temperature in about 2 or 4 K during the condensation process is expected because of the phase change that each component undergoes. The filling time of the sample cell is around 45 - 60 minutes. The longer this process takes the shorter the time it takes for the temperature in the cell to stabilize to the set point. Thus, after condensation of the sample a waiting time for accurate temperature control is required. No bubbles should be observed inside the cell after this operation has been completed. If this is not the case, then allow more gas inside the cell until it is full of the cryogenic solution, followed by temperature stabilization waiting time. This last step is repeated as needed.

Thermal Lens Spectroscopy and the Lakes of Titan

From the moment the Voyager 2 spacecraft first identified Saturn's largest moon, Titan, approximately 35 years ago, it has been object of increasing interest for the scientific community. Initially there was a strong believe that Titan was mostly covered by oceans of methane in the same way that earth is covered by oceans of water. In 2004, after the launching of the Cassini-

Huygens mission to the Saturn's system and the landing of the Huygens probe on the surface of this Saturn's satellite, the hypothesis of these oceans of methane was proven wrong. Nevertheless, Huygens' experimental data and dozens of flybys around this moon over the course of the last ten years, show confirming evidence of the existence of lakes. In July 2008 Brown et al.^{64, 65} confirmed the presence of liquid on the surface where the lake-like shapes were numerous.

Not only were they able to prove the presence of liquid on the surface of the moon, Brown also announced that the Ontario Lacus, one of the large lakes observed in the moon's south pole, contained liquid hydrocarbons, and positively identified the presence of ethane.⁶⁶ Since then, ethane and several other simple hydrocarbons have been identified in Titan's atmosphere. It is also known that a methane cycle exists in Titan's thick atmosphere just like the earth has its water cycle. Ethane and other hydrocarbons are the photochemical products of the breakdown of methane by sunlight and, at Titan's surface temperatures; these substances can exist as both liquid and gas. Thus, Titan's weather relies on methane-ethane rather than water.

The chemical composition of the lakes of Titan is not well determined yet. The atmosphere is rich in methane, which makes the detection of other compounds in the lakes of Titan difficult since in situ measurements are not possible yet. Therefore, the best way to get a good estimate of the chemical composition of these lakes is to elaborate models and simulations based on known data. Cordier et al.⁶⁷ have estimated values for the mole fraction of several chemical compounds in the atmosphere. The mole fractions are shown in Table 13.

In this chapter the C-H $\Delta\nu = 6$ vibrational overtone of benzene, the C-H $\Delta\nu = 5$ of ethane at low temperatures, and $\Delta\nu = 6$ of ethylene in solution with ethane are presented. Spectra were obtained using thermal lens spectroscopy (as described in Chapter Four). In the past our laboratory has used TL to study samples of pure hydrocarbons at room temperatures,⁶⁸ as well as cryogenic solutions of hydrocarbons dissolved in rare gases.^{12, 68}

Table 13. Chemical Composition of Titan's Lakes at the Poles and Equator Proposed by Cordier et al.⁶⁷

Compound	Equator (93.65 K)	Poles (90 K)
Main composition (mole fraction)		
N ₂	2.95 x 10 ⁻³	4.90 x 10 ⁻³
CH ₄	5.55 x 10 ⁻²	9.69 x 10 ⁻²
Ar	2.88 x 10 ⁻⁶	5.01 x 10 ⁻⁶
CO	2.05 x 10 ⁻⁷	4.21 x 10 ⁻⁷
C ₂ H ₆	7.95 x 10 ⁻¹	7.64 x 10 ⁻¹
C ₃ H ₈	7.71 x 10 ⁻²	7.42 x 10 ⁻²
C ₄ H ₈	1.45 x 10 ⁻²	1.39 x 10 ⁻²
H ₂	5.09 x 10 ⁻¹¹	3.99 x 10 ⁻¹¹
Solutes (mole fraction)		
HCN	2.89 x 10 ⁻² (s)	2.09 x 10 ⁻² (s)
C ₄ H ₁₀	1.26 x 10 ⁻² (ns)	1.21 x 10 ⁻² (ns)
C ₂ H ₂	1.19 x 10 ⁻² (ns)	1.15 x 10 ⁻² (ns)
C ₆ H ₆	2.34 x 10 ⁻⁴ (ns)	2.25 x 10 ⁻⁴ (ns)
CH ₃ CN	1.03 x 10 ⁻³ (ns)	9.89 x 10 ⁻⁴ (ns)
CO ₂	3.04 x 10 ⁻⁴ (ns)	2.92 x 10 ⁻⁴ (ns)

(s): saturated

(ns): non-saturated

We have also studied binary cryogenic solutions of benzene in methane with a customized UV-vis spectrophotometer.⁶⁹ In this case, despite the fact that both components can undergo vibrational transitions, it is possible to unequivocally show the transitions of both components by looking at an electronic transition of benzene as well several overtone transitions of the solvent methane. Figure 34 shows this spectrum which was obtained with the UV-vis apparatus described in detail in appendix A.

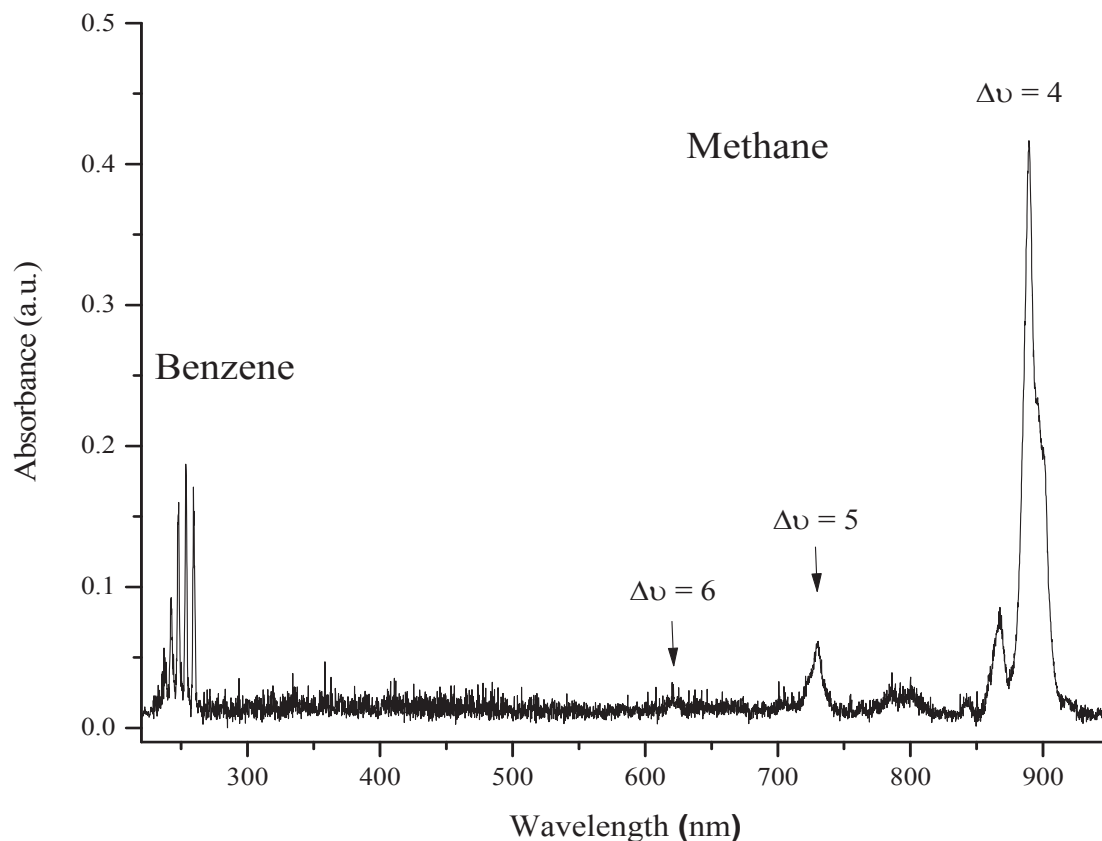


Figure 34. UV-vis spectrum of benzene in liquid methane at 97 K. This spectrum was obtained with the experimental setup described in appendix A.

The next step on our approach to simulate the lakes of Titan is to study these simple binary solutions utilizing the TL technique. This requires that both components can undergo overtone transitions without the possibility for their bands to overlap with each other, hence allowing an unequivocal identification of both compounds. In order to be able to study these types of solutions it is critical to accommodate a TL setup in which this result can be achieved. The spectra of benzene at room temperature and liquefied ethane were recorded with the extended range thermal lens spectrometer showed in Figure 32. Measurements of diluted solutions of ethylene in liquid ethane were attempted using the same experimental configuration without much success thus far.

Table 14 shows the different wavenumber ranges obtained with each of the pump lasers, as well as the molecules studied with them. Perhaps, this table represents a summary of the versatility of this extended design. In general lines, the experimental set up utilizes a dedicated heating beam for the solvent transitions (Ti:Sapphire laser) and a different source (dye laser) for the solute in the solution. In addition, the flexibility and generally wide range of the dye laser allows for convenient adjustment based upon the selected solute. This can be made by preparing a different dye solution. Whether the solute is an alkane, an alkene, or an alkyne; these can be targeted with the selection of a different dye molecule.

Table 14. Excitation beam ranges and selected solutes and solvents of the binary cryo-solutions studied with the extended range TL spectrometer.

Source	Range (cm ⁻¹)	Molecule	$\Delta\nu$
Ti:Sapphire Laser	13,387 – 13,862	Ethane	5
		Methane **	5
Dye Laser – R6G*	15,974 – 17,727	Ethylene	6
		Benzene	6
		Propylene **	6
		Isobutylene **	6

(*): *Rhodamine 6G*

(**): *Lopez-Calvo*⁷

TL Spectrum of Benzene

The fifth C-H overtone of neat liquid benzene at room temperature was obtained using a quartz cuvette of 2 mm pathlength. The power of the pump laser was 4 W, the dye laser had an absorption of 80 – 85% which generates an excitation beam of 540 mW, and the shutter frequency was 4 Hz. The maximum signal is localized at 16466 cm⁻¹ with a band width (FWHM) of 219.7 cm⁻¹. Both parameters are in agreement with the

literature values reported previously.^{70, 71} Figure 40 shows the TL spectrum of benzene at room temperature.

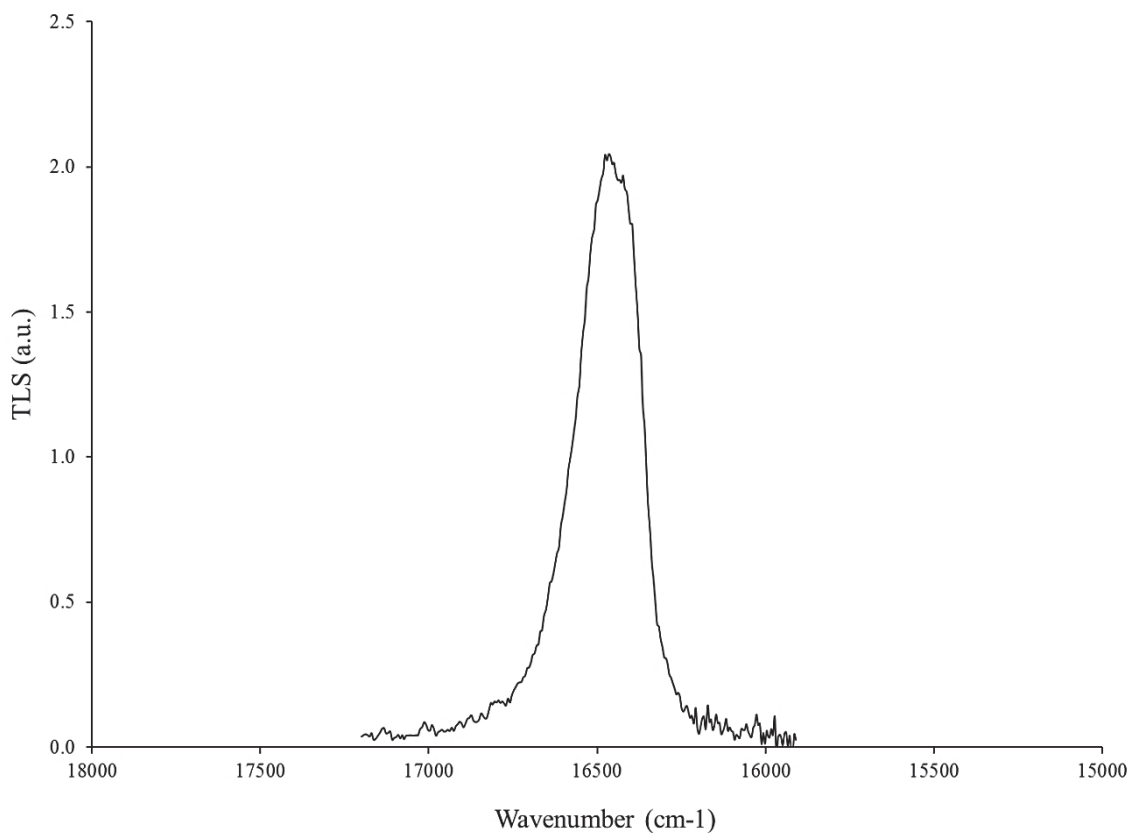


Figure 35. TL spectrum of the C-H $\Delta\nu = 6$ of benzene at room temperature, obtained with the extended range TL setup.

TL Spectrum of Ethane

The fourth C-H overtone of liquid ethane at 91 K was obtained using a cryo-cell with quartz windows (as explained in Chapter Four) of 100 mm pathlength. The power of the pump laser, excitation beam, and the shutter frequency were set identically to the benzene experiment. The maximum signal is localized at 13415.4 cm^{-1} with a band width (FWHM) of 136.0 cm^{-1} . Both parameters have similar values to those found in the literature.⁶⁸ Figure 36 shows the TL spectrum of ethane at 91 K.

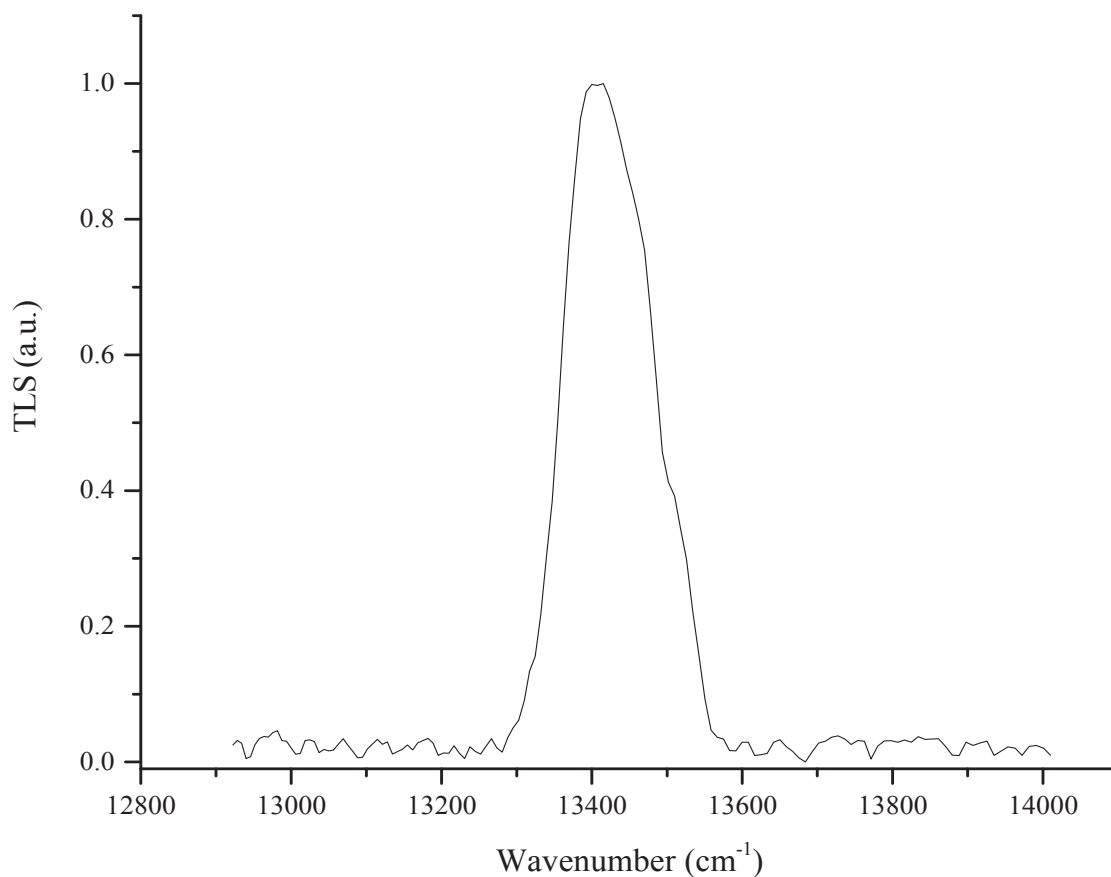


Figure 36. TL spectrum of the C-H $\Delta\nu = 5$ of ethane at 91 K, obtained with the extended range TL setup.

TL Spectrum of an Ethylene – Ethane cryo-solution

The fifth and fourth C-H overtones of liquid ethylene and ethane, respectively, were obtained at 100 K using the same cryo-cell and experimental conditions as in the cases of benzene and ethane. It must be mentioned that the ethylene band required of a large amount of graphical treatment after the raw data for it was obtained. This was due to the presence of noise and its baseline being very uneven, which is unusual for a TL spectrum.

The maximum absorption of the solvent ethane is shown at 13415 cm^{-1} with a band width (FWHM) of 147.4 cm^{-1} , which is in close agreement with our previous result

for ethane. On the other hand, the maximum absorption of the solute ethylene is shown at 17124 cm^{-1} with a band width (FWHM) of 328.6 cm^{-1} . It must be pointed out that the later values are far from those reported in the literature for the ethylene molecule,⁶⁸ the actual reported band maximum value for this molecule in a cryogenic solution fluctuates around 16460 cm^{-1} depending on the solvent. Similarly, the width at half height for the $\Delta\nu = 6$ transition of C_2H_4 is reported to be 142 cm^{-1} for a 0.04% solution in a transparent solvent. Although the FWHM increases with the concentration, the rather wide value obtained in this experiment, along with the wrongful maximum frequency, confirms that this was not a good result. Figure 37 shows the TL spectrum of the 10% $\text{C}_2\text{H}_4\text{-C}_2\text{H}_6$ solution at 100 K.

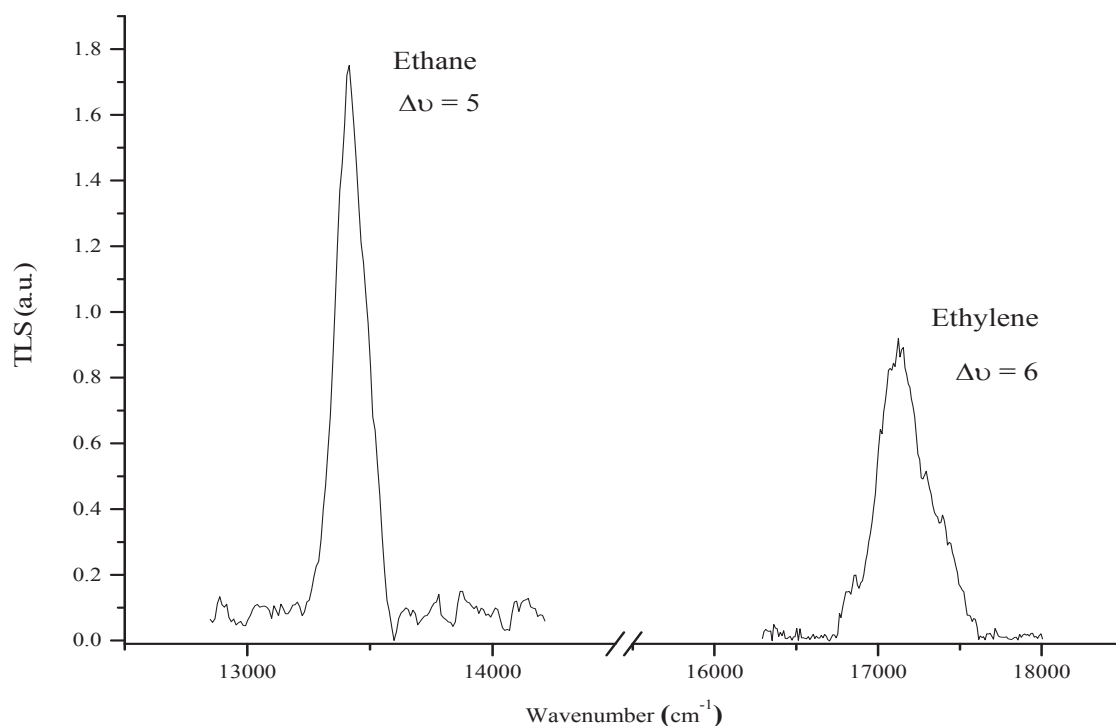


Figure 37. TL spectrum of the 10% $\text{C}_2\text{H}_4\text{-C}_2\text{H}_6$ solution at 100 K obtained with the extended range TL setup. Notice that the ethylene band is not showing in the expected frequency range.

CHAPTER FIVE

Spectral Moment Analysis

A spectrum usually contains a large amount of information in it. However, interpretation of this information in terms of molecular dynamics is not always an easy task. This is particularly true for molecules in which not all the bonds are equivalent like in the case of methane or benzene (if we are interested on the C-H overtones only). And even on simple molecules with this description, combination bands and electronic transitions might still complicate a spectrum (i.e. acetylene).

Gordon⁷² found a way to reduce spectral analysis to a few simple features by developing the concept of the spectral moments, or simply moments hereby. These moments are simply a tool, or method, that are the result of a molecular statistics analysis and should not be confused with any of the other quantum mechanical parameters like the angular momentum, or moment of inertia. If $P_{(\omega)}$ is the spectral transition probability at an angular frequency ω , the n^{th} moment of the spectrum is defined as:

$$M_{(n)} = \int (\omega - \omega_0)^n P_{(\omega)} d\omega \quad (43)$$

where ω_0 is some suitably chosen band maximum. It is usually convenient to normalize $P_{(\omega)}$ so that $M_{(0)} = 1$. Equation 44 shows the expression for the probability, $P_{(\omega)}$, as a function of the cross section, $\sigma_{(\omega)}$, used by Gordon in his moment analysis of absorption spectra.

$$P_{(\omega)} = \frac{\sigma_{(\omega)}}{\omega} \quad (44)$$

Therefore, the general expression for calculating the normalized spectral moment of an absorption band results from the combination of equations 43 and 44, as follows:

$$M_{(n)} \equiv \int (\omega - \omega_0)^n \omega^{-1} \sigma_{(\omega)} d\omega / \int \omega^{-1} \sigma_{(\omega)} d\omega \quad (45)$$

For lower values of n , these lower moments are shown to depend on simple molecular distribution functions, whereas higher moments will represent more complex properties of the system.

Gordon established that the intensity distribution of a spectrum can be represented as a set of polynomials on ω . The infinite set of coefficients in the expansion, are a linear combination of the moments. Therefore the moments characterize the spectrum uniquely and any other property such as the frequency at the maximum intensity, the width at half height, or intensity at any specific frequency, will depend on all of the moments. Hence, all of the low order moments are the only simple properties of a spectrum.

From an experimental point of view, moment analysis assists in the interpretation of spectra as follows:

1. The first moment can locate the true frequency of the internal molecular transition, without making the usual assumption that it coincides with the maximum absorption. This is particularly useful in the case of asymmetric bands, or when matrix effects start showing in a liquid sample.
2. The second moment contains two types of terms: (a) the fluctuations of the difference in potentials between the ground and the excited state, and (b) rotational kinetic energy terms. Therefore if the fluctuations on “a” are small, and assuming an adiabatic process, $M_{(2)}$ is essentially a measurement of the average rotational kinetic energy. Nevertheless, in liquid and gaseous samples, $M_{(2)}$ does not take into consideration the intermolecular hindering of the rotational motion.
3. The higher moments contain kinetic energy terms, angular properties, and higher fluctuations of the shift.

Before we start establishing the relationship between the moments and the quantum mechanics quantities involved in the dynamics of molecules, some important approximations must be made. Starting with the reasonable assumption that the bonds within a molecule are stronger than the intermolecular interactions, this means that the internal degrees of freedom move faster than the overall rotation and the translation of the molecule. Based on this intermolecular adiabatic approximation, one must therefore neglect the collision induced absorption as part of the initial absorption transition.

The second major approximation is to assume that the spectroscopically active molecules are sufficiently far apart (i.e., in diluted solutions). Furthermore, even in the case of pure phases, exciton type splittings often have a small effect on the moments of vibrationally weak transitions. Finally, the ground state is assumed to be the only one populated thermally.

First Moment

A general expression found by Gordon⁷³ for the first moment is shown in equation 46:

$$\begin{aligned}
M_{(1)} &\equiv \int (\omega - \omega_0) \omega^{-1} \sigma_{(\omega)} d\omega / \int \omega^{-1} \sigma_{(\omega)} d\omega \\
&= \left[\hbar \sum_k \langle i | (\boldsymbol{\varepsilon}_k \cdot \mathbf{S}_k \cdot \mathbf{m}_k)^2 | i \rangle \right]^{-1} \sum_k \langle i | (\boldsymbol{\varepsilon}_k \cdot \mathbf{S}_k \cdot \mathbf{m}_k)^2 [V^\beta - V^0 \\
&\quad + \frac{B_k^\beta(x) - B_k^0(x)}{B_k^0(x)} T_x + \frac{B_k^\beta(y) - B_k^0(y)}{B_k^0(y)} T_y + \frac{B_k^\beta(z) - B_k^0(z)}{B_k^0(z)} T_z \rangle \quad (46) \\
&\quad + hc [\boldsymbol{\varepsilon}_k \cdot \mathbf{S}_k \times \mathbf{m}_k - \boldsymbol{\varepsilon}_k \cdot (\mathbf{O}_k \mathbf{S}_k) \cdot \mathbf{m}_k] \cdot \mathbf{B}_k^\beta \cdot [\boldsymbol{\varepsilon}_k \cdot \mathbf{S}_k \times \mathbf{m}_k - \boldsymbol{\varepsilon}_k \cdot (\mathbf{O}_k \mathbf{S}_k) \cdot \mathbf{m}_k] \\
&\quad + hc \sum_{j \neq k} [\boldsymbol{\varepsilon}_k \cdot (\mathbf{O}_j \mathbf{S}_k) \cdot \mathbf{m}_k] \cdot \mathbf{B}_j^0 \cdot [\boldsymbol{\varepsilon}_k \cdot (\mathbf{O}_j \mathbf{S}_k) \cdot \mathbf{m}_k] + \frac{1}{2} \hbar^2 \sum_j M_j^{-1} |\boldsymbol{\varepsilon}_k \cdot (\nabla_j \mathbf{S}_k) \cdot \mathbf{m}_k|^2 \Big| i \rangle
\end{aligned}$$

Here $\boldsymbol{\varepsilon}_k$ is the electric field of the incident radiation averaged over the region of molecules nearby molecule k . \mathbf{S}_k is the shielding tensor for the k^{th} molecule, defined by

$\boldsymbol{\varepsilon}_k(\text{local}) = \boldsymbol{\varepsilon}_k \cdot \mathbf{S}_k$. \mathbf{m}_k is the transition dipole moment for the β^{th} transition. V^0 and V^β are the intermolecular potential energy functions for the ground and the β^{th} excited states, respectively. $B_k^0(x)$ and $B_k^\beta(x)$ are the rotation constants about the x principal axis of inertia of the k^{th} molecule, in the ground and excited state, respectively. \mathbf{B}_k^β is the tensor, diagonal to the principal axis of the moment of inertia, with the diagonal values $B_k^0(x)$, $B_k^0(y)$, and $B_k^0(z)$. T_x is the rotational kinetic energy operator for rotations around the x principal axis of inertia. \mathbf{O}_k is the gradient operator with respect to rotations about the principal axes of inertia. ∇_j is the gradient operator with respect to the center of mass of the j^{th} molecule. M_j is the mass of the j^{th} molecule. The matrix elements in the state $|i\rangle$ represent averages over the external coordinates only, in the initial state of the system. The sums over k extend over all identical molecules which are active to the β^{th} transition. The sum on j includes all the molecules in the system.

After further developing each of the terms of equation 46 separately, Gordon found the final expression for the first moment which is used to calculate the shift band origin, $\tilde{\nu}_s^\beta$, in units of cm^{-1}

$$\begin{aligned}
 \tilde{\nu}_s^\beta = & \int \sigma_{(\tilde{\nu})} d\tilde{\nu} / \int \tilde{\nu}^{-1} \sigma_{(\tilde{\nu})} d\tilde{\nu} - \left(\frac{kT}{2hc} \right) \left(\frac{B^\beta(x)}{B^0(x)} + \frac{B^\beta(y)}{B^0(y)} + \frac{B^\beta(z)}{B^0(z)} - 3 \right) \\
 & - [B^\beta(x)(\hat{m}_y^2 + \hat{m}_z^2) + B^\beta(y)(\hat{m}_x^2 + \hat{m}_z^2) + B^\beta(z)(\hat{m}_x^2 + \hat{m}_y^2)] \\
 & - (3.3 \times 10^{48})(\rho/M)^2 [B(x)(\alpha_{yy} - \alpha_{zz})^2 + B(y)(\alpha_{xx} - \alpha_{zz})^2 + B(z)(\alpha_{xx} - \alpha_{yy})^2] \\
 & - (2.1 \times 10^{64})\hbar\rho^{8/3}(\alpha_{xx}^2 + \alpha_{yy}^2 + \alpha_{zz}^2)N_0c^{-1}M^{-11/3} \quad (47)
 \end{aligned}$$

Here \hat{m}_x , \hat{m}_y , and \hat{m}_z are the direction cosines of the transition dipole moment relative to the principal axes of inertia. ρ is the molecular density, M is the molecular weight, α is the polarizability of the molecules, and N_0 is the Avogadro's number.

The last two terms of equation 47 are each generally smaller than 0.1 cm^{-1} , and therefore can usually be neglected. Taking this into consideration we can conclude that the shift band origin can be expressed as follows:

$$\begin{aligned} \tilde{\nu}_s^\beta \cong & \int \sigma_{(\tilde{\nu})} d\tilde{\nu} / \int \tilde{\nu}^{-1} \sigma_{(\tilde{\nu})} d\tilde{\nu} - \left(\frac{kT}{2hc} \right) \left(\frac{B^\beta(x)}{B^0(x)} + \frac{B^\beta(y)}{B^0(y)} + \frac{B^\beta(z)}{B^0(z)} - 3 \right) \\ & - [B^\beta(x)(\hat{m}_y^2 + \hat{m}_z^2) + B^\beta(y)(\hat{m}_x^2 + \hat{m}_z^2) + B^\beta(z)(\hat{m}_x^2 + \hat{m}_y^2)] \end{aligned} \quad (48)$$

The last term of equation 48 is referred to as the ‘‘orientation term’’, whereas the term preceding the latter is known as the ‘‘shape term’’. $\tilde{\nu}_s^\beta$ represents the average energy transferred to the internal degrees of freedom of an active molecule, per excitation of the β^{th} internal level, when the sample is illuminated with radiation.

Second Moment

The discussion for the second moment starts by writing equation 45 in terms of $n=2$ as follows

$$M_{(2)} \equiv \int (\omega - \omega_0)^2 \omega^{-1} \sigma_{(\omega)} d\omega / \int \omega^{-1} \sigma_{(\omega)} d\omega \quad (49)$$

The calculation begins with the quantum mechanical expression for the absorption cross section (equation 50), using the dipole approximation and first order perturbation theory for the interaction with the radiation:

$$\sigma_\omega = (4\pi^2/n\hbar c) \sum_F |\langle F | \sum_F \boldsymbol{\varepsilon}_k \cdot \mathbf{S}_k \cdot \mathbf{u}_k | I \rangle|^2 \times \omega \delta(\omega - \omega_F + \omega_I) \quad (50)$$

where n is the refractive index, \mathbf{u}_k is the total dipole moment operator for the k^{th} molecule, $\boldsymbol{\varepsilon}_k$ is the amplitude of the average electric field due to the incident radiation at a frequency ω , and \mathbf{S}_k is the shielding tensor that relates the average field to the local field. Following a similar analysis to that of the first moment, Gordon concluded that the second moment, $M_{(2)}$, is given by

$$\begin{aligned}
M_{\beta}(2) = & \frac{1}{(hc)^2} \left\{ \frac{\langle \mathbf{m} \cdot \mathbf{S} \cdot \mathbf{S} \cdot \mathbf{m} (V^{\beta} - V^0)^2 \rangle}{\langle \mathbf{m} \cdot \mathbf{S} \cdot \mathbf{S} \cdot \mathbf{m} \rangle} - \frac{\langle \mathbf{m} \cdot \mathbf{S} \cdot \mathbf{S} \cdot \mathbf{m} (V^{\beta} - V^0) \rangle^2}{\langle \mathbf{m} \cdot \mathbf{S} \cdot \mathbf{S} \cdot \mathbf{m} \rangle^2} \right\} \\
& + 2 \left(\frac{kT}{hc} \right) \left\{ (\hat{m}_y^2 + \hat{m}_z^2) \frac{[B^{\beta}(x)]^2}{B^0(x)} + (\hat{m}_x^2 + \hat{m}_z^2) \frac{[B^{\beta}(y)]^2}{B^0(y)} + (\hat{m}_x^2 + \hat{m}_y^2) \frac{[B^{\beta}(z)]^2}{B^0(z)} \right\} \\
& + (\text{Tr} \mathbf{B}^{\beta})^2 - (\hat{\mathbf{m}} \cdot \mathbf{B}^{\beta} \cdot \hat{\mathbf{m}}) (\text{Tr} \mathbf{B}^{\beta}) + \hat{\mathbf{m}} \cdot \mathbf{B}^{\beta} \cdot \mathbf{B}^{\beta} \cdot \hat{\mathbf{m}} \\
& + \left(\frac{kT}{hc} \right) \left\{ \frac{\Delta B(x)}{B^0(x)} + \frac{\Delta B(y)}{B^0(y)} + \frac{\Delta B(z)}{B^0(z)} \right\} (\text{Tr} \mathbf{B}^{\beta} - \hat{\mathbf{m}} \cdot \mathbf{B}^{\beta} \cdot \hat{\mathbf{m}}) \\
& + \frac{1}{4} \left(\frac{kT}{hc} \right)^2 \left[3 \left(\left\{ \frac{\Delta B(x)}{B^0(x)} \right\}^2 + \left\{ \frac{\Delta B(y)}{B^0(y)} \right\}^2 + \left\{ \frac{\Delta B(z)}{B^0(z)} \right\}^2 \right) \right. \\
& \left. + 2 \left\{ \frac{\Delta B(x) \Delta B(y)}{B^0(x) B^0(y)} + \frac{\Delta B(x) \Delta B(z)}{B^0(x) B^0(z)} + \frac{\Delta B(y) \Delta B(z)}{B^0(y) B^0(z)} \right\} \right] \quad (51)
\end{aligned}$$

where \mathbf{m} is the transition dipole moment defined as

$$\mathbf{m}_k^{\beta} \equiv \langle \beta_k | \mathbf{u}_k | 0_k \rangle \quad (52)$$

The first term to the right of the equality in equation 51 is known as the shift-fluctuation term, and depends on the difference between the intermolecular potential energies of the excited and ground state. The other four terms represent dynamical contributions to $M_{(2)}$, and depend on the molecular geometry, direction of the transition dipole moment, and the temperature. Notice how these dynamical contributions are independent of the intermolecular potential energy.

The shift-fluctuation term is always positive and hence, an experimental measurement of $M_{(2)}$ gives an upper limit to the average rotational kinetic energy. In the other hand, if the shift-fluctuation term is negligible, the measurement of $M_{(2)}$ is essentially a measurement of the average molecular rotational kinetic energy. This makes the second moment particularly useful as a tool to evaluate intermolecular interactions like those involved in the formation of dimers, or any other in which the rotation of the molecule is hindered by those surrounding it.⁷⁴

Bulanin simplifies equation 51 within the classical limit and with allowance for rotational-vibrational interactions in the molecules.⁷⁴ The second moment is then expressed as follows:

$$M_{\beta}(2) = 4 \left(\frac{kT}{hc} \right) B^{\beta} + 8 \left(\frac{kT}{hc} \right) \left(\frac{\Delta B}{B^0} \right) B^{\beta} + 16 \left(\frac{\Delta B}{B^0} \right) (B^{\beta})^2 + \frac{8}{3} (B^{\beta})^2 \quad (53)$$

Calculation of First and Second Moment from TL Spectral Data

We can now calculate the first and second moments for the spectra of benzene and ethane obtained by means of thermal lens spectroscopy, shown earlier in this chapter. The simplest method to do so involves the definition of a new abscissal scale that expresses the symmetry of the spectral band in a more simplified way. We now define a “j-scale” based on the inherent features of a spectrum like the frequency, ω , and the full width at half maximum, FWHM. We most first define b as

$$b = FWHM/2 \quad (54)$$

thus

$$j = (\omega - \omega_0)/b \quad (55)$$

$$dj = d\omega/b \quad (56)$$

The general expression for the n^{th} moment with the j-scale method is defined as⁷⁵

$$M_{(n)} = \frac{\int_{-10b}^{+10b} j^n y_j dj}{\int_{-10b}^{+10b} y_j dj} \quad (57)$$

where y_j represents the signal obtained during the acquisition of the spectrum. Typically, the integration limits are chosen to be within a range equal to ten times the FWHM to assure the full coverage of the spectral band.

The calculation starts by calculating the area of the spectrum as shown in the denominator of equation 57. Then we proceed to calculate the first and second order curves depicted by the numerator of equation 57. Figures 38 and 39 show these resulting curves for the overtone transition $\Delta\nu=6$ of benzene, obtained with TLS, and previously shown in Figure 32. It is also convenient to generate a simulated curve of each of these in order to simplify the calculation of their absolute areas. These are also shown in Figures 38 and 39. After obtaining these areas the application of equation 57 results in a very straight forward step.

This identical calculation was done for the fourth overtone spectrum ($\Delta\nu=5$) of ethane, also obtained by TLS and shown in Figure 36. The overall result is shown in Figure 40. This figure shows the progression of the graphical calculation from the original spectrum to the graphical, non-normalized second moment. Similarly, after calculating each moment, a simulated curve was also calculated.

This j-scale method for the calculation of spectral moments was also used to calculate the $M_{(2)}$ of the ν_4 transition of benzene (674 nm) with spectral data obtained with Fourier transformed infrared spectrometer (FT-IR). The result was compared against the value reported by Gordon. Table 15 summarizes the results of the calculation of the first and second moment for the overtone transitions mentioned thus far.

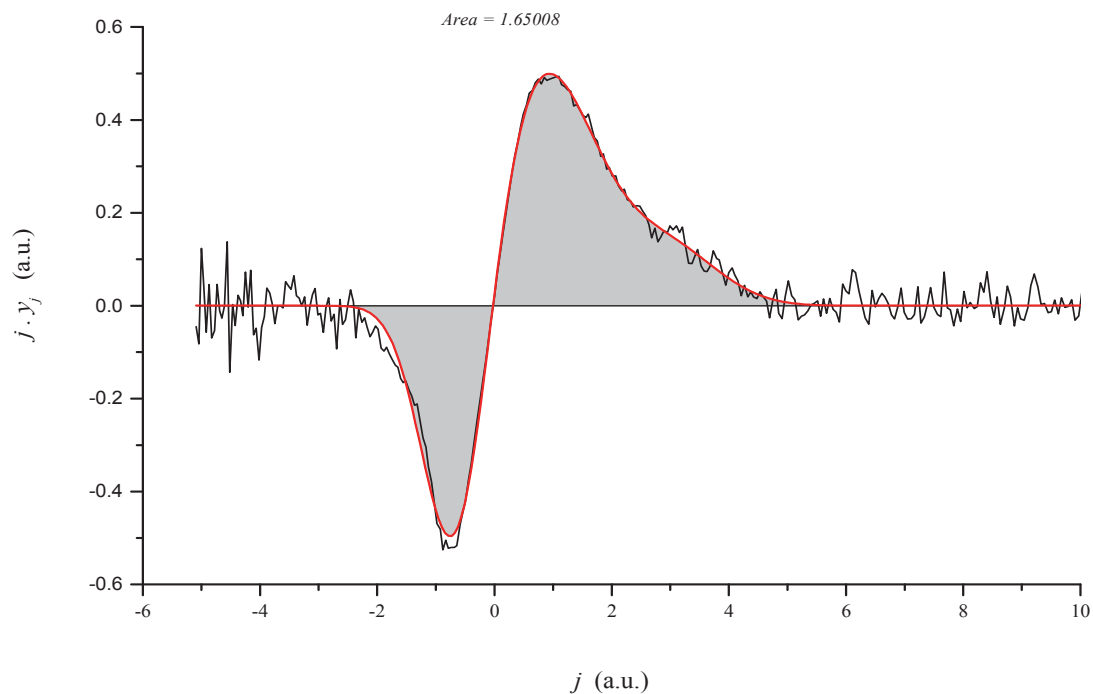


Figure 38. Graphical calculation of $M_{(1)}$ for the fifth overtone of benzene. Non-normalized $M_{(1)}$. The red traces are the simulated curves obtained via deconvolution calculations.

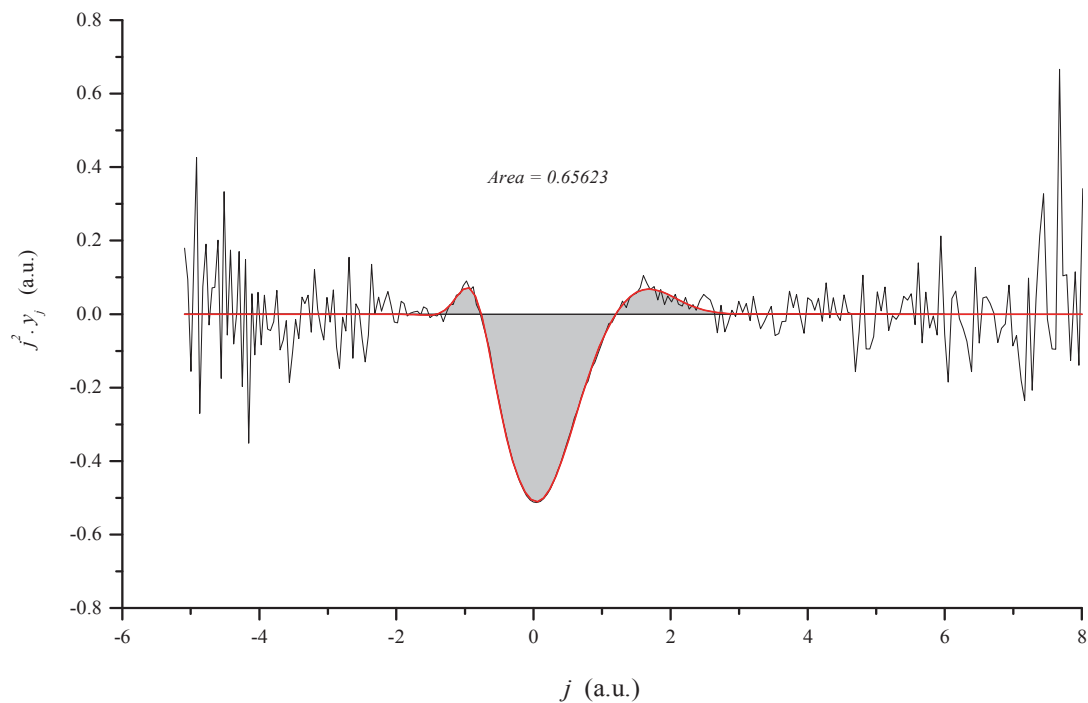


Figure 39. Graphical calculation of $M_{(2)}$ for the fifth overtone of benzene. Non-normalized $M_{(2)}$. The red traces are the simulated curves obtained via deconvolution calculations.

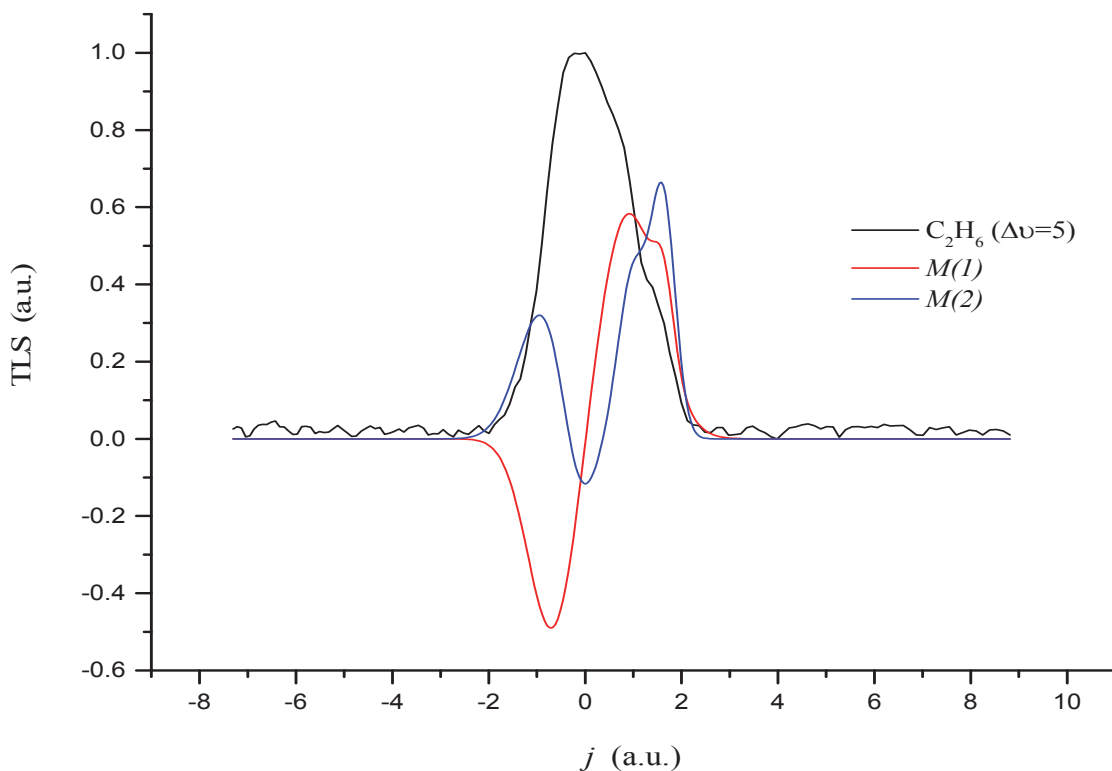


Figure 40. Graphical calculation of $M_{(1)}$ and $M_{(2)}$ for the fourth overtone of liquid ethane at 91 K.

Table 15. Calculation results of benzene and ethane spectral moments

Molecule	Band/Transition	$M_{(1)}$ (cm^{-1})	$M_{(2)}$ (cm^{-2})	Reference
Benzene	ν_4	-----	169.0	Gordon ⁶⁸
Benzene	ν_4	1.11	149.27	This work
Benzene	$0 \leftarrow 6$	0.79	0.65	This work
Ethane	$0 \leftarrow 5$	0.82	0.62	This work

Conclusions

As it can be seen in Table 15, the value $M_{(2)}$ obtained in this work for the bending transition of benzene (ν_4) is only slightly deviated from the value reported by Gordon. Our value is the result of averaging the $M_{(2)}$ obtained for each of five spectra, which were taken with different spectrometers but under approximately the same conditions of pressure, temperature, and density. Despite the discrepancy with the value reported in the literature, and

the limited amount data on this particular field, we feel very confident on the value obtained in this work using the j-method.

The $M_{(1)}$ values shown on the latter table validate the spectra of benzene and ethane obtained with the extended range TL setup used in this work for the analysis of cryo-solutions (Figure 32). In spite the slight asymmetry of the bands shown in both of these spectra, the obtained $M_{(1)}$ values suggest a small deviation of the bands maximums with respect to the actual frequency of the transition.

In regards to the high overtone transitions of benzene and ethane, the $M_{(2)}$ values appear to be trustworthy. It is expected for the $M_{(2)}$ values to undergo a large decrease for higher overtones.^{76,77} In a liquid sample the free rotation of the molecules is hindered by the intermolecular interactions with the neighboring molecules, which may also explain the low values of $M_{(2)}$. In the case of the ν_4 band of benzene, it must be said that the sample was also liquid, but in this case this is the strongest and therefore largest band of benzene in the IR. This should explain the difference in the values with respect to the other liquid samples. Unfortunately there is not much information of $M_{(2)}$ of high overtones in order to establish a more accurate relationship between the experimental values and any reported ones, and therefore we will rely on the demonstrated applicability of the J-method.

The calculation of these spectral moments is a rather new area in our laboratory and therefore, the information shown in this work is inconclusive. Ideally, we should acquire spectra and calculate the second moment for a complete series of transitions, from the fundamental to the high overtones, in order to achieve better conclusions. In our work we employ the calculation of these spectral moments for two main reasons. First, they represent a more accurate way to calculate the true frequency of a transition from an asymmetric spectral

band. These are common in overtone spectroscopy and especially when working with the thermal lens spectroscopy technique. Second, these calculations help us attest to the proper functionality of the proposed extended range TL spectrometer.

The calculation of spectral moments represents a great piece of information especially in the case of cryo-solutions. The values of $M_{(2)}$ offer an insight on the nature of the intermolecular interactions occurring in these solutions, which may offer valuable information in simulations of the lakes of Titan. A comprehensive understanding of the behavior of these low order moments at higher overtone transitions is required. This work has provided the basis for this moment analysis and its application to the spectral data obtained in the near IR region, and definitely has pointed out the importance of these calculations. Finally, the calculation of the spectral moments may offer an excellent piece of supplemental information to every spectrum produced in our laboratory.

CHAPTER SIX

General Conclusions and Research Outlook

Phase Shift Cavity Ring Down Remarks

It has been shown how our PS-CRD setup is able. This depends on the step size of the motor that controls the birefringent filter of the dye laser. This step size correlates closely with the calibration between the wavelength of the output of the dye laser and the position of the micrometric of the birefringent filter. The spectra shown show slight shifts of the absorption frequency with respect to the simulated values. This small shift depend on the accuracy of the calibration curve shown on Figure 15.

The quality of the results obtained with PS-CRD can be evaluated with simple empirical observations in regards to the S/N ratio and amount of resolved peaks in a spectrum. This empirical analysis can be used to shorten the optimization of the PS-CRD spectrometer at the beginning of every experiment. Our results show that the acquisition pause is the most influential experimental parameter when looking for the optimal conditions of a PS-CRD experiment. Clearly this relates to the lock-in amplifier's response time, as well as the time it takes the system to complete one full iteration as controlled by the customized software (move motor, acquire data, pause, end of cycle).

Lastly, the evaluation of the off-axis position leaves room for hesitation in regards to the symmetry of the off-axis alignment around the cavity axis. So far, it appears that the best off-axis angle can be found at discrete entry points to the cavity, but considering the symmetry of the high reflectance mirrors, this results to be very

unexpected. A plausible reason for this result could be that the optimal off-axis alignment always depends on the initial on-axis alignment of the beam inside the cavity. A remark must be made in this regards, since the best on-axis alignment does not necessarily means that the beam is located in the geometric center of the HR mirrors. Instead, the best on-axis alignment is simply the one resulting on the longest RDT. Therefore, the HR mirrors are not necessarily in a parallel configuration between them. This fact alone should limit the symmetrical behavior of the off-axis configuration, since the smallest variation in the reflection angle of the beam inside the cavity may have a large effect on the off-axis alignment. This is perhaps a good experiment to carry out on future studies, as it would complement the optimization step associated with every CRD experiment.

Thermal Lens Remarks

The benzene and ethane spectra obtained with the extended range TL spectrometer shown in Figure 32 showed a close correlation to those found in the literature. Unfortunately that is not the case for the cryogenic solution of ethylene and ethane. Despite obtaining a good spectrum for the solvent ethane, the spectrum of the solute ethylene is not accurate. This negative result might be the consequence of very strong matrix effects added to a very low concentration of the solute. Future experiments may consider a slight variation to the experimental approach in which the solvent can be studied through a higher overtone transition than that of the solute. This change takes into consideration the fact that there are less molecules of the solute present in the sample and therefore this situation will be favored by a stronger transition, as it would be a lower overtone. Under this conditions, the solvent should still be readily excited to a higher vibrational state and its this absorption should still be noticeable without major problems. This alternative configuration can be easily achieved in

our experimental setup by changing the dye solution of the dye laser, as well as tuning the titanium sapphire output to any of the other ranges it can achieve as this one can lase in the NIR region which should excite lower over tones of many hydrocarbon molecules. Both, the dye solution and the output range of the Ti:sapphire should be selected as a function of the molecules of interest.

The spectra obtained with the thermal lens technique were studied with the moment analysis by means of the J-method. Although the method showed to be simple and effective for the calculation of low order moments, there is still very little understanding about the correlation of these moments with the high overtone transitions studied in our lab. This is in part due to the lack of experimental data in this area. Understanding the trends of these spectral moment of high overtone transitions could result very useful for all the experiments that take place in our laboratory. These moments help identify the true frequency of a given transition from an asymmetric spectrum ($M_{(1)}$), and also help to understand the molecular interactions occurring in a sample ($M_{(2)}$). These appear to be very important when studying cryogenic solutions since the motion of the molecules in the sample is expected to be strongly hindered by the low temperatures. In the other hand, the spectral moment analysis should also result very useful in the study of gas samples with CRDS, as it might offer insights about the formation and chemical behavior of molecular dimmers, as this might be complementary information for some areas of atmospheric chemistry.

APPENDICES

APPENDIX A

Ultraviolet-Visible Spectroscopy Instrumentation and Procedures

A brief description of the UV-Vis system for cryogenic samples utilized throughout the course of research is offered in this appendix. This apparatus was used as a complementary technique to the Thermal Lens Spectroscopy methods presented in Chapter Four.

UV-Vis Cryogenic Setup

In order to record the spectra of cryogenic solutions in the UV-Vis region a special cell, located inside a vacuum chamber, is connected to a cryostat and is placed inside the sample compartment of a Varian Cary 50 Bio spectrophotometer. Figure A1 shows a diagram of this experimental set up. This system was used to record the secondary absorption band (${}^1B_{2u}$) of benzene, in order to measure its solubility in ethane.

The cryostat is an APD Cryogenic model LT-3-110 and was operated using LN₂ as the cryogen. Here, the LN₂ is transferred from a pressurized supply Dewar (Messer Griessheim Juno) to the head of the cryostat through a transfer line. The flow of the cryogen is regulated by a valve at the top of the cryostat, as well as two flow meters, one connected to the cryostat, and the other connected to the transfer line on the top of the refrigerant Dewar.

The cryostat, shown in Figure A2, has five ports: coolant exhaust, vacuum pump-out, electric feed through, BNC terminal, and a vacuum check point. Ultra-Torr fittings connect both, the coolant exhaust and the vacuum pump-out, to hoses. Remaining ports are sealed with flanges and rubber O-rings.

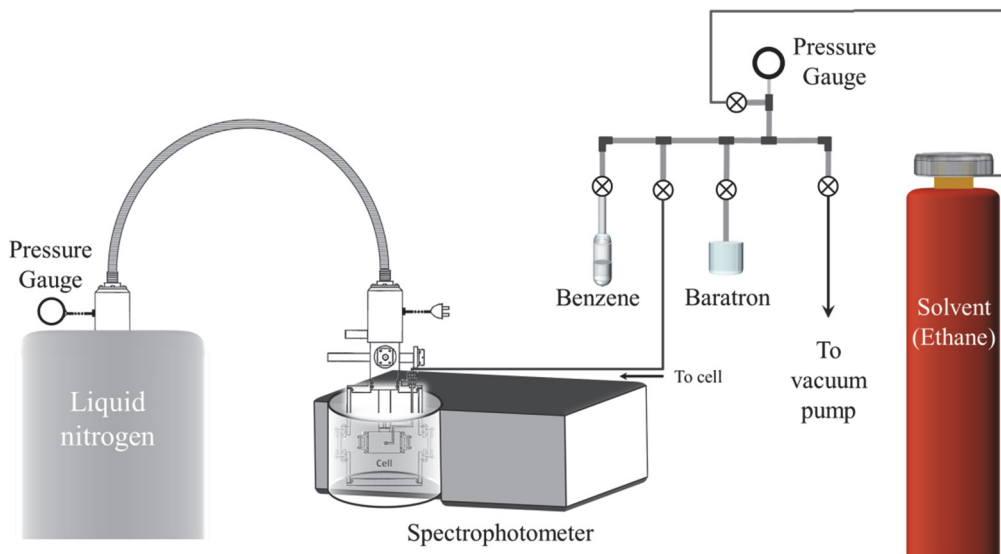


Figure A.1. Experimental set up for the study of cryogenic samples in the UV-Vis region.

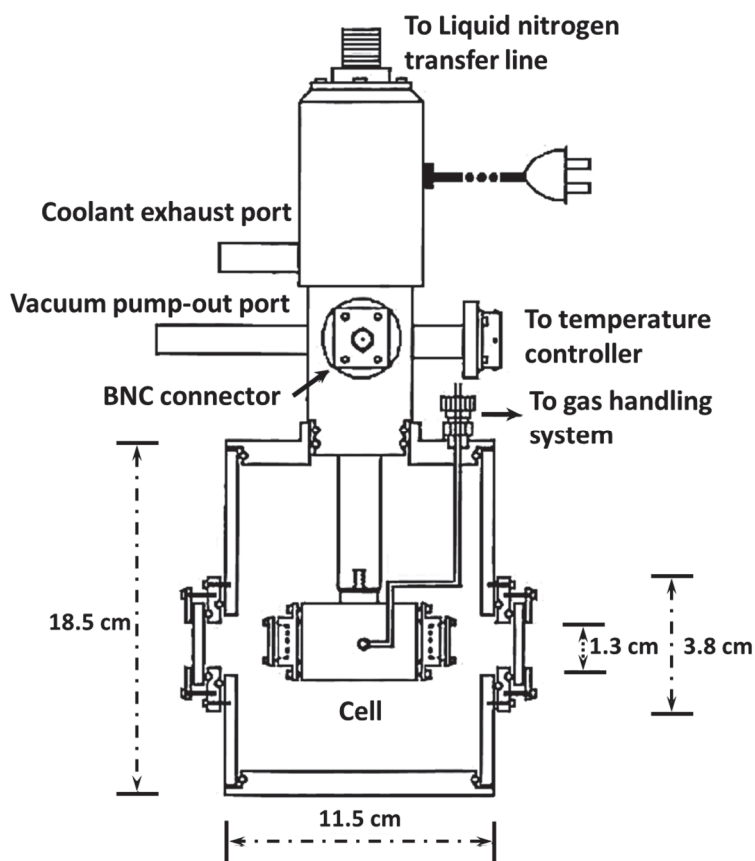


Figure A.2. Diagram of the cryostat head and vacuum chamber for the study of cryogenic samples in the UV-Vis region.

In order to achieve high vacuum conditions inside the vacuum chamber, an initial rough vacuum is made with a mechanical pump. Then, high vacuum is obtained (lower than 10^{-4} Torr) with a diffusion pump. A vent gas heater within the cryostat head must be operated when the cryogen is flowing to avoid freezing of the electrical component. Temperature reading is done using silicon diode sensors in the cryostat head and on the cell. These sensors are connected to a SI-9650 controller, which is also used to control the temperature in the cell. Although, the complete control of the temperature results from a combination of the heater power and the cryogen flow. The latter is accomplished manually.

The SI-9650 has an accuracy of ± 0.5 K, resolution of 0.01 K, and controllability of ± 0.02 K. The vacuum chamber is a custom made aluminum cylinder of 7 1/4" (18.415 cm) in length and 4" of internal diameter. Four windows are symmetrically placed on every side. The windows used are 1" (2.54 cm) in diameter and their material depended on the spectral region of interest. In this work quartz windows were employed. The windows on the chamber were sealed with rubber O-rings and fastened with flat circular flanges.

UV – Vis Sample Cell

The cell is a copper (OFHC) cylinder with dimensions of 1.7" (4.318 cm) in length and 1/2" (1.27 cm) in internal diameter. The sample is admitted through a 1/8" (0.318 cm) stainless steel connection placed on the top of the cell. Similarly to the TL apparatus, stainless steel tubing connects the cell with a gas-handling system through a Swagelok valve. The windows are placed on each end of the cell and fastened with interchangeable circular flanges designed to fit the quartz window's dimensions. A detailed scheme of the cell is shown in Figure A3.

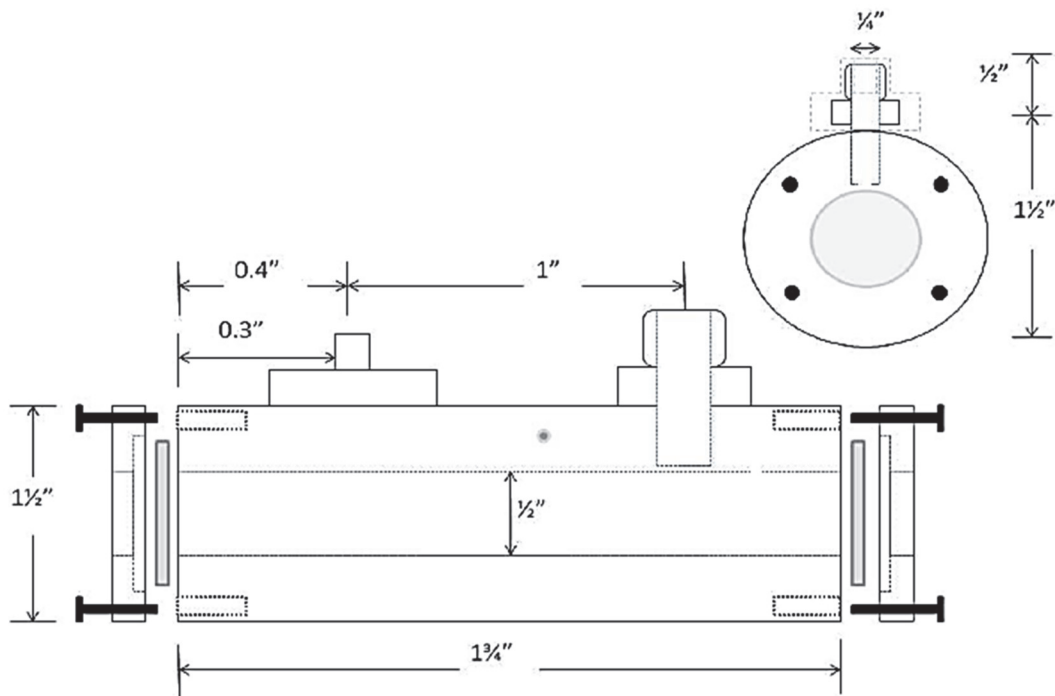


Figure A.3. Diagram of the cell used in the UV-Vis experiment.

UV – Vis Cryostat Operation

The temperature decrease process requires the SI-9650 controller to be turned on in advance. A voltage of 25 V is set as the heater output voltage. The 50-L Dewar is filled with LN₂ using a special transfer hose. The transfer line bayonet is placed into the Dewar and sealed with a rubber sleeve and a hose clamp. To push the refrigerant through the transfer line, pressurization is needed. Therefore, a continuous flow of nitrogen gas is provided at a pressure of 5 psi approximately. The needle valve on the cryostat head (knob) and both flow meters should be open to allow the cryogen flow through the transfer line. This process takes around 30 min before the cryogen starts flowing. When the refrigerant starts to flow, or when the temperature on the cryostat head is 250 K, the vent gas heater has to be plugged to avoid freezing and damage of the electronic components. Allowing the temperature to stabilize in

the coldest value possible (77 K if LN₂ is the cryogen) is recommended, before programming the set point.

Upon the stabilization of the temperature, adjustment of the cryogen flow is done to avoid excess heating when controlling the temperature at the set point. Control of the cryogen is accomplished with the flow meter. Setting it at 20 mm is enough for efficient operation at all the temperatures. The steps required to set the temperature on the SI-9650 are described in the following table:

Table A.1. Steps for programing the SI-9650 to a particular temperature set point.

Step	Key/Button	Action
1	TEMP/EDIT	to choose the sensor to be controlled. (1 = cryostat head; 2 = cell)
2	ENTER	to save the value
3	SET/EDIT + Numeric pad	to set change the temperature set point
4	ENTER	to save
5	MANUAL	to allow the instrument achieve the temperature automatically

Once the temperature set point is reached, a wait of up to 2 hours to allow for stabilization of the temperature is critical. Control of the temperature should be within ± 0.3 K.

UV-Vis Experimental Procedure

Before starting any measurement, the windows of the vacuum chamber and the cell must be aligned with the beam coming from the Cary 50. The spectrophotometer is controlled by the Cary WinUV software and optimized alignment is accomplished by using this user interface. This software is a modular design that allows for the execution of several tasks through a user friendly interface. It makes it possible to optimize and choose the acquisition

parameters for every scan, such as the resolution, velocity, and spectral window of each record. The maximum resolution used was 0.5 nm.

Background Acquisition

Background acquisition is not needed but rather a blank scan of the empty cell in the cryostat chamber. This is done at the same parameter conditions at which the sample is run. These blank scans of the empty cell and cryostat chamber are recorded before every experiment. After the blank is recorded, the cryostat chamber must not be moved from its place to avoid baseline distortion. Due to the inherent limitations of the sample preparation procedure (described next), the blank spectra were acquired at room temperature before every experiment. Not only backgrounds of the empty cell were recorded at room temperature, but also with the pure solvent were obtained.

Sample Preparation

All the samples were prepared *in-situ* using the experimental set-up shown in Figure A4. A known pressure of the gas sample was admitted into the pipes line and the cell at room temperature. In the case of samples like benzene, that is liquid at room temperature, the substance's vapor pressure provided enough gas molecules to reach the pressure wanted. By closing the Swagelok valve, a waiting time of around 5 minutes was needed to achieve pressure equilibrium; thus an accurate reading of the actual pressure of the sample in the cell was obtained. Next, the entry valve to the cell was closed and the injection line was evacuated. A pressure of 1 atmosphere or higher of the solvent gas at room temperature was loaded into the line and then quickly introduced into the cell by opening its entry valve. Then the cell was

cooled until a temperature of about 10 K lower than the boiling point of the solvent. Condensation and mixture of the sample starts occurring in the cell at this point.

Finally, more solvent gas was condensed into the cell using a backing pressure greater than to the vapor pressure at the cryogenic temperature, usually greater than 1 atm. Since the filling of the cell procedure caused turbulence in the solution, no additional mixing was required and solution is assumed to be homogeneous. During the condensation process of the solvent gas, the temperature of the cell increased. A suitable time was once more needed until reaching thermal equilibrium.

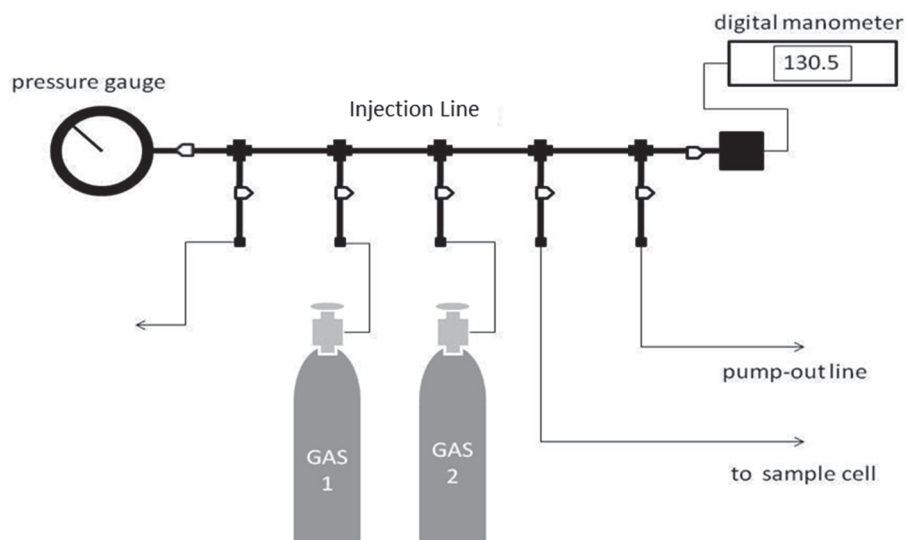


Figure A.4. Experimental set-up for UV-Vis cryogenic sample preparation.

Technical specification of the chemical substances and gases used in the sample preparation are provided in Table A2. To obtain optically transparent liquids and solutions, high purity of the gases was critical. Although purities of 99 % are often acceptable to obtain clear solutions, at times noisy signals were observed as result of impurities in the solvent. In this case further purification procedures were necessary. Concentrations of each solution were calculated as mole fraction,

$$X = \frac{n_{solute}}{n_{total}} = \frac{n_{solute}}{(n_{solvent} + n_{solute})} \quad (A1)$$

For very diluted solutions, $n_{total} \approx n_{solvent}$. Also, matrix isolation effects minimize the interactions of the analyte molecules making the ideal gas approximation a valid assumption. Therefore, the mole fraction is calculated as:

$$X = \frac{P_i}{R \cdot T_i \cdot \rho_{(T)}^{sol}} \quad (A2)$$

where, P_i is the pressure of the sample in atm, R is the ideal gas constant in $L \cdot atm \cdot K^{-1} \cdot mol^{-1}$, T_i is the temperature of the solute at which it entered the cell (room temperature), and $\rho_{(T)}^{sol}$ is the temperature dependent density of the solvent, in $mol \cdot L^{-1}$, at the temperature of the cryogenic solution. Concentration of the solute in solution is expressed in part per million (ppm) by multiplying the mole fraction, X , times 10^6 factor.

Table A.2. Technical specification of chemical substances

Substance	Chemical Formula	Molar mass (g/mol)	Manufacturer	Purity (%)
Methane	CH ₄	16.04	Praxair	99.999
Ethane	C ₂ H ₆	30.07	Aldrich	99.99+
Benzene	C ₆ H ₆	78.11	Aldrich	99.99

Sample Condensation

Once the temperature set point is reached, and remains stable, opening the Swagelok valve lets the solvent enter into the cell until it is filled. There is a temperature rise of around 3-5 K during condensation of the solvent gas, due to phase change process. Because the vacuum chamber is inside the sample compartment of the Cary 50 its windows will not be exposed, this means that there is not an easy way to see when the cell is full. Therefore, quick scans must be performed in order to determine when the cell

is fully occupied. Likewise, when working at temperatures that are too close to the freezing point of the solvent, quick scans can be used to identify when the sample is liquid again. Once again, a suitable time of at least 30 min is allowed for the temperature to stabilize once the sample is in the cell.

Spectra Acquisition

Spectra were acquired following the standard procedure use for conventional UV-Vis spectroscopy with the Cary 50 Bio spectrophotometer. The WinUV software interface allows for the selection of the wavelength range of 200 – 1100 nm. Then the START button engages the Cary 50 to begin scanning. Typical resolution was 0.15 nm, and the average rates for the data were 12.5 and 25 ms per step. The signal/noise ratio largely depends on these parameters. Hence, previous optimization was required at the beginning of each day of experiment.

Shut-down Procedure

When all the spectra were recorded, the sample was slowly evaporated at the set point temperature by partially opening the cell and vacuum line valves. As the solution evaporates, these gases will suffer an expansion towards the vacuum line and beyond. If this expansion occurs too suddenly, the temperature of these vapors will lower dramatically causing them to freeze in the tubes. This may block the apparatus and induce dangerously high pressures in the cell and tubes. To avoid this, it is critical that the cell and system should be evacuated very slowly by barely opening the vacuum valve as indicated earlier. Once the cell is empty, stopping the refrigerant flow is accomplished by closing the knob at the cryostat head and flow meters, and the regulator of the nitrogen

pushing gas. The temperature controller is then set at 250 K and the vacuum line is fully opened upon reaching this set point. Finally, the SI-9650 is at room temperature (290 K). Setting the controller at temperatures over 300 K may cause damaging of the sensors attached to the cell.

The cryogen reservoir is large enough to be used for several runs of this experiment. Therefore, the bayonet of the transfer line could remain inside the Dewar unless clear evidence of line clogging is observed. This is noticeable when the cryogen flow meter indicates an unusual flow rate at the beginning of the experiment or if, as a consequence of this, the temperature in the system does not decrease at the usual rate. Complete maintenance of this bayonet was required three times per month.

APPENDIX B

Cavity Ring Down Alignment Procedure

The alignment procedure is not a complicated process, but it requires attention to details, analytical thinking, and finesse in dealing with the optical system. Mastering the alignment of a CRD system can be achieved with experience. The following procedure explains the alignment process for the CRD cavities developed in our laboratory. It must be noticed that this procedure is based on a typical PS-CRD system, with a continuous source (cw-laser) externally modulated by an electro-optic modulator (EOM), but the actual cavity alignment remains the same regardless of the method. It can also be applied in the case of exponential decay CRD where a pulsed laser is required. Typically, in exponential decay CRD the pulses frequencies are several orders of magnitude lower than those of on PS-CRD, where modulating frequencies are in the order of KHz.

1. Begin with the laser's start-up process and peak the laser power. Also, set the EOM to around 23 kHz for a starting modulator frequency.
2. Adjust the birefringent filter using the micrometer screw on the titanium sapphire laser (or dye laser) to match the maximum reflective wavelength of the mirror set being used.
3. Make sure the cavity is attached to its supporting bronze core block such as the ends of the cavity end up as shown in Figure B1. The fine alignment bolts must be in positions North (N), South (S), East (E), and West (W); whereas the attachment bolts must be in positions NE, SE, SW, and NW.

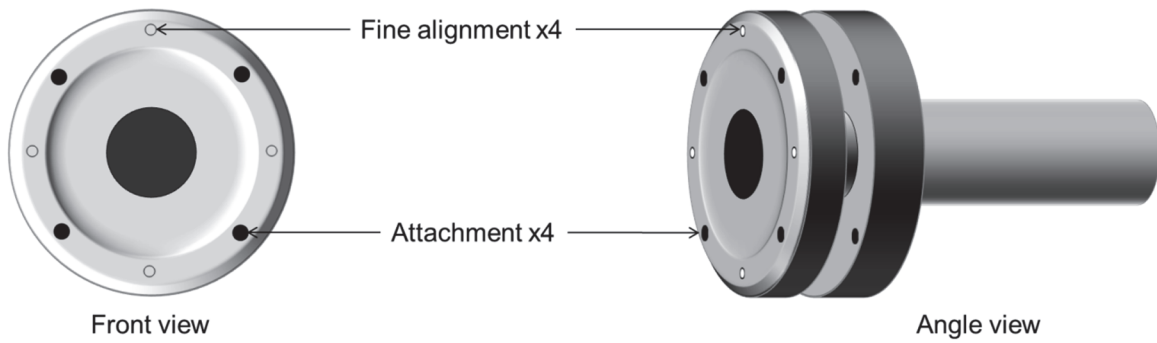


Figure B.1. Front (or back) end of the cavity shown in frontal and angled profile.

4. As an initial approximation, use a ruler to make sure the laser beam remains equidistant from the optic table along its whole extent, but particularly 30 cm before and after the cavity. A height equal to the distance from the center of the cavity to the surface of the optical table is strongly recommended.
5. This is the most critical step and must be followed closely. Use the periscope optics (Figure B2), and turning prism (if any), to adjust the beam so it is going through the center of the sample cell. You may use a ruler as an initial approximation to locate the beam exactly at the geometric center of the cavity aperture. This condition must prevail for both horizontal and vertical dimensions, and in both ends of the cavity. Now, for better accuracy, use a pinhole to verify the beam is at the geometric center of the cavity in both ends. Make adjustments as needed with the periscope optics. After the beam passes through the pinhole in and out of the cavity, neither the periscope nor the cavity should be moved until the alignment is complete.

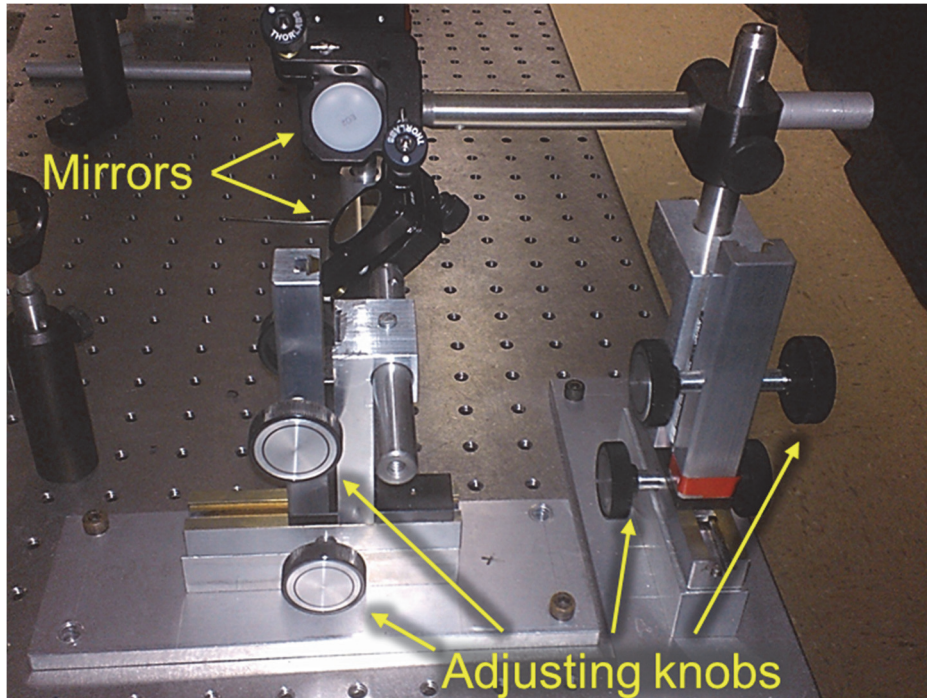


Figure B.2. Periscope used for PS-CRD beam alignment.

6. Block the incoming beam and place a photomultiplier detector (PMT) at the end of the cavity. Allow 2 - 3 inches between the end of the cavity and the PMT. It is strongly advised to have the PMT attached to an X, Y, Z motion stage so that its position can be adjusted in all three dimensions. Connect the PMT to an oscilloscope.
7. Before unblocking the entering beam, lower the laser power and use an optical density filter (if needed), and use an appropriate power meter to adjust the power of the incoming beam to 1 - 2 mW.
8. Turn ON the PMT and set gain at 700 V and unblock the incoming beam. Set the proper time scale on the oscilloscope until you can see a square signal. Use the X, Y, Z micrometric mount knobs to adjust the position of the detector until achieving the maximum amplitude of the square wave. You can

adjust the gain on the PMT as needed although that shall not be set higher than 1000 V. The PMT position should not be changed after this point.

9. Placing a plano-convex lens between the cavity and the detector is often encouraged in order to gather all the radiation coming out of the cavity and focus it onto the PMT, especially after all the mirrors are in position. Nevertheless it is better to place it at this point in the alignment procedure. Attach the plano-convex lens onto another X, Y, Z stage, with the flat side facing the PMT, and adjust its position so that the same amplitude found at the end of step 8 (or better) is achieved. This lens should not be moved after this point.
10. Clean both HR mirrors using spectrophotometric grade methanol and lens tissue as recommended by manufacturer. Optical soap may be used in extreme cases. If the optical soap is used, the spectrophotometric grade methanol must always follow. Achieving the best CRD signal depends greatly on the cleanliness of these HR mirrors.
11. Place the rear mirror on the cell and seal using the appropriate o-ring, rubber for room temperature measurements and indium for low T, making sure the reflective side is facing toward the sample cell. Tighten the mirror to the cell to create a vacuum tight seal between the mirror, o-ring, and cell. Some finesse must be used here to ensure too much pressure is not put on the mirrors or they might be damaged. See Figure B3 for appropriate placement of HR mirrors.

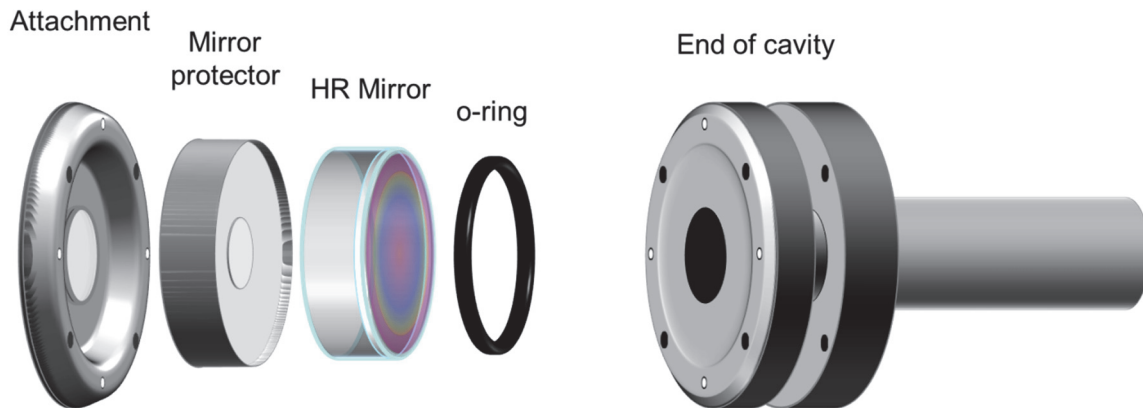


Figure B.3. Attachment of HR mirrors onto the cavity ends.

12. Use a pinhole close to the periscope optics to show the back reflection of the laser beam coming from the rear mirror, as shown on Figure B4.
13. Superimpose the back reflection onto the laser beam coming through the pinhole using the adjustment allen screws on the rear mirror. Do not use the fine alignment screws.

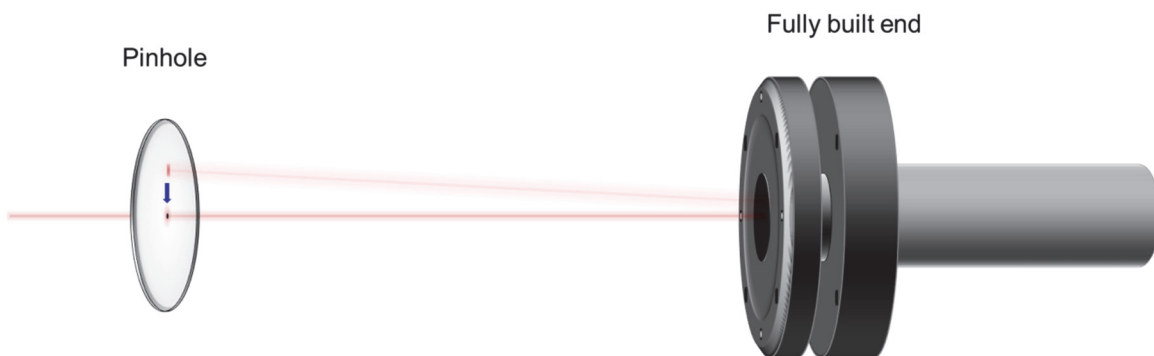


Figure B.4. Reflection of the laser beam onto the pinhole slide after it is reflected from the rear HR mirror.

14. Check for vacuum leaks using a rubber stopper on the front end of the cavity. If vacuum is not achieved, the adjustment screws on the rear mirror must be tightened further until vacuum is maintained. A leak rate of 500 mTorr/min is

acceptable at this point. Once this point was checked you must slowly open the cavity to atmospheric pressure, retire rubber stopper from front end, and repeat step 13.

15. Place the front mirror onto the cell just like the rear mirror.
16. Superimpose the back reflection from this mirror just like in step 13 for the back mirror (Figure B5).

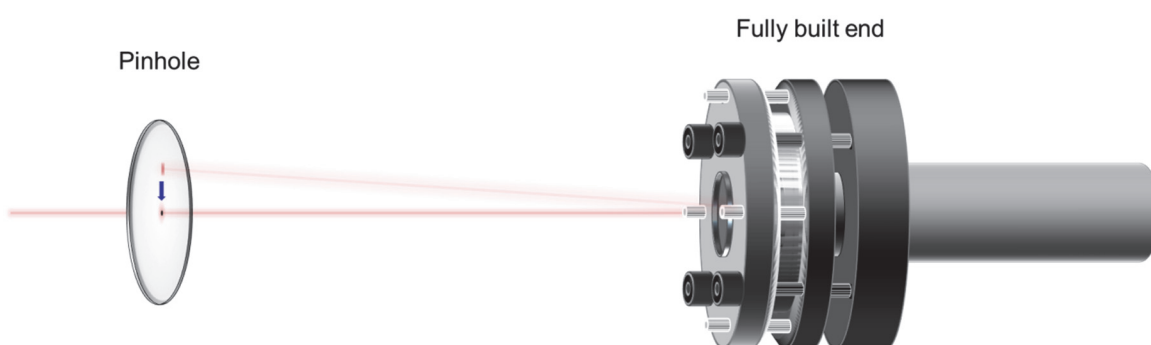


Figure B.5. Reflection of the laser beam onto the pinhole slide after it is reflected from the front HR mirror.

17. Check for vacuum leaks. If vacuum is not achieved, the adjustment screws on the front mirror must be tightened further until vacuum is maintained. A leak rate of 1 Torr/h is acceptable at this point. Once this point was checked you must repeat step 16.
18. Set laser power to its maximum value and use more optical density filters to decrease the power of the incoming beam as close to 100 mW as possible.
19. The above steps should get the alignment close, but further steps are needed. For PS-CRD omit step 20 and continue until the end of this procedure.
20. For Exponential Decay CRD, the operator must be able to see on the oscilloscope a ring-down signal which decreases exponentially as shown in

Figure B6. Adjustments of the front mirror with the fine adjustments mirrors must be done until the longest decay time is achieved.

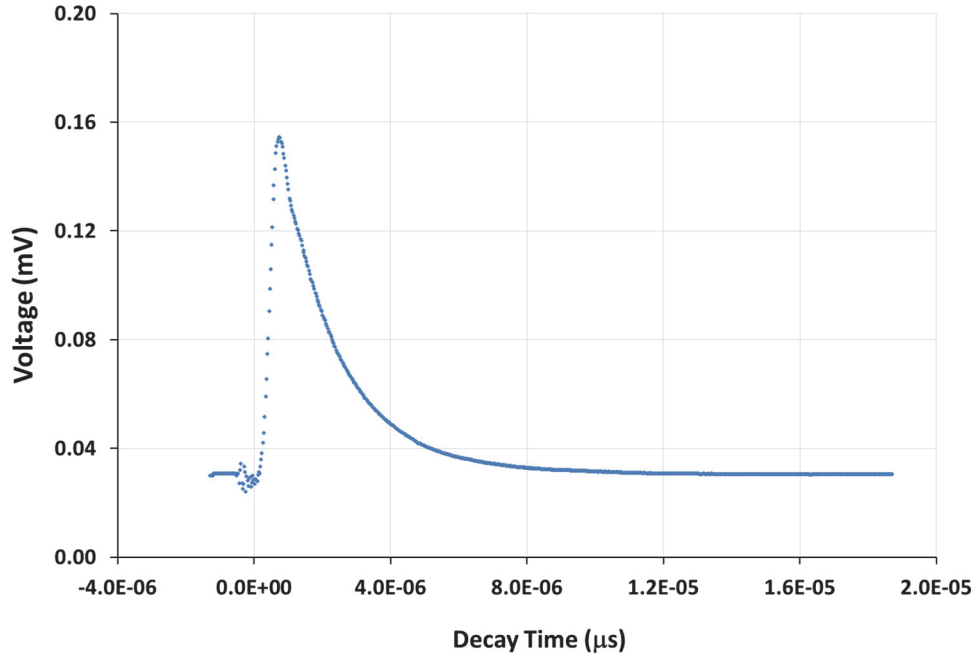


Figure B.6. Ring-down signal for the exponential decay CRD method.

21. Using the fine alignment allen screws on the front mirror, try to adjust them until a signal is detected on the oscilloscope. This signal may look like a slightly deformed square wave or a shark fin, depending on the modulation frequency and length of the cavity. This step can take a little time depending on the initial alignment. Start with one screw and work around to the others.
22. Once the PS-CRD signal is obtained by-pass the cell using turning mirrors to place the beam onto the PMT.
23. Set the reference angle in the lock-in amplifier by pressing the reference button located next to the phase angle display.

24. The front mirror should now be adjusted with the fine alignment screws to maximize this angle. It should get as close to -45° as plausible.
25. After the maximum angle obtainable is found, adjust the frequency of modulation up or down to obtain a -45° angle.

This procedure, if followed closely, should provide a good PS-CRD signal within approximately three hours. Some final adjustments might be needed to tweak the signal, but these come from experience and practice. Once this procedure has been mastered, it can be done in approximately half the time.

APPENDIX C

High Reflectance Mirrors

Either exponential decay CRD or PS-CRD methods require high reflectivity mirrors. The mirrors have a coated side (reflective surface) and a non-coated side that are very delicate and must be handled with care. Considering that the mirrors are the backbone of the Cavity Ring Down technique careful handling and care of these is critical towards succeeding in these experiments.

The mirrors used in this system have been obtained from Los Gatos Inc. These HR mirrors can be used in any CRD system both, at room temperature or in experiments at low temperature. They can also be used at temperatures slightly higher than room temperature, about 15 K to 20 K higher, without jeopardizing the mirrors performance. Experiments requiring warmer temperatures are not recommended since these can deteriorate the high reflectivity coatings on the mirrors. Temperature considerations must be made particularly if measurements will be carried at low temperatures, as these mirrors have to create a leak proof bond with the cell surface. This condition must persist while the system is being cooled to as low as 77 K. To accomplish this indium, as opposed to regular rubber, is used to create an O-ring that can still provide a leak proof seal while being exposed to cryogenic temperatures. Close attention must be taken for this method as the indium has to be applied to the outer sections of the mirror surfaces to avoid possibly damage to the mirror.

It must also be pointed out that the mirrors are under vacuum with an oil vacuum pump as the vacuum source. Over time the mirror surface can become laced with a minute amount of oil, which causes degradation of the CRD signal. Because of this reason, the mirrors must be cleaned periodically. One possible way to clean the mirrors with minimal effort is to use the cryo pump which supplies the vacuum to the cryo jacket. The high vacuum and oil-less system can actually pull small particles off the surface of the mirror over time. Nevertheless, this operation takes between two to three days, and it is encouraged only if time is available. The sample cell can be pumped over the weekend usually yielding good results. If the cell is disassembled, or if the quality of the CRD signal is poor, it is best to use the cleaning procedures presented below.

Mirror Cleaning Procedure

It must be emphasized that if the CRD signal is not obtainable after exhausting all alignment efforts it is almost always a result of the mirrors being dirty. The following procedure should be followed to thoroughly clean the mirror surface.

1. Place a piece of lens tissue on a hard working surface.
2. Place the mirror reflective side up on the lens tissue.
3. Check the surface to make sure no indium or noticeable material is attached to the surface. If it is, create a pad using lens tissue, hold it in a hemostat, place a drop of spectroscopic grade methanol on the tissue, and wipe the mirror surface from the center of the mirror out.
4. If the mirror surface is clear use the drag and drop method to clean it.
 - a. Place a piece of lens tissue on top of the mirror.

- b. Place a drop of spectroscopic grade methanol on the tissue with the mirror underneath it.
 - c. Drag the tissue over the mirror surface making sure no residue is left on the mirror surface. It is useful to use a pair of hemostats to hold the mirror against so it does not slide with the lens tissue.
 - d. Optical soap and spectroscopic grade acetone can also be used if the mirror is extremely dirty.
 - e. Aggressive cleaning can also be used. Make a pad with a piece of lens tissue and place in a pair of hemostats. Place a drop of methanol on it and wipe the surface of the mirror.
 - f. Repeat the drag and drop method.
5. Flip the mirror over and repeat the procedure.
6. Visually inspect each mirror for any particles, if present repeat above procedures.
7. Place the mirror in its case until needed.

Following these procedures should provide a clean mirror surface to start with the alignment process. Without clean mirrors the CRD signal will be difficult or unobtainable; therefore, it is an important beginning step.

APPENDIX D

Cryostat Operation

Both the CRD and TL sample cells are attached to the cryostat which allows the cell to be cooled to cryogenic temperatures and obtain thermal equilibrium for low temperature measurements. The cryostat is basically a large liquid cryogen container that has a simple purpose. It supplies a continuous flow of the cryogen (liquid nitrogen or helium) to a cold head that is attached to the sample cell. A heater is also attached to the cold head which can be controlled remotely to allow equilibrium temperatures to be reached. The cryogen flow going through the cold head can be adjusted by using an outlet valve which is controlled by a micrometer screw. This controls the rate of cooling of the cell which keeps the cell from being thermally shocked. This is especially important in our system because the alignment can be lost completely if the cell moves too much due to the contraction of the aluminum metal of the cell when it is cooled. It is also recommended that the cell assembly be cooled at a slow rate to avoid rupture of either the HR mirrors or windows, which is likely to happen if the assembly is subjected to a sudden decrease in temperature. Below is the procedure for setting up the low temperature system, and operating the cryostat.

1. To begin the filling of the cryostat, the cryo jacket around the cell, or the chamber in the case of TL, must be in place and the vacuum applied. This is achieved by reaching a 10^{-4} torr vacuum with the mechanical pump. Then, with the cryo-pump, a pressure of 10^{-7} torr should be maintained within the system.

2. Before moving on, best alignment conditions must be obtained and a good signal, either TL or CRD, if not present already. This signal will need to be monitored throughout the process.
3. Turn on the temperature controller unit and set the temperature to room temperature. This maintains an equilibrium temperature and ensures the cell does not cool by itself.
4. The cryostat is made up of two dewars. The middle one cools the cell and the outer dewar insulates the center one. Take the cap off of the outer dewar and manually add liquid nitrogen to the dewar until it is full. Be sure to keep the cap on the center dewar so water is not allowed to condense inside of it.
5. Place the cap back on the outer dewar when finished. Do not close the cap too tightly, allow about a fifth to a quarter spin of the screw open.
6. Take the center cap off and using a funnel pour liquid nitrogen into the center dewar. A spacer is used between the funnel and the top of the cryostat to allow for the excess and warmer gasses to escape.
7. Continue adding liquid nitrogen until it begins to spill out the side of the spacer. Place the cap back on the dewar and allow some opening as indicated in step 5.
8. The cryostat might shift while adding liquid nitrogen so adjusting the alignment might be necessary at this point.
9. Set the temperature controller to a lower temperature. Usually it is recommended to lower it in 20 K increments, repeatedly as necessary, to let the cell cool slowly.

10. Allow the cryostat to equilibrate for a couple of hours.
11. Open the micrometer screw on the top of the cryostat to around 20. This allows for the liquid nitrogen to start flowing through the cryo head and cooling of the cell to begin. The process is pressure controlled so if the micrometer screw is opened too much the temperature can go down very quickly if not watched. This is also the reason why the temperature controller is set at 20 K increments. It can be thought of as a back-up just in case something goes wrong.
12. The cryostat holds liquid nitrogen very well and only needs to be refilled about every two days.

The above method provides a starting system for making the cryostat operational. With experience the operation of the system becomes quite simple and is fairly maintenance free. For instructions operating the temperature controller, refer to its manual. The alignment must be monitored during the cooling cycle, but once thermal equilibrium is achieved it becomes very stable and often needs no adjustments for several days.

APPENDIX E

LabVIEW Codes

LabView is a program that provides a user friendly method for developing computer codes through the use of graphical single tasked modules. These modules are arranged in a logic order completing a block diagram, which makes the process very intuitive. The final code results in the buildup of a virtual instrument (VI). Like any other physical instrument, it can send and receive electronic signals to/from the different apparatuses in use for a particular experiment through any computer. These virtual instruments can then control other apparatuses of the experimental setup, as well as, acquiring the data from them. This conveniently stores the data in the computer ready for next step of the experiment. In general, one VI, named “Main”, coordinates all subroutines. Finally, all VI’s should be saved into a library (*.llb) to facilitate execution.

Cavity Ring Down DAQ Code

The main block diagram for the CRD acquisition system is illustrated in Figure E1 which connects all the components of the program together, and organizes them in sequences that the computer can follow and execute. The sequence follow by the program is:

- 1) Move the step motor.
- 2) Wait specified time.
- 3) Acquire one data point from the lock-in amplifier.
- 4) Calculate the absorption.
- 5) Write the data to a file,
- 6) Repeat until the final micrometer position matches the calculated one.

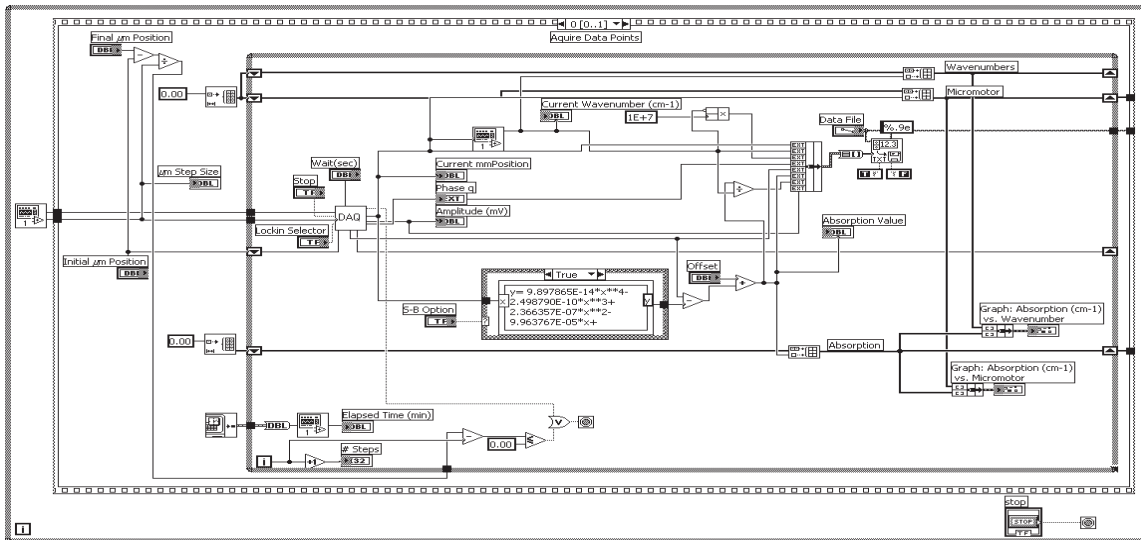


Figure E.1. Measurement Panel Wiring Diagram.

The DAQ vi is the essential vi in any program. This contains several frames operation within it. It starts the data acquisition by moving the step motor or stepper motor. It then has a sequence to allow the lock-in or oscilloscope to respond to the signal after the step by waiting a predetermined amount of time set by the operator. The program then communicates with the lock-in to acquire the data and starts the calculations involved, the ring down time (τ), and then absorption using the algorithms provided by the operator (see Chapter One). After the data point is processed the computer sends a signal back to the lock-in or oscilloscope re-establishing communication. The program then repeats the sequence until the desired final position is reached, previously set by the user. Figures E2 – E6 show the codes that make possible the previous sequence.

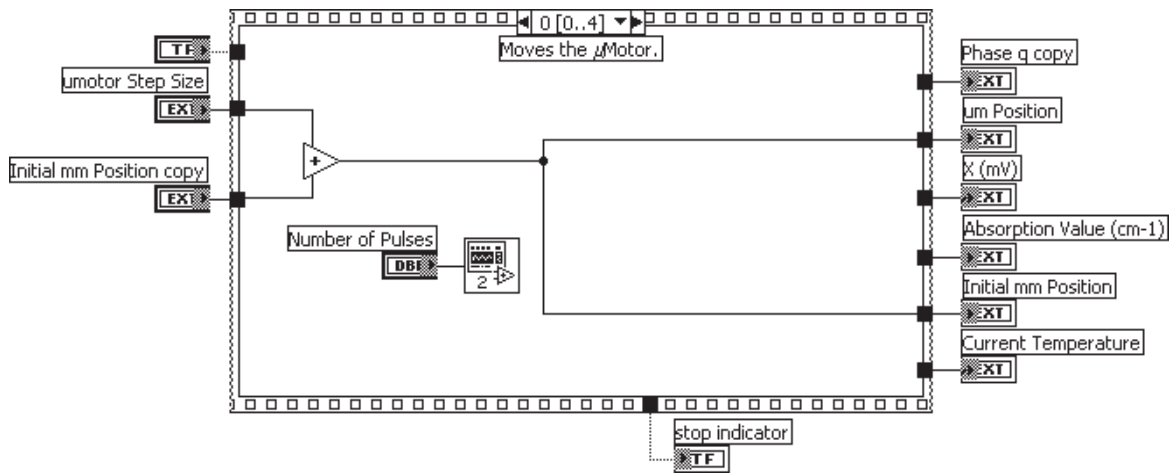


Figure E.2. DAQ Movement of the motor.

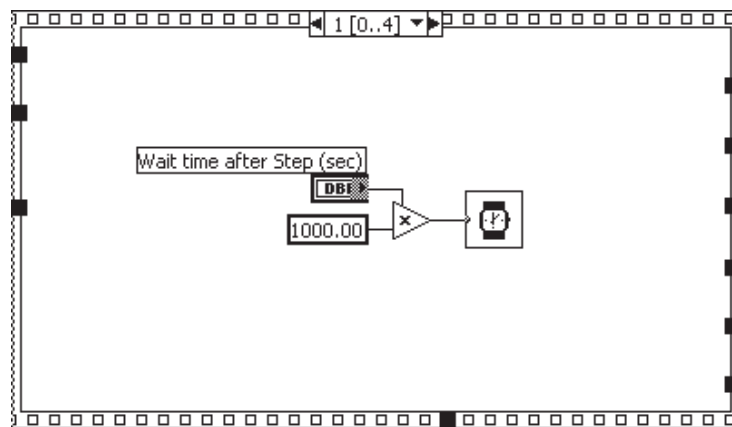


Figure E.3. Delay time.

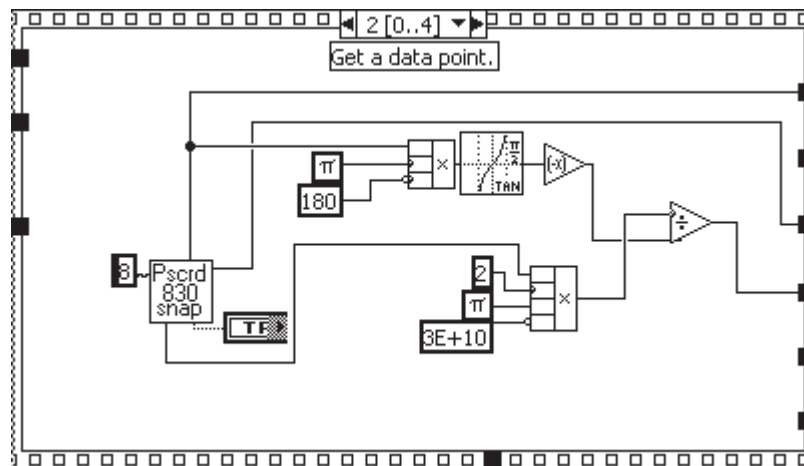


Figure E.4. Acquire Data Point and Calculated Absorption.

The “Pscrd 830 snap.vi” communicates with the lock-in and takes the string of arranged, appended data transmitted by the lock-in amplifier, and separates it into useable data.

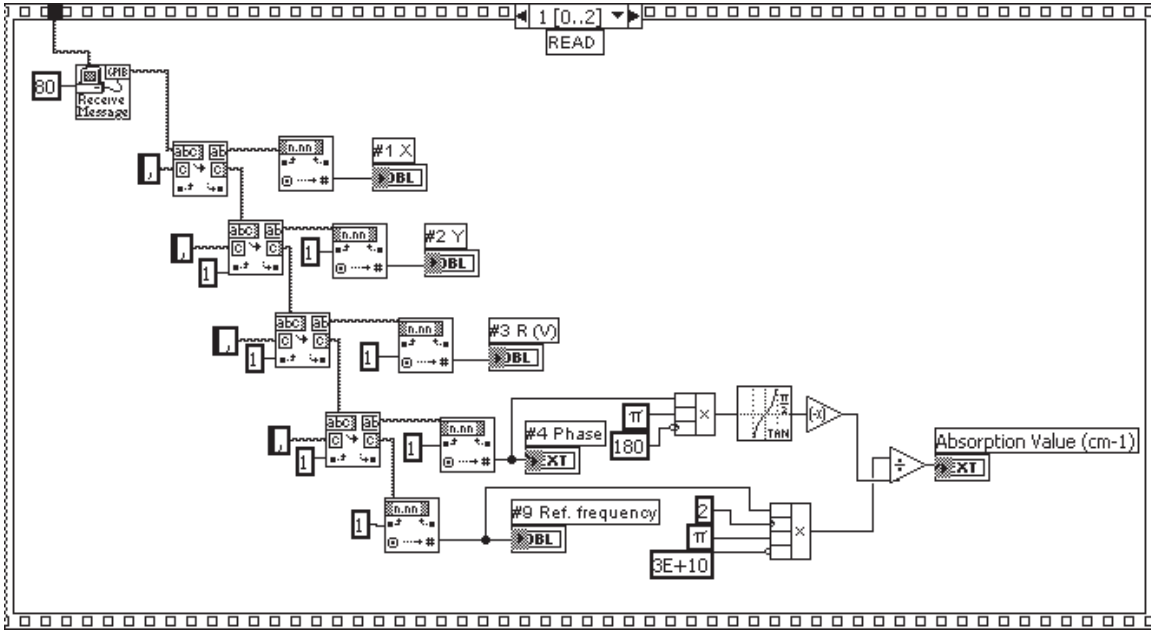


Figure E.5. Pscrd 830 Snap.vi.

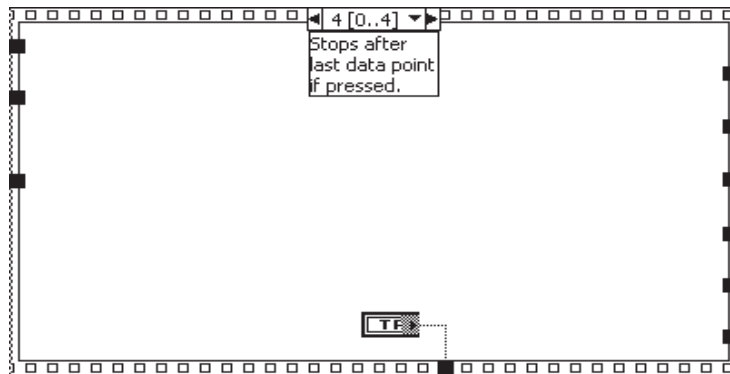


Figure E.6. Stop Data Collection

All the information collected is sent out of the DAQ vi and assembled in the measurement diagram where it is processed and shown on the main panel shown in Figure E7.

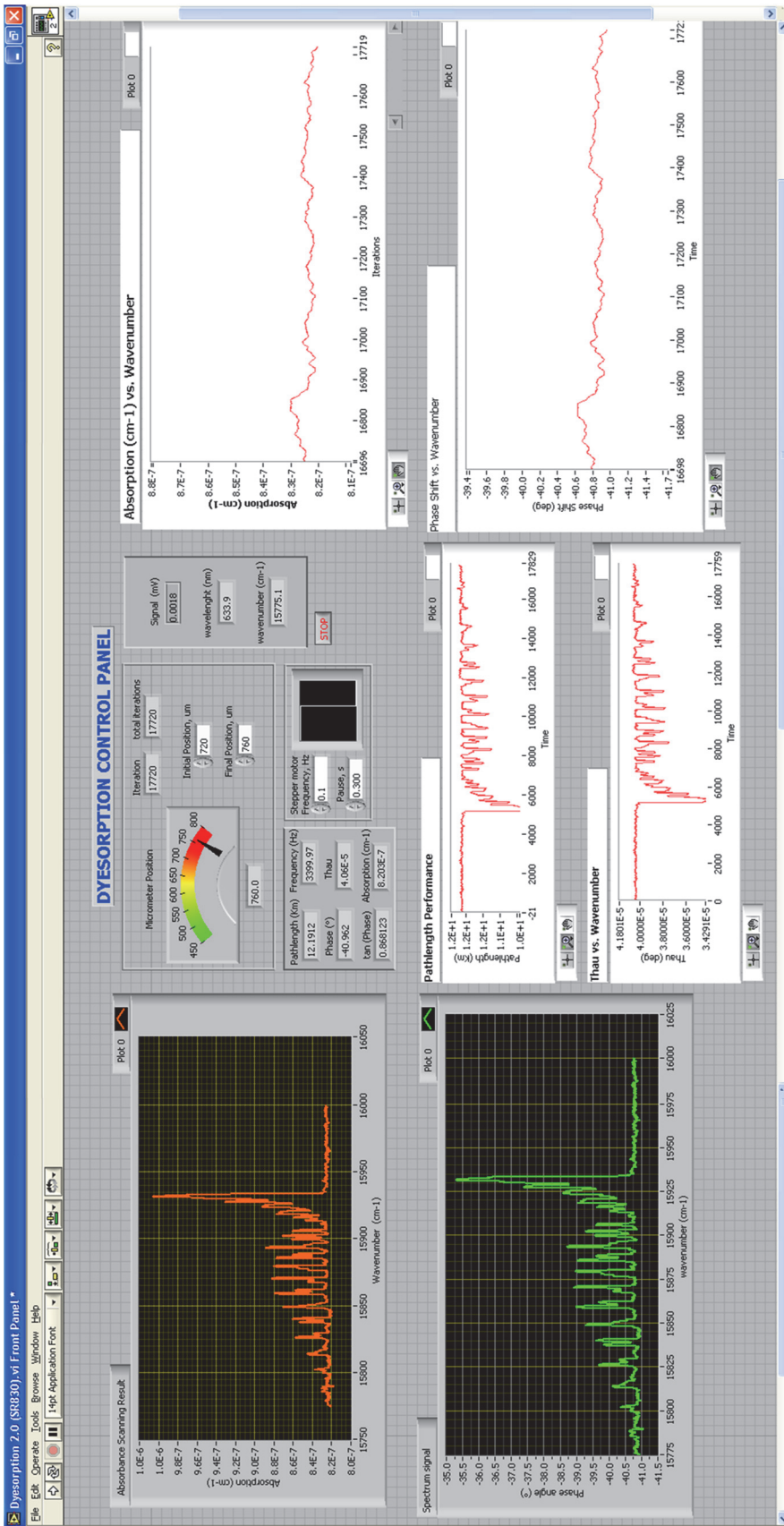


Figure E.7 . Front panel of the Main PS-CRD vi code. The charts with the white background show the signal variation in real time as the scan progresses. The charts with dark background show the final result at the end of the scan. (Top) Absorbance. (Bottom) shift angle.

Thermal Lens DAQ Code

Before starting any scan, it must be confirmed that all the lasers are turned on and their outputs are stable. The selection of the initial and wavelength to be scanned is made on the software. Correspondence between micrometer position of the birefringent filter and wavelength is founded by a calibration chart previously accomplished. The stepper motor should be turned on at the initial micrometer position. If the step size of the stepper motor must be accurately determined by running the Motorcontrol.vi through a series of randomized ranges. The ratio between the final – initial positions in the micrometer and in the code should provide enough information to determine the right step size. Then, the lock-in amplifier must be communicating with the code which is accomplished by establishing the corresponding parameters on the LabView® interface. This parameters are specific of the lock-in amplifier to be used, and can be found in its manual. Once all these conditions are met the spectrometer is ready to scan. Figure D8 shows the main front panel of the code.

Clicking on the start button of the software leads to the DAQ in real time on the computer screen. If the calibration is optimum, the final micrometer position shown on the code must match the one shown on the actual micrometer. The spectrum data can be saved in ASCII format for later analysis. With the data saved, just stopping the program re-sets the system for a new acquisition. At least three spectra of each sample under the same conditions are carried out for averaging.

The code sequence is very similar to that of the PS-CRD code explained on the previous section, except that it calculates the ratio in between the voltage read by the PMD and the heating laser output, as oppose to calculating absorbance. Figures E8 – E14 show this code sequence.

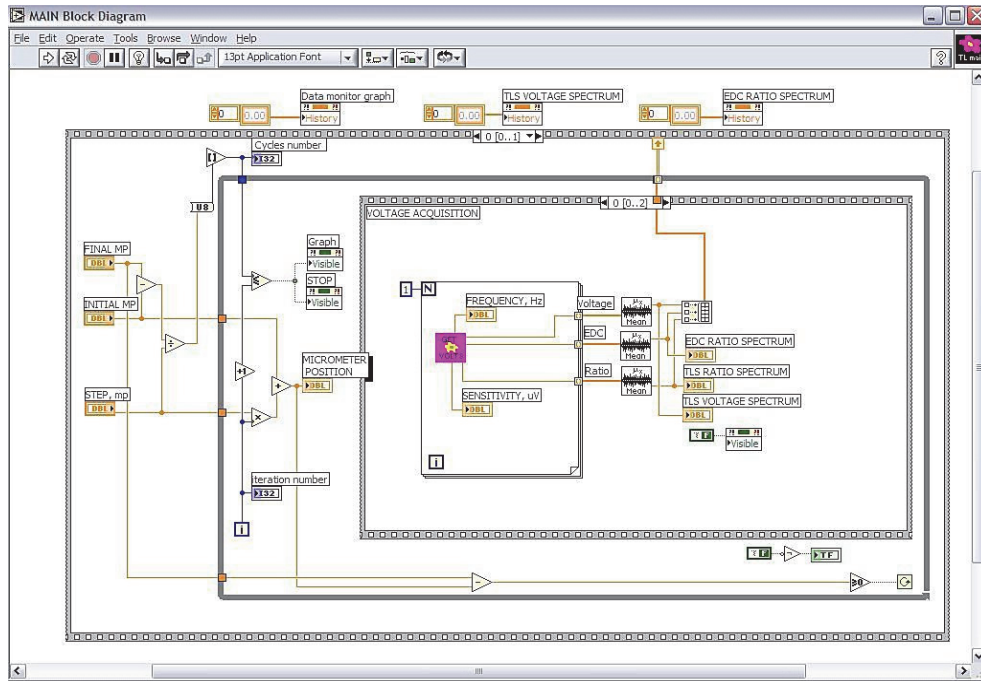


Figure E.8. Voltage acquisition.

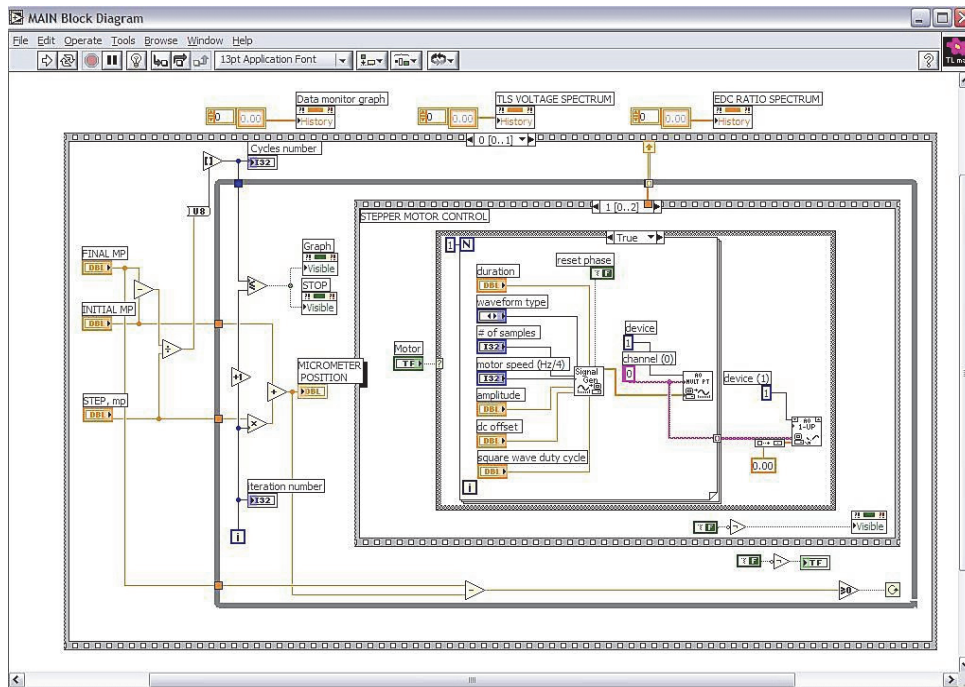


Figure E.9. Stepper motor control.

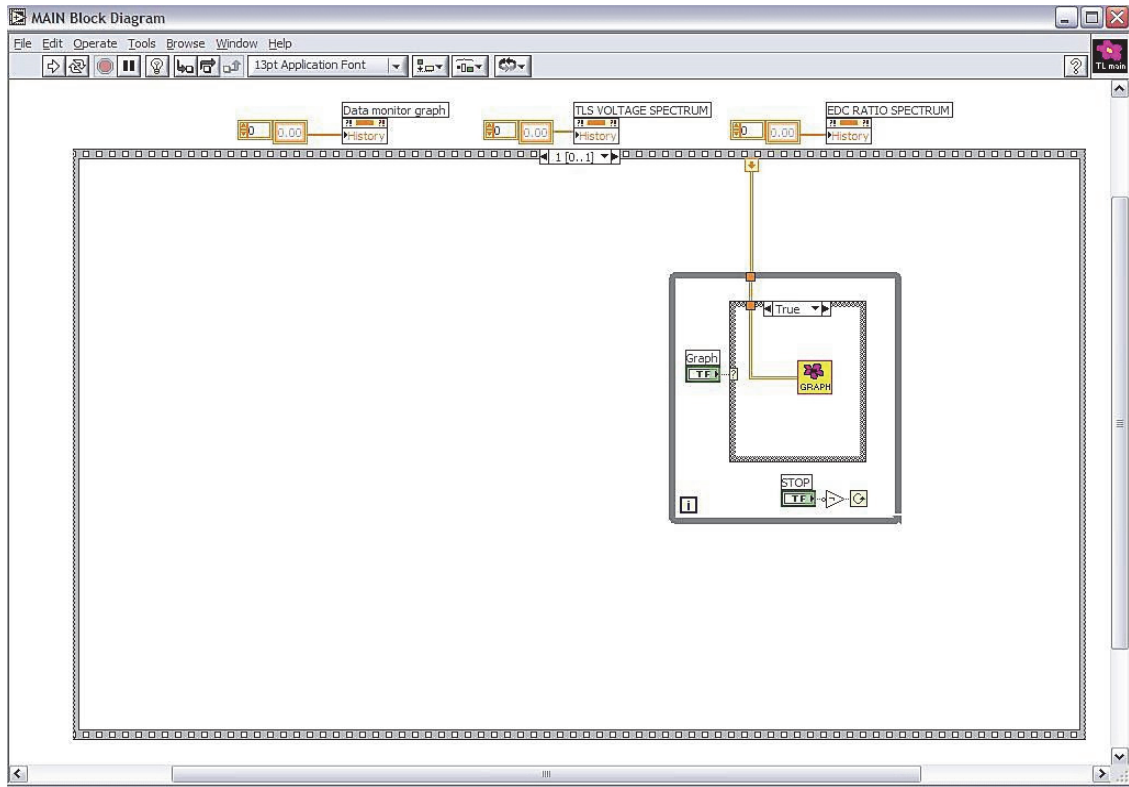


Figure E.10. Saves the raw data.

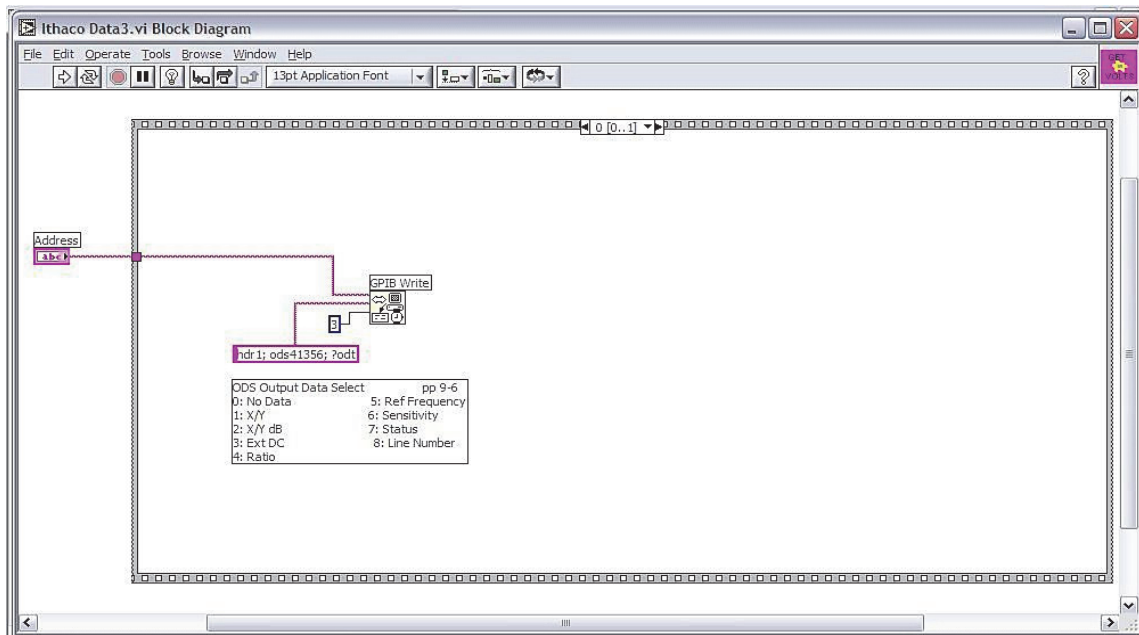


Figure E.11. Addressing of the GPIB, and storage of data points.

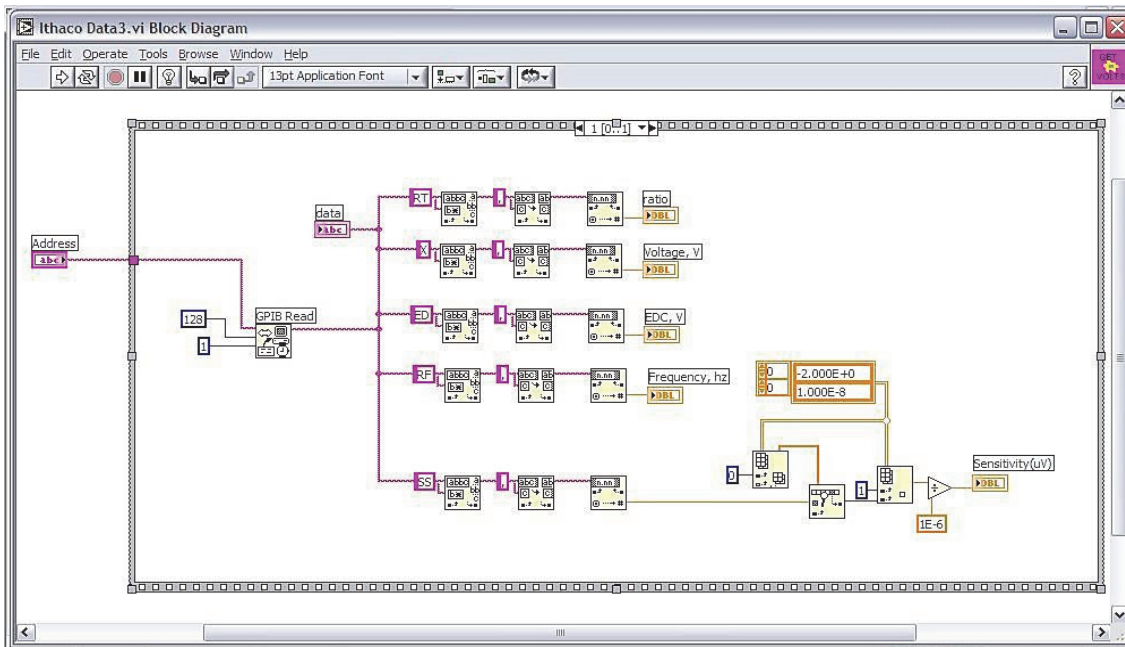


Figure E.12. DAQ, and addressing of the information out from the lock-in amplifier through the GPIB

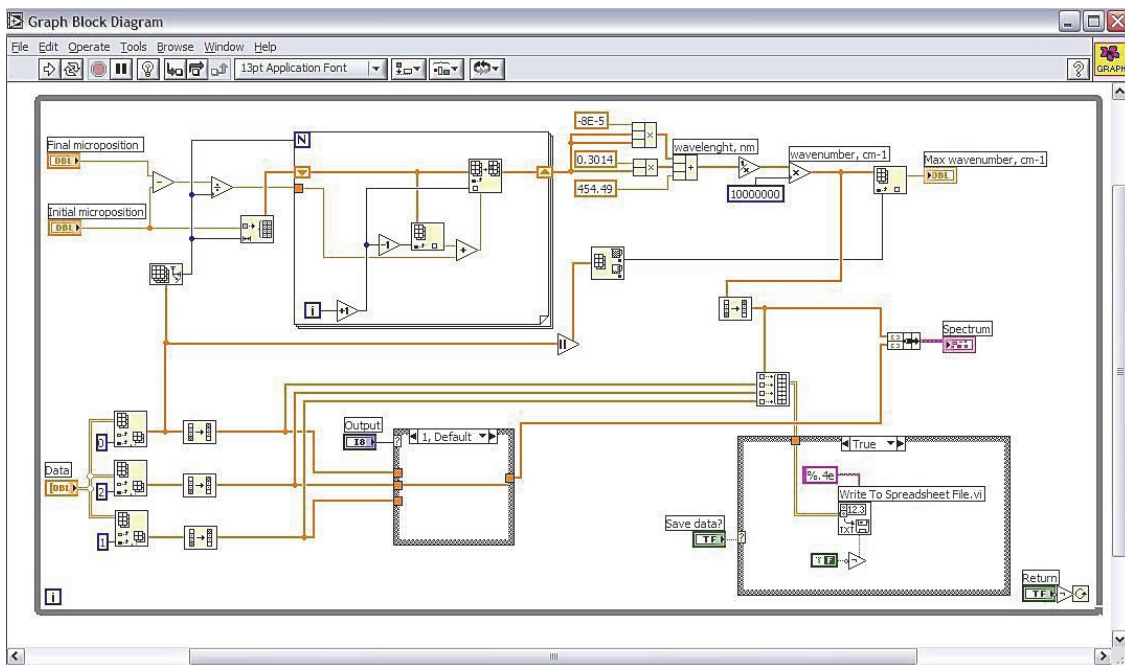


Figure E.13. Block diagram of the Graph.vi that shows the final results

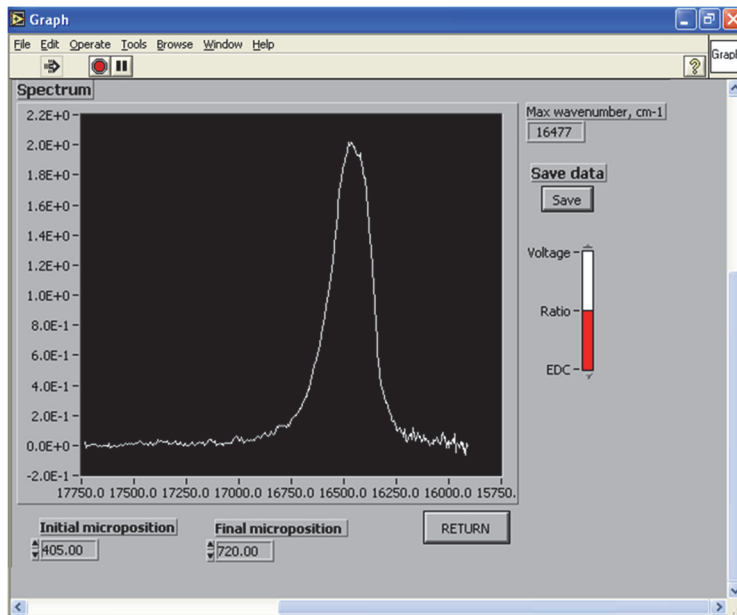
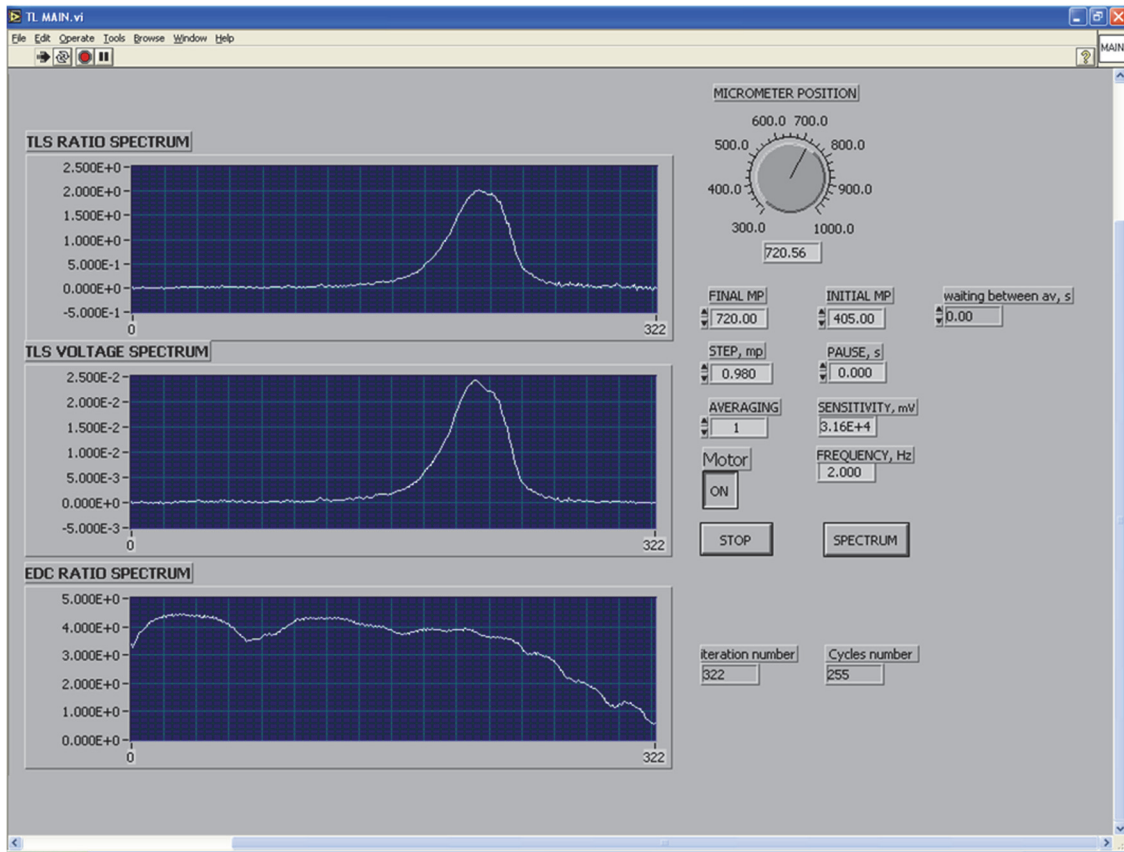


Figure E.14. (Top) Front panel of the Main TLS vi code. EDC: dye laser output, TLS voltage: raw voltage signal, TLS ratio: ratio of the raw signal and the dye laser output. (bottom) Graph result vi, which pops up at the end of the scan.

REFERENCES

- (1) Bertie, J. E.; Keefe, C. D. *J. Chem. Phys.* **1994**, *101*, 4610 - 4616.
- (2) Fang, H. L.; Swofford, R. L. *Appl. Opt.* **1982**, *21*, 55 - 60.
- (3) Gordon, J. P.; Leite, C. C.; Moore, R. S.; Porto, S. P. S.; Whinnery, J. R. *J. Appl. Phys.* **1965**, *36*, 3 - 8.
- (4) Ding, Y.; Herman, M.; Campargue, A. *J. Mol. Spec.* **2002**, *212*, 125 - 129.
- (5) Busch, K. W.; Busch, M. A. In *Cavity-Ringdown Spectroscopy: An Ultratrace-Absorption Measurement Technique*; ACS Symposium Series; 1999; pp 269.
- (6) Berden, G.; Peeters, R.; Meijer, G. *Int Rev Phys Chem* **2000**, *19*, 564-607.
- (7) Allen, G.; Pritchard, H. *Statistical Mechanics and Spectroscopy*; John Wiley & Sons: New York, (1974); 63-78.
- (8) Griffiths, P; Introduction to Vibrational Spectroscopy. In *Handbook of Vibrational Spectroscopy*; John Wiley & Sons: New York, (2001); 34-557.
- (9) Levine, I. *Molecular Spectroscopy*; John Wiley and Sons: New York, (1937), 137-180.
- (10) Scherer, G. J.; Lehmann, K. K.; Klemperer, W. *J. Chem. Phys.* **78**, *6*, 2817 - 2832.
- (11) Diem, M. *Introduction to Modern Vibrational Spectroscopy*; John Wiley & Sons: New York, (1993), 1-44.
- (12) Lopez-Calvo, A. *Vibrational Spectroscopy in Cryogenic Solutions: Application of Thermal Lensing and Fourier Transform Techniques to the Study of Molecular C-H Overtone Transitions*, Baylor University, 2006.
- (13) O'Keefe, A.; Deacon, D. A. G. *Rev. Sci. Instrum.* **1988**, *59*, 2544-2551.
- (14) Du, J.; Zhu, L. *Chem Phys Lett* **2011**, *511*, 213-218.
- (15) Zeuner, T.; Paa, W.; Schmidl, G.; Zopf, D.; Henkel, T.; Csaki, A.; Fritzsche, W. *Sensors and Actuators B: Chemical* **2014**, *195*, 352-358.
- (16) Kerr, E. L.; Atwood, J. G. *Appl. Opt.* **1968**, *7*, 915 - 921.
- (17) Davidsson, J.; Gutow, J. H.; Zare, R. N. *J. Phys. Chem.* **1990**, *94*, 4069 - 4073.
- (18) Navea, J. G.; Lopez-Calvo, A.; Manzanares, C. *J. Phys. Chem. A* **2006**, *110*, 1594-1599.

- (19) Long, M. E.; Swofford, R. L.; Albrecht, A. C. *Science* **1976**, *191*, 183 - 185.
- (20) Lewis, E. K.; Reynolds, D.; Xiaochuan, L.; de Villele, G.; Leduc, C.; Cedeno, D.; Manzanares, C. E. *Chem Phys Lett* **2001**, *334*, 357-364.
- (21) Perez-Delgado, Y.; Manzanares, C. E. *J Phys. Chem* **2010**, *114*, 7918-7927.
- (22) Lopez-Calvo, A.; Manzanares, C. *J. Phys. Chem.A* **2006**, *110*, 10427-10343.
- (23) Herbelin, J. M.; McKay, J. A.; Kwok, M. A.; Ueunten, R. H.; Urevig, D. S.; Spencer, D. J.; Bernard, D. J. *Appl Optics* **1980**, *19*, 144-147.
- (24) Wheeler, M. D.; Newman, S.; Orr-Ewing, A. J.; Ashfold, M. N. R. *J. Chem. Soc. Faraday Trans.* **1998**, *94*, 337 - 351.
- (25) Martyn, D.; Wheeler, M. D.; Newman, S. M.; Orr-Ewing, A. J.; Ashfold, N. R. *J. Chem. Soc. Faraday Trans.* **1998**, *94*, 337-351.
- (26) Lewis, E. K. *Design of a Low Temperature Phase Shift Cavity Ring Down Technique with Applications to High Vibrational Overtones Absorptions*, Baylor University, 2003.
- (27) Lewis, E. K.; Moehnke, C. J.; Manzanares, C. E. *Chem Phys Lett* **2004**, *394*, 25-31.
- (28) Romanini, D.; Lehmann, K. K. *J. Chem. Phys.* **1993**, *99*, 6287-6301.
- (29) Engeln, R.; von Helden, G.; Berden, G.; Meijer, G. *Chem Phys Lett* **1996**, *262*, 105-109.
- (30) Lehmann, K. K.; Romanini, D. *J. Chem. Phys.* **1996**, *105*, 10263-10277.
- (31) Perez-Delgado, Y. Z. *Off-axis Cavity Ring Down Spectroscopy with Exponential and Phase Shift Detection: Absorption Spectra of Weak Transitions at Low Temperatures*, Baylor University, 2009.
- (32) van Helden, J. H.; Schram, D. C.; Engeln, R. *Chem. Phys. Lett.* **2004**, *400*, 320-325.
- (33) Kasyutich, V. L.; Martin, P. A.; Holdsworth, R. J. *Chem Phys Lett* **2006**, *430*, 429-434.
- (34) Kasyutich, V. L.; Martin, P. A. *Chem Phys Lett* **2007**, *446*, 206-211.
- (35) Paul, J. B.; Lapson, L.; Anderson, J. G. *Appl Optics* **2001**, *40*, 4904-4910.
- (36) Bakhirkin, Y. A.; Kosterev, A. A.; Roller, C.; Tittel, F. K. *Appl Optics* **2004**, *43*, 2257-2266.
- (37) Herriott, D.; Kogelnik, H.; Kompfner, R. *Appl Optics* **1964**, *3*, 523-526.
- (38) Newman, S.; Lane, I. C.; Orr-Ewing, A. J.; Newnham, D. A.; Ballard, J. J. *Chem. Phys.* **1999**, *110*, 10749-10757.

- (39) Babcock, H. D.; Herzberg, L. *Astrophys. J.* **1948**, *108*, 167-190.
- (40) Melieres, M. A.; Chenevier, M.; Stoeckel, F. *J. Quant. Spectrosc. Radiat. Transfer* **1985**, *33*, 337-345.
- (41) Xu, S.; Dai, D.; Xie, J.; Sha, G.; Zhang, C. *Chem. Phys. Lett* **1999**, *303*, 171-175.
- (42) Teslja, A.; Dagdigian, P. J. *Chem. Phys. Lett* **2004**, *400*, 374-378.
- (43) Hamers, E.; Schram, D.; Engeln, R. *Chem Phys Lett* **2002**, *365*, 237-243.
- (44) Miller, J. H.; Boese, R. W.; Giver, L. P. *J. Quant. Spectrosc. Radiat. Transfer* **1969**, *9*, 1507-1517.
- (45) PGOHER, a Program for Simulating Rotational Structure, C. M. Western, University of Bristol, <http://pgopher.chm.bris.ac.uk>.
- (46) Gordon, L. P.; Leite, R. C. C.; Moore, R. S.; Porto, S. P. S.; Whinnery, J. R. *Bull. Am. Phys. Soc* **1964**, *2*, 501.
- (47) Fang, H. L.; Swofford, R. L. In *In Ultrasensitive Laser Spectroscopy*; Kliger, D.S., Ed.; Academic Press: NY, 1983.
- (48) Dovichi, N. J.; Harris, J. M. *Anal. Chem.* **1979**, *51*, 728-731.
- (49) Abroskin, A. G.; Belyaeva, T. V.; Filichkina, V. A.; Ivanova, E. K.; Proskurnin, M. A.; Savostina, V. M.; Barbalat, Y. A. *Analyst* **1992**, *117*, 1957.
- (50) Gören, A.; Prior, P.; Macedo, F. *Journal of Physics: Conference Series* **2010**, *214*, 012085.
- (51) Shen, J.; Snook, R. D. *Chemical Physics Letters* **1989**, *155*, 583-586
- (52) Brown, S. M.; Baesso, M. L.; Shen, J.; Snook, R. D. *Anal. Chim. Acta* **1993**, *282*, 711-719.
- (53) Baesso, M. L.; Shen, J.; Snook, R. D. *Chemical Physics Letters* **1992**, *197*, 255-258.
- (54) Snook, R. D.; Lowe, R. D. *Analyst* **1995**, *120*, 2051-2068.
- (55) Bialkowski, S. E. In *Photothermal Spectroscopy Methods For Chemical Analysis*; Chemical Analysis; John Wiley & Sons: NY, 1996; Vol. 134.
- (56) Grabiner, F. R.; Siebert, D. R.; Flynn, G. W. *Chemical Physics Letters* **1972**, *17*, 189-194.
- (57) Hu, C.; Whinnery, J. R. *Appl. Opt.* **1973**, *12*, 72-79.
- (58) Harris, J. M. In *Thermal Lens Effect*; Piepmeir, E. H., Ed.; Analytical Applications of Laser; Wiley & Sons: NY, 1986; Vol. 87

- (59) Mladen Franko, Chieu D. Tran *Rev. Sci. Instrum.* **1996**, *67*, 1-18.
- (60) Swofford, R. L.; Morrell, J. A. *J. Appl. Phys.* **1978**, *49*, 3667-3674.
- (61) Vyas, R.; Monson, B.; Nie, Y.; Gupta, R. *Appl. Opt.* **1988**, *27*, 3914-3920.
- (62) Gupta, R. In *The Theory of Photothermal Effect in Fluids. Photothermal Investigations of Solids and Fluids*; Academic Press: NY, 1989; pp 81-26.
- (63) He, Q.; Vyas, R.; Gupta, R. *Appl. Opt.* **1997**, *36*, 7046-7058.
- (64) Brown, R. H.; Soderblom, L. A.; Soderblom, J. M.; Clark, R. N.; Jaumann, R.; Barnes, J. W.; Sotin, C.; Buratti, B.; Baines, K. H.; Nicholson, P. D. *Nature* **2008**, *454*, 607-610.
- (65) NASA. **NASA Confirms Liquid Lake On Saturn Moon.**
http://www.nasa.gov/mission_pages/cassini/media/cassini-20080730.html
- (66) Raulin, F. *Nature* **2008**, *454*, 587-589
- (67) Cordier, D.; Mousis, O; Lunine, J. I.; Lavvas, P.; Vuitton, V. *The Astrophysical Journal Letters* **2009**, *707*, 128.
- (68) Diez-y-Riega, M. H. *Solubility and Spectroscopy of Unsaturated Hydrocarbons in cryogenic solvents*, Baylor University, 2010.
- (69) Diez-yRiega, H.; Camejo, D.; Rodriguez, A. E.; Manzanares, C. E. *Planetary and Space Science* **2014**, *99*, 28 – 35.
- (70) Ellis, J. W. *Trans. Faraday Soc.* **1929**, 888 – 898.
- (71) R. L. Swofford; M. E. Long; A. C. Albrecht. *J. Chem. Phys.* **1976**, 183 – 185.
- (72) Gordon, R. G. *Journal of Chemical Physics.* **1963**, *39*, *11*, 2788 – 2797.
- (73) Gordon, R. G. *Journal of Chemical Physics.* **1963**, *38*, *7*, 1724.
- (74) Bulanin, M. O.; Bukhmarina, V. N.; Moiseenko, E. G.; Tokhadze, K. G. *Opt. Spectrosc.* **1984**, *56*, *5*, 497 – 501.
- (75) Stancik, A. L.; Brauns, E. B. *Vibrational Spectroscopy.* **2008**, *47*, 66 – 69.
- (76) Gordon, R. G. *Journal of Chemical Physics.* **1964**, *41*, *6*, 1819 – 1829.
- (77) Vu, H.; Atwood, M. R.; Vodar, B. *Journal of Chemical Physics.* **1963**, *38*, *11*, 2671 – 2677